104

NEUTRON RADIOGRAPHIC IMAGING ANALYSIS

NEUTRON RADIOGRAPHIC IMAGING ANALYSIS

Part A

by

MICHAEL PAUL BUTLER, B.Eng.

A Report
Submitted to the School of Graduate Studies
in Partial Fulfilment of the Requirements
for the Degree
Master of Engineering

McMaster University

1980

MASTER OF ENGINEERING (1980)
Engineering Physics

McMASTER UNIVERSITY
Hamilton, Ontario

TITLE: Neutron Radiographic Imaging Analysis

AUTHOR: Michael Paul Butler, B.Eng. (McMaster University)

SUPERVISOR: Professor A.A. Harms

NUMBER OF PAGES: vii, 116

ABSTRACT

In analyzing the processes involved in neutron radiography, there is a need for a well-defined mathematical structure which can simultaneously be used in practical situations without great difficulty. In this report, the edge-spread function method of analysis is considered in some detail. The basic theory is developed, and both the general and the specific viewpoint are considered, in terms of the mathematical functions used. The usefulness of ESF theory in predicting optical density patterns is illustrated. Specific applications of the theory are developed; in particular, studies of image resolution and unsharpness are undertaken.

To determine whether or not ESF methods are a good representation of the physical situation, some alternate methods which consider radiography from a more basic viewpoint are developed. The first of these is a strictly numerical approach, where experimental data is examined without specifying a model for the image formation process; a matrix formulation suitable for characterizing an image is developed.

The second alternate method involves the use of Monte Carlo methods; this allows the incorporation of more realistic parameters into the analysis. For example, screen-film separation and object scattering of neutrons, and their effects on the image, are evaluated. Finally, a two-dimensional analysis of a simple problem is considered, with the end result being a confirmation of the usefulness of ESF theory.

ACKNOWLEDGEMENTS

Having finally (finally!) completed this work, it is only appropriate that I acknowledge the contributions of those who helped and/or hindered my progress along the road to radiographic madness.

First, there is my supervisor, Dr. Archie Harms, whom I may someday forgive for initially propelling me into the study of neutron radiography. His suggestions and assistance are appreciated.

Next, I must thank my long-suffering typists, Miss Janet Delsey and Mrs. Kathy Noon, both of whom did an admirable job of translating the original hieroglyphics into English.

I would like to thank my parents, whose encouragement, or nagging, helped very much in getting me through this and other ordeals. This work is dedicated to them with love.

Finally, I should like to thank Mr. Carl Holmann, without whose assistance this project would have been completed much sooner.

TABLE OF CONTENTS

LIST OF ILLUSTRATIONS

1. INTRODUCTION

To date, the science of image analysis has largely been an empirical field; the analysis of optical density patterns obtained from radiographs has often been a matter of educated curve-fitting, a practice which tends to produce some rather unsatisfactory results. Now, there may be considerable justification for the empirical approach, but in terms of generality, applicability, compactness, and even elegance, the technique leaves much to be desired.

Another approach is to use a combination of statistics and quantum principles; while well-grounded in theory, the rigour of the mathematics is somewhat beyond the ambitions, if not the understanding, of the average worker in image analysis. The same complaint holds for another technique, namely the application of Fourier analysis and the numerous difficulties which that entails: the problem of obtaining manageable functions on either an analytical or a numerical basis is well-known.

Obviously then, some middle ground is required which is sufficiently rigorous in terms of theory, yet remains open to relatively easy practical application. The framework which is further developed in this report involves the use of edge-spread function(ESF) methodology. The preliminary uses of this approach have indicated considerable accuracy and generality, and at the same time the desired rigor is obtained without any particularly terrifying mathematics.

The purposes of this work then, are to outline the structure of ESF theory, and to develop it mathematically in terms of several areas of practical concern. In setting up the mathematics, a certain degree of abstraction is attained; fortunately, this is quickly remedied by the appropriate substitution of realistic parameters and simple functions, so that an easily-digested calculation procedure results. The mathematics is applied to two particular areas: first, there is the fairly straightforward application to predicting the density pattern for a specified material and geometric composition, and second, the matters of resolution and image unsharpness are examined through the use of ESF techniques. It should be pointed out that while this work deals only with the applications of ESF theory to neutron radiography, it is thought that the extension of the basic principles to other areas, such as x- and gamma-radiography, will be a relatively simple matter.

In addition to the ESF techniques, some alternative methods of analysis are presented, which depend on basic physical ideas to a greater extent than does ESF theory. This is done for two reasons: first, if the ESF results can be favourably compared with the results of a model which is more obviously related to a physical process, then the implication is that the ESF model may also be a good representation of that same physical process. This is of course only true within the limitations of the comparison; for example, if ESF theory and a Monte Carlo calculation give similar results in a one-dimensional analysis, it does not guarantee that the ESF model will hold up in a two-dimensional case.

The second reason for developing these methods is the fact that they are of some interest in themselves; it is always useful to find that a mathematical technique can be applied to a new field of practical interest. In addition, sometimes there is a point to just going through a mathematical exercise: even if an application cannot easily be found, the theoretical ideas that are examined may provide a starting point for yet another approach.

The basic idea behind this work is to examine the use of edge-spread function theory from a reasonably rigorous theoretical viewpoint. Previous work( ) has indicated a surprisingly wide range of potential applications in both quantitative and qualitative fashion; thus, it becomes desirable to have a variety of analytical techniques whereby one can further develop the usage of this model. It is hoped that this report clearly illustrates some of these techniques.

2. EDGE-SPREAD FUNCTION METHODOLOGY

2.1 Theoretical Background

In this section, the mathematical formulation of the edge-spread method will be summarized. This theory has been well-defined elsewhere; thus, for further details, one may consult references 1 and 4.

A convenient way to regard the processes involved here is from the viewpoint of input and output: to obtain an expression for the output (the convertor response), one needs to know the form of the input (the attenuated flux) and the effect of the system (the converter screen) on the input.

Using figure 2-1, it is a simple matter to show that the attenuation of the incident flux is given by

$$\phi(u) = \phi_o \exp\left\{- \int_{z_n(u)}^{z_p(u)} \Sigma_a(u,z)dz\right\} \tag{2.1}$$

where $\Sigma_a(u,z)$ is the position-dependent macroscopic absorption cross-section, and $z_p(u)$ and $z_n(u)$ are the upper and lower boundaries of the object at $x = u$.

Now, the system response is the emission of the secondary radiation about the point of neutron impact; this can be represented by some function $R(x,u)$, which gives, in either analytic or numerical form, the effect of transport from a point u to a point x. Thus, in a small region about the point x, the increment of convertor response is

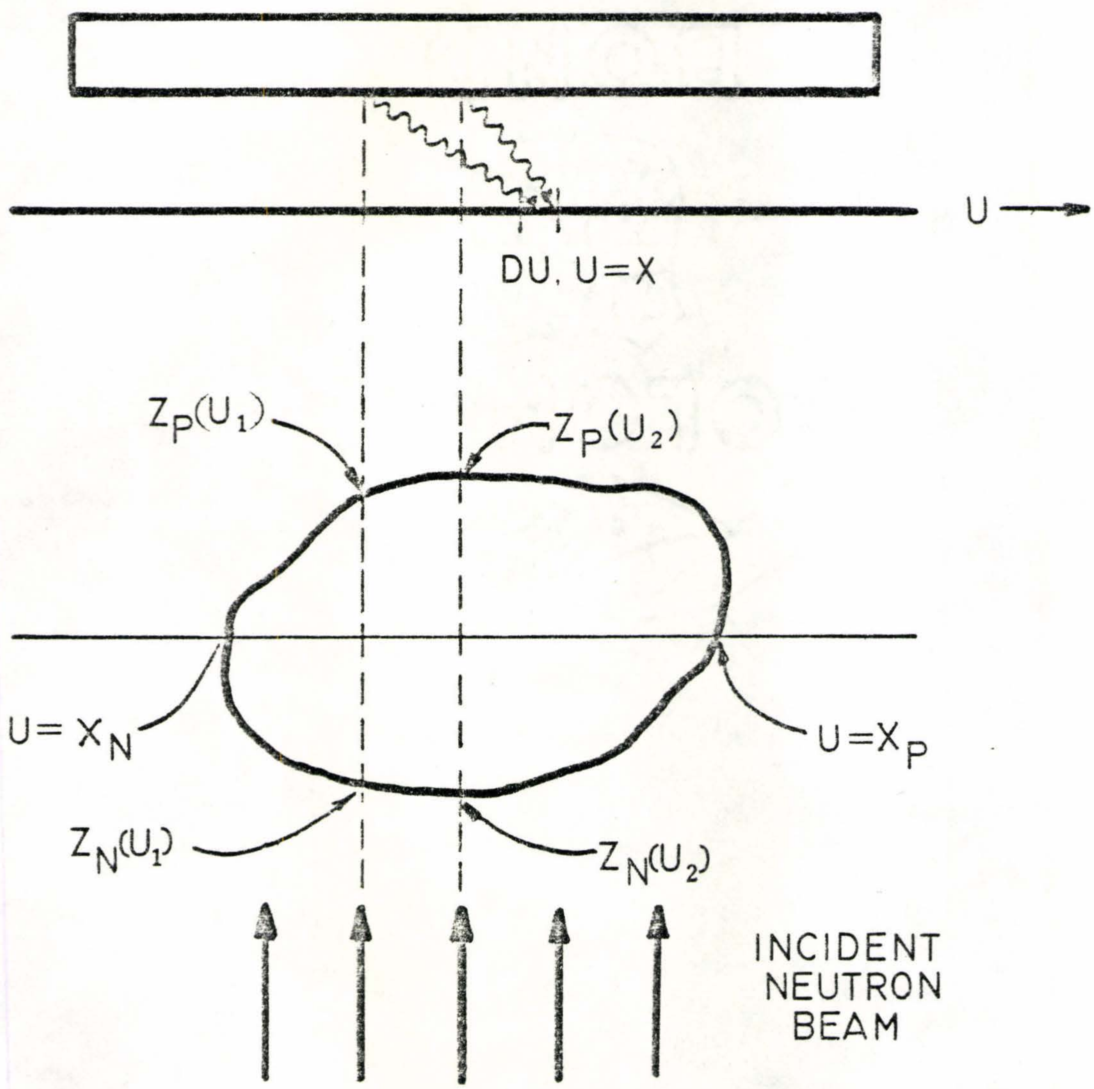

Fig. 2-1: Symbolism used in developing the mathematics for an ESF analysis.

$$dS_A(x,u) = NR(x,u)\phi(u)du \tag{2.2}$$

so that as a final result the total convertor response is given by

$$S_A(x) = N \int_{-\infty}^{\infty} R(x,u)\phi(u)du \tag{2.3}$$

Here N is the desired constant of normalization, which is usually chosen so that $S_A(x)\varepsilon[0,1]$. The limits of integration mean that radiation transport is accounted for from all points $u \varepsilon (-\infty, \infty)$.

In keeping with the previous viewpoint, $S_A(x)$ is the system output; examination of equation (2.3) shows that the basic process occurring here is a convolution of the input ϕ with the system response R. The system analogy will not be considered further, since it was meant for illustrative purposes only; for the purposes of this work, it is the output $S_A(x)$ which is of primary interest, whereas in systems work it is often the form of the input which is required.

Equation (2.3) is a very general form for the response, and as such is a rather abstract object; however, without any great loss of generality, a correspondence between the mathematics and the physics can be obtained by breaking up the region of integration into the three subregions $(-\infty,x_n]$, $[x_n,x_p]$, and $[x_p,\infty)$. The closed region bounded by x_n and x_p is justified by the simplifying assumption that absorption is the dominant process occurring in the object; as a result there is no neutron scattering at the objects edges, hence the exact limits of integration.

Now note that in the regions $(-\infty,x_n]$ and $[x_p,\infty)$ there is no attenuation, by virtue of the fact that there is no material (at least in the more simple situations); this results in the attenuation function becoming equal to unity. This leads to a modified form of equation (2.3):

$$\frac{S_A(x)}{N} = \int_{-\infty}^{x_n} R(x,u)du + \int_{x_n}^{x_p} R(x,u)\phi(u)du + \int_{x_p}^{\infty} R(x,u)du \tag{2·4a}$$

$$= r(x;u)\Big|_{-\infty}^{x_n} + \int_{x_n}^{x_p} R(x,u)\phi(u)du + r(x;u)\Big|_{x_p}^{\infty} \tag{2·4b}$$

where the integral of the response function has been re-defined such that

$$\int_a^b R(x,u)du \equiv r(x;b) - r(x;a) \tag{2·5}$$

If the values of $r(x;u)$ as $u \to \pm\infty$ are set to constants such that

$$\lim_{u\to-\infty} r(x;u) = r_-, \quad \lim_{u\to\infty} r(x;u) = r_+ \tag{2·6}$$

then a final more or less compact form is obtained for the complete response:

$$\frac{S_A(x)}{N} = \left\{r(x;x_n) - r_-\right\} + \int_{x_n}^{x_p} R(x,u)\phi(u)du + \left\{r_+ - r(x;x_n)\right\} \tag{2·7}$$

To clarify the physical-mathematical correspondence referred to earlier, a brief digression is introduced in the form of an example. Consider a knife-edged object similar to that shown in figure 2-2, with

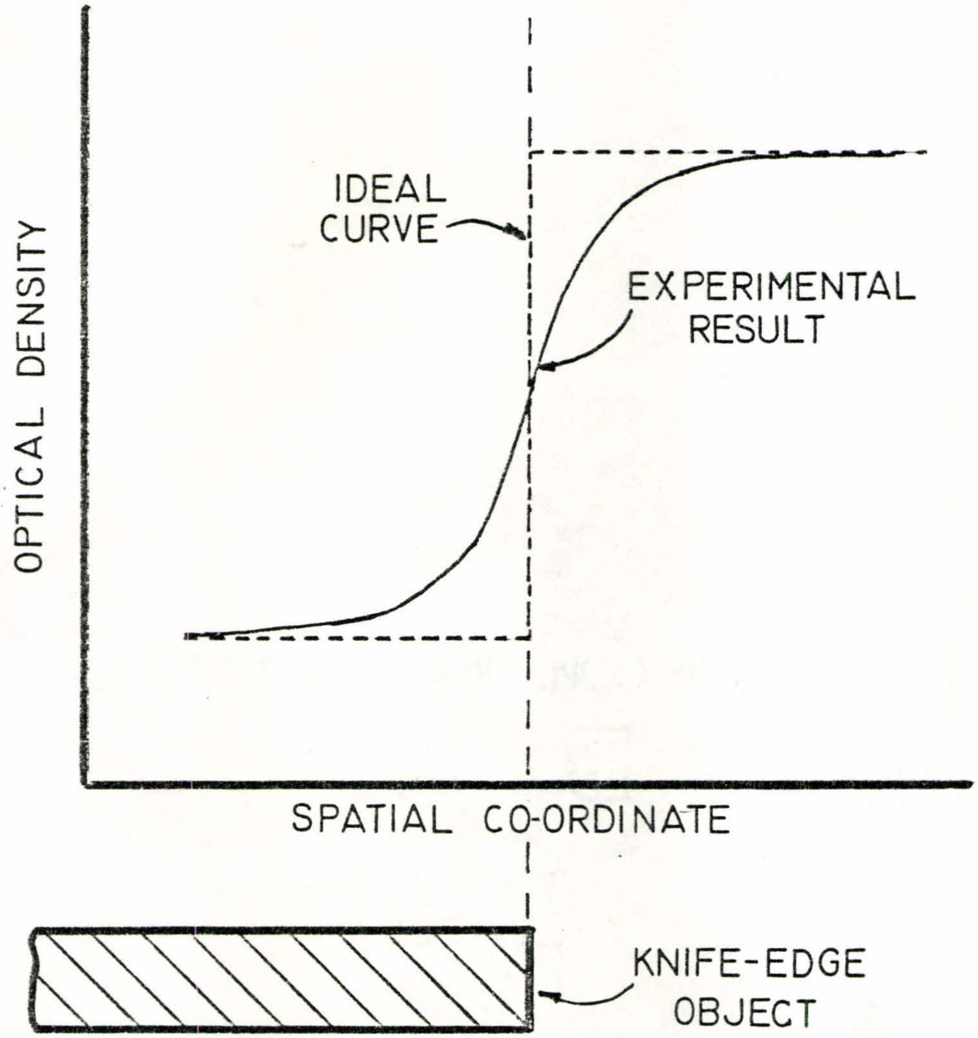

Fig. 2-2: The optical density due to a knife-edge object. The deviation from the ideal curve is caused by screen unsharpness.

the requirement that $(\Sigma_a t) \to \infty$; this corresponds to infinite absorption, so that the attenuation function becomes

$$\phi(u) = \begin{cases} 0, & x \leq x_o \\ 1, & x > x_o \end{cases} \tag{2·8}$$

(x_o being the coordinate of the edge). Noting that $x_n \to -\infty$ and $x_p \to x_o$, these results are substituted into equation (2.5) to yield

$$\frac{S_A(x)}{N} = \{r(x;-\infty) - r_-\} + \int_{\infty}^{x_o} R(x,u)[0]du + \{r_+ - r(x;x_o)\} \tag{2·9}$$

The first term vanishes because of the definition of r_- and the second term vanishes because of the zero integrand giving

$$\frac{S_A(x)}{N} = r_+ - r(x;x_o) \tag{2·10}$$

This is the convertor response for a semi-infinite knife-edge from which it follows that the form for the corresponding rotated knife-edge is

$$\frac{S_A(x)}{N} = r(x;x_o) - r_- \tag{2·11}$$

Comparing these results to equation (2.7), the physical significance of the three terms becomes clear: the first and third terms are the "usual" edge-spread functions, corresponding to knife-edges at $u = x_n$ and $u = x_p$, while the central term represents a perturbation factor which allows for material and geometric effects, such as absorption cross-section variations and arbitrary object shape . It is clear then that provided a suitable spread function is available, the calculation of the convertor response for any object becomes a fairly straightforward matter.

This brings up the next subject, which of course is the matter of what is a suitable spreading function? A number of candidates have been proposed at one time or another[1] and an acceptable function has been found to be the Lorentzian line-spread function, given by

$$L(x,u) = \frac{1}{1 + C_L(x-u)^2} \qquad (2\cdot12)$$

Here C_L is the so-called Lorentzian coefficient and has units of inverse length-squared. A value can be obtained by non-linear curve-fitting techniques although the fitting is usually done with the ESF obtained by integration:

$$\int_{u=-\infty}^{x_o} L(x,u)du = -\frac{1}{\sqrt{C_L}} \tan^{-1} [\sqrt{C_L}\,(x-u)]\Big|_{-\infty}^{x_o} \qquad (2\cdot13)$$

This results from the ESF being much easier to obtain through experimental means than the LSF.

Admittedly, this same constant is the source of some uncertainty in the application of this theory; there is some evidence to suggest that C_L may not be a true constant but instead depends on both material cross-section and thickness. The position adopted here is to obtain appropriate values of C_L from micro-densitometer scans of knife-edges made from materials similar in composition and dimensions to the samples being radiographed and analyzed. This simultaneously removes the immediate need for an analytical model for C_L and helps to reduce the possible error involved. Other methods of characterizing C_L will be discussed in chapter 4.

Having settled on a model, one substitutes the Lorentzian into equation (2.2). The values for r_+ and r_- are easily found to be

$$r_+ = \lim_{u\to\infty} r(x;u) = \lim_{u\to\infty} \left\{ \frac{-\tan^{-1}[\sqrt{C_L}\,(x-u)]}{\sqrt{C_L}} \right\} = \frac{\pi}{2\sqrt{C_L}} \qquad (2\cdot14)$$

and

$$r_- = \lim_{u\to-\infty} r(x;u) = \frac{-\pi}{2\sqrt{C_L}} \qquad (2\cdot15)$$

Thus, equation (2.2) becomes

$$\frac{S_A(x)}{N} = \frac{1}{\sqrt{C_L}} \{-\tan^{-1}[\sqrt{C_L}\,(x-x_n)] + \tfrac{\pi}{2}\} + \int_{x_n}^{x_p} L(x,u)\phi(u)du$$

$$+ \frac{1}{\sqrt{C_L}} \{\tfrac{\pi}{2} + \tan^{-1}[\sqrt{C_L}\,(x-x_p)]\} \qquad (2\cdot16)$$

One can show that the normalization constant in this case is $N = \sqrt{C_L}/\pi$; thus, the final form for the general Lorentzian convertor response is

$$S_A(x) = 1. + \frac{1}{\pi}[t(x_p) - t(x_n)] + \frac{\sqrt{C_L}}{\pi} \int_{x_n}^{x_p} L(x,n)\phi(u)du \qquad (2\cdot17)$$

Here, a notation is introduced which will be frequently used throughout this work; the inverse tangent function is constantly appearing, so as a matter of convenience, the following definition is used:

$$t(u) \equiv \tan^{-1} [\sqrt{C_L}\ (x-u)] \tag{2.18}$$

or

$$t(u)\Big|_w \equiv \tan^{-1} [\sqrt{C_L}\ (w-u)] \tag{2.19}$$

As will become apparent, a number of the more interesting geometries will require numerical solution of equation (2.17), since the attenuation function, $\phi(u)$, usually results in the perturbation term becoming analytically intractable. However, the numerical integration is a straightforward matter, and a generalized computer code has been developed to this end. In section 2.2 a number of response functions are presented in graphic and functional form.

The last point to be discussed with regard to ESF theory concerns the object symmetry; as one might expect, the various calculations can be considerably simplified if it becomes possible to take advantage of symmetry. Note that the advantages occur primarily in those cases where numerical solution is required; if an exact solution of equation (2.6) can be obtained, whether or not the object is symmetric will have little bearing on the relative difficulty of the calculations.

The conditions for object symmetry are quite straightforward; basically one requires that the left and right edges of the object, at $u = x_n$ and $u = x_p$ respectively, are located such that

$$x_p = -x_n \equiv x_o$$

In addition, the object attenuation, $\phi(u)$, must be such that

$$\phi(u) = \phi(-u)$$

Thus, equation (2.6) becomes

$$S_A(x) = 1. + \frac{1}{\pi}\,[t(x_o) - t(-x_o)] + \frac{\sqrt{C_L}}{\pi}\int_{-x_o}^{x_o} L(x,u)\phi(u)du \qquad (2\cdot20)$$

The usual approach in the case of a symmetric integral is to change the limits of integration - to $[0,x_o]$ in this case - and double the resulting integral. In this case, the result would be incorrect since the integrand is not an even function. This is due to the Lorentzian: $L(x,u) \neq L(x,-u)$. Thus, a slightly less simple approach is required.

Consider the two regions $[-x_o,0)$ and $(0,x_o]$; it is clear that if in the first region one transforms u to -u, two nearly identical forms are obtained by splitting the integral term:

$$\int_{-x_o}^{x_o} L(x,u)\phi(u)du = \int_{-x_o}^{0} L(x,u)\phi(u)du + \int_{0}^{x_o} L(x,u)\phi(u)du$$

Because of the conditions imposed previously, $\phi(u) = \phi(-u)$; thus, substituting this and clearing all extraneous negatives, a new form is obtained:

$$S_A(x) = 1. + \frac{1}{\pi}\,[t(x_o) - t(-x_o)] + \frac{\sqrt{C_L}}{\pi}\int_{0}^{x_o} \phi(u)\{L(x,u) \qquad (2\cdot21)$$

$$+ L(x,-u)\}du$$

To clarify, slightly, the fact that symmetry is being used to some advantage, a new "symmetry-modified" Lorentzian is defined:

$$L_s(x,u) = L_s(x,-u)$$

$$\equiv \frac{1}{2}\,[L(x,u) + L(x,-u)] \tag{2.22}$$

$$= \frac{1 + C_L(x^2 + u^2)}{[1 + C_L(x-u)^2][1 + C_L(x+u)^2]}$$

Finally, this is substituted into equation (2.21), giving the result for symmetric geometries:

$$S_A(x) = 1. + \frac{1}{\pi}\,[t(x_o) - t(-x_o)] + \frac{2\sqrt{C_L}}{\pi} \int_0^{x_o} L_s(x,u)\phi(u)du \tag{2.23}$$

2.2 Response Functions for Various Geometries

In this section, convertor response functions for various geometries are presented in both functional and graphic form. Since the functions which these curves represent are all obtained by substituting the appropriate attenuation function into either of equations (2.6) or (2.23), no lengthy derivations will be given here; instead, the various end-results are listed along with the curves in figures 2-3b through 2-3h.

The curves shown here all have been calculated from a "stock" set of parameters, and thus should not be taken as being particularly general. The relevant parameters are illustrated in figure 2-3a.

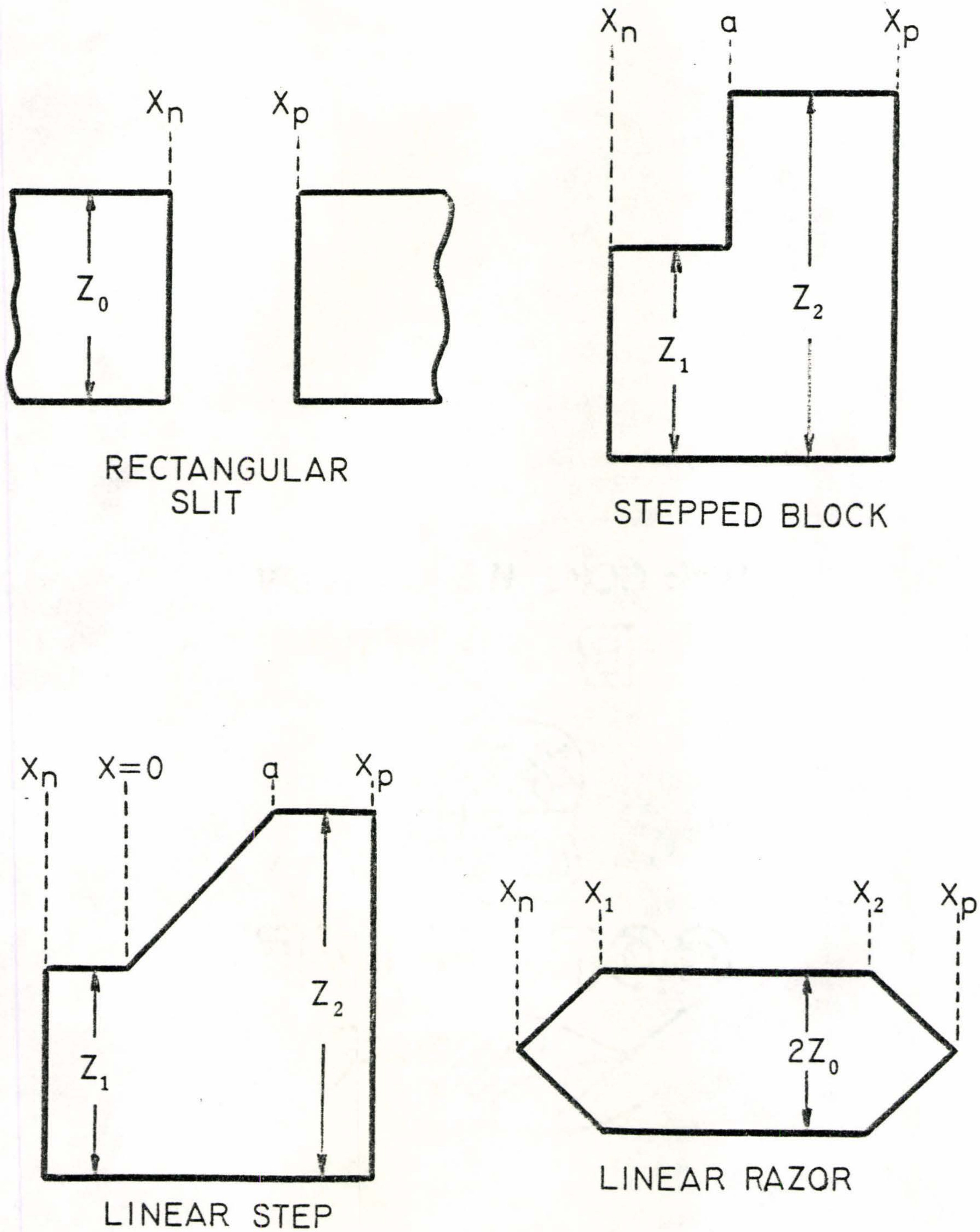

Fig. 2-3a: Parameters used in calculating the convertor response for various object geometries.

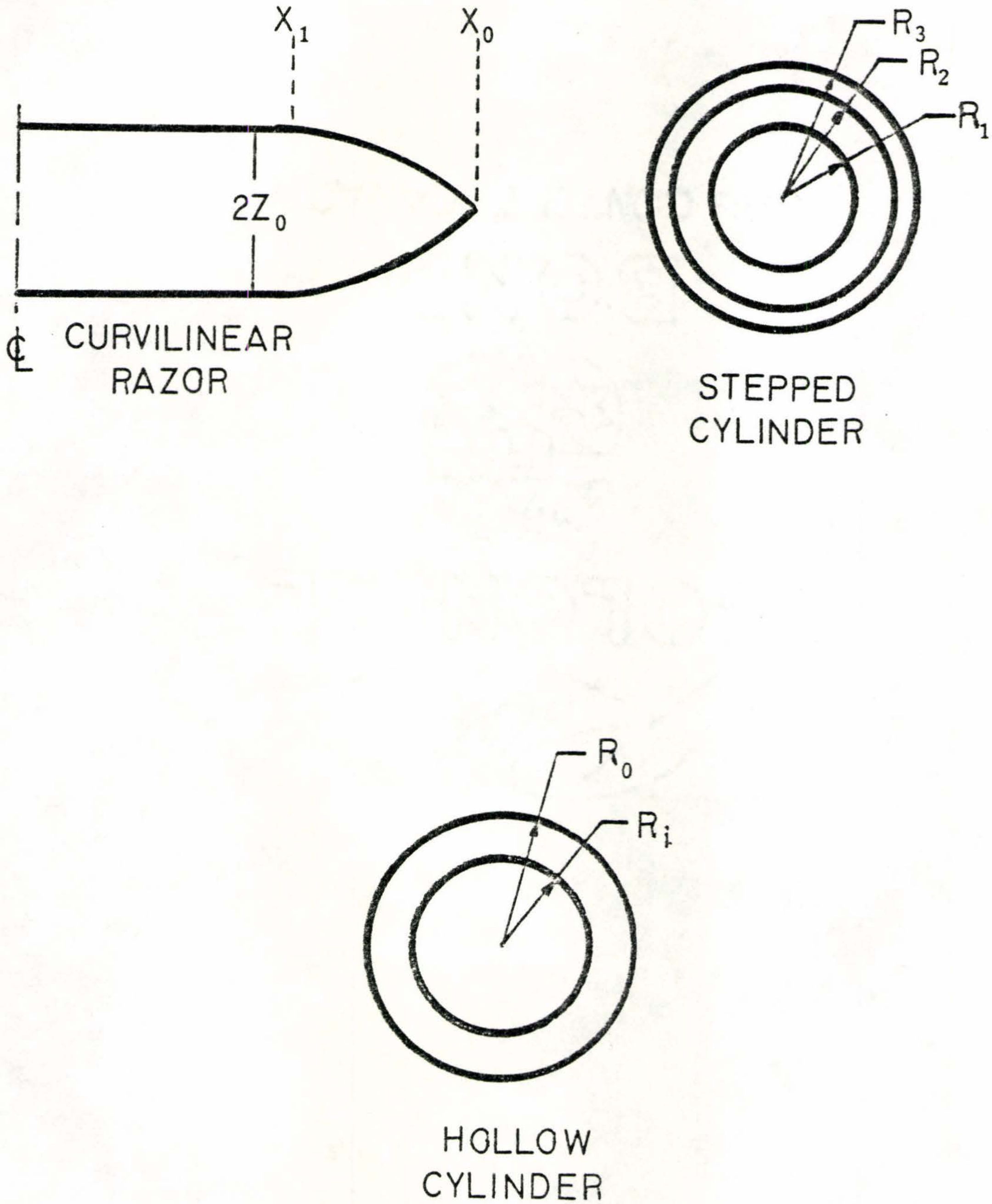

Fig. 2-3a: Parameters used in calculating the convertor response for various object geometries.

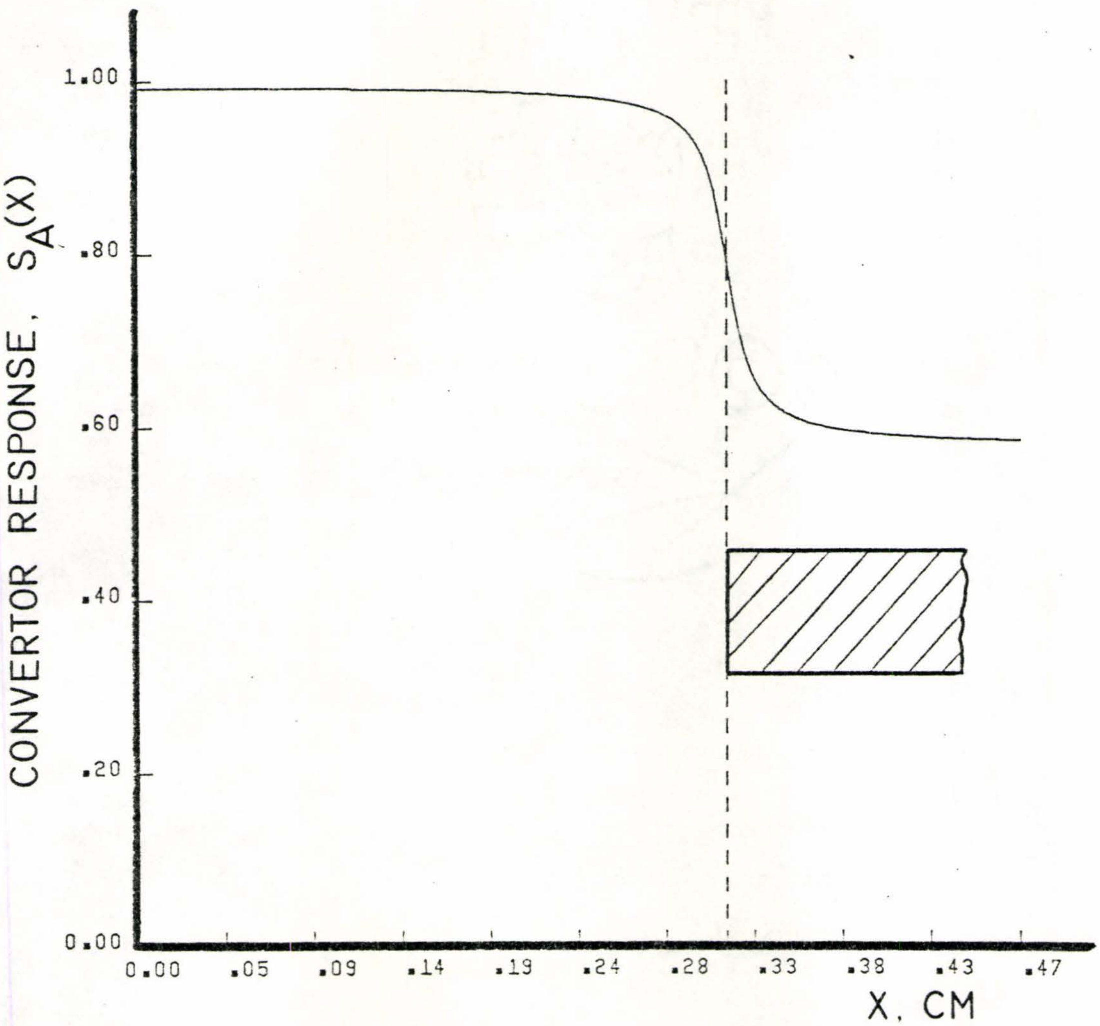

$$S_A(x) = e^{-\Sigma z} + \frac{1}{\pi}(1-e^{-\Sigma z})[t(x_n) - t(x_p)]$$

Fig. 2-3b: The convertor response for a rectangular slit.

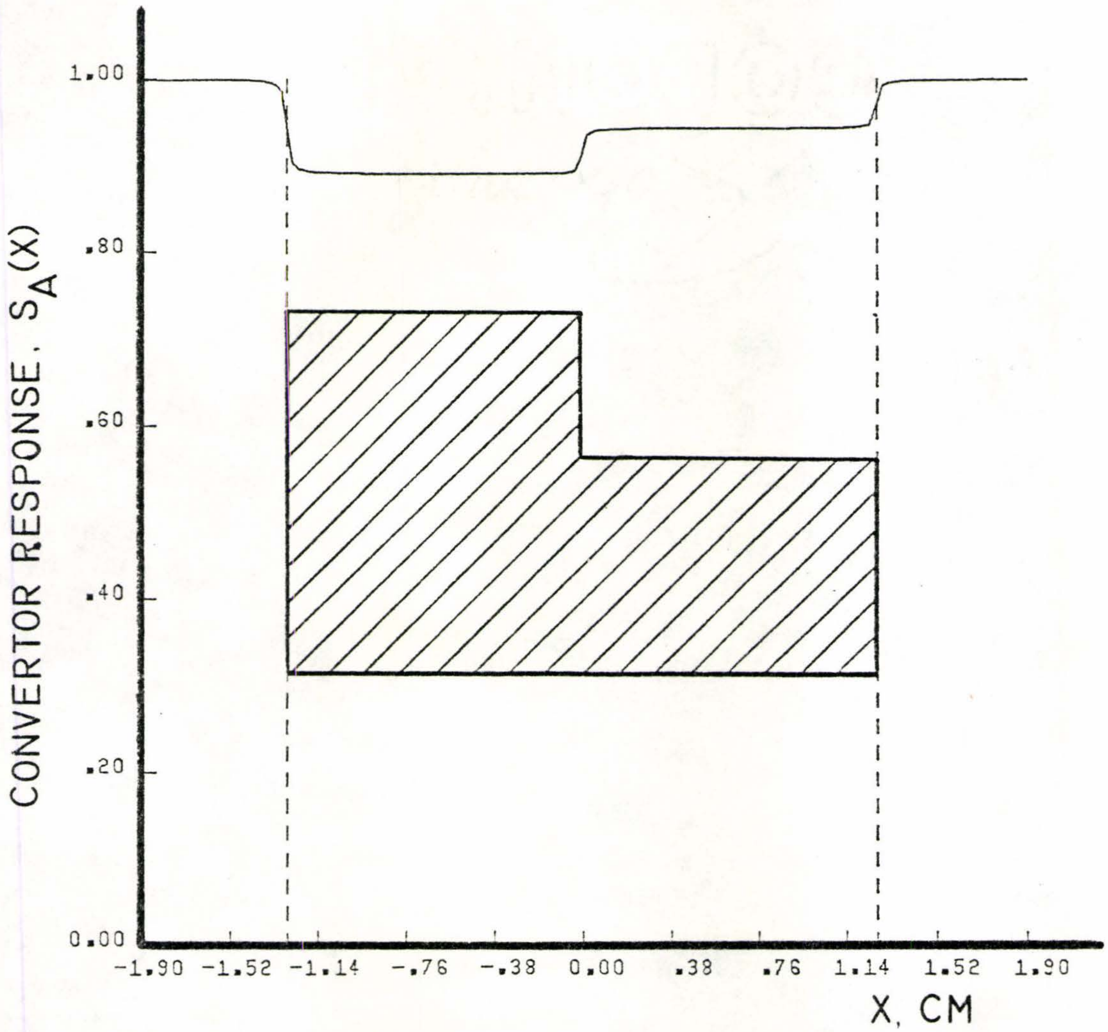

$$S_A(x) = 1 + \frac{1}{\pi}\{(e^{-\Sigma z_1} - 1)\, t(x_n) + (e^{-\Sigma z_2} - e^{-\Sigma z_1})\, t(a) + (e^{-\Sigma z_2} - 1)\, t(x_p)\}$$

Fig. 2-3c: The convertor response for a stepped block.

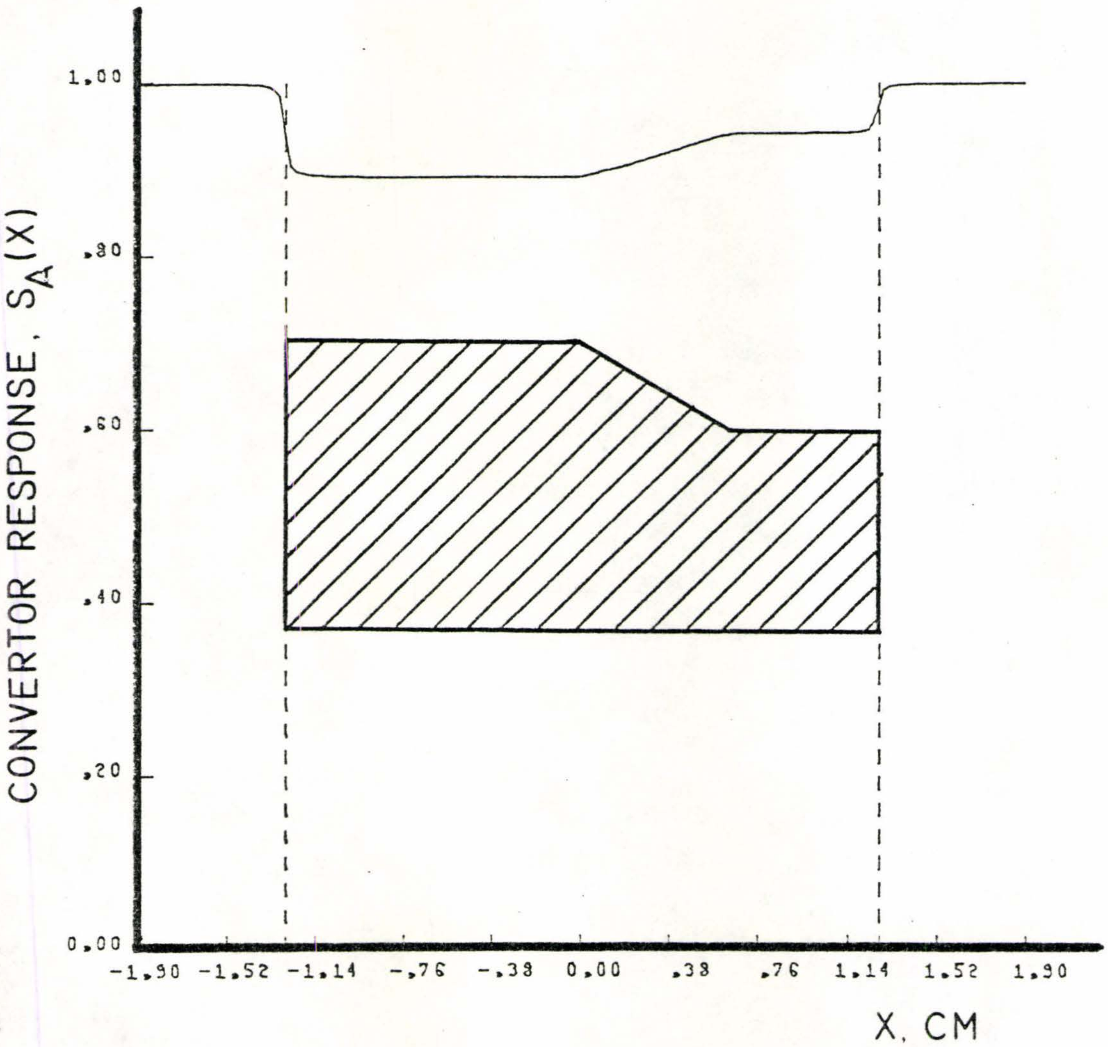

$$S_A(x) = 1. + \frac{1}{\pi}\{(e^{-\Sigma z_1} - 1)\, t(x_n) - (e^{-\Sigma z_2} - 1)\, t(x_p) + e^{-\Sigma z_2} t(a) - e^{-\Sigma z_1} t(0)\}$$

$$+ \frac{\sqrt{C_L}}{\pi} e^{-\Sigma z_1} \int_0^a L\phi\, du;\ \phi(u) = \exp[-\Sigma \frac{(z_2 - z_1)}{a} u]$$

Fig. 2-3d: The convertor response for a "linear step".

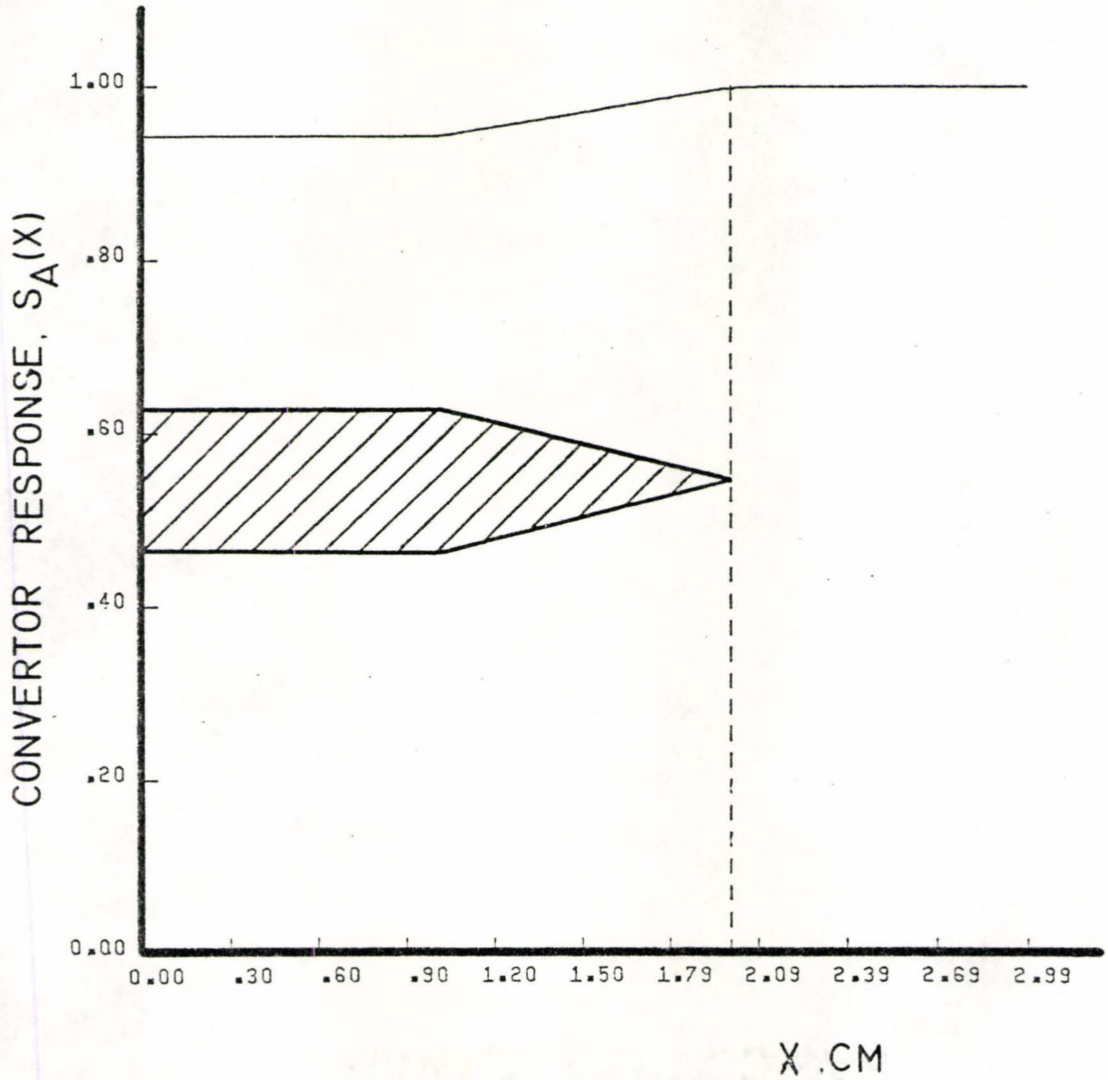

$$S_A(x) = 1. + \frac{1}{\pi}\,[t(x_p)-t(x_n)] + \frac{1}{\pi}e^{-2\Sigma z}\,[t(x_2) - t(x_1)]$$

$$+ \frac{\sqrt{C_L}}{\pi}\,\{\int_{x_n}^{x_1} L\phi_1 du + \int_{x_2}^{x_p} L\phi_2 du\}$$

$$\phi_1(u) = \exp[-\Sigma_z \frac{(u-x_n)}{x_1-x_n}]; \quad \phi_2(u) = \exp\,[\frac{-\Sigma z(u-x_p)}{x_2-x_p}]$$

Fig. 2-3e: The convertor response for a "linear razor".

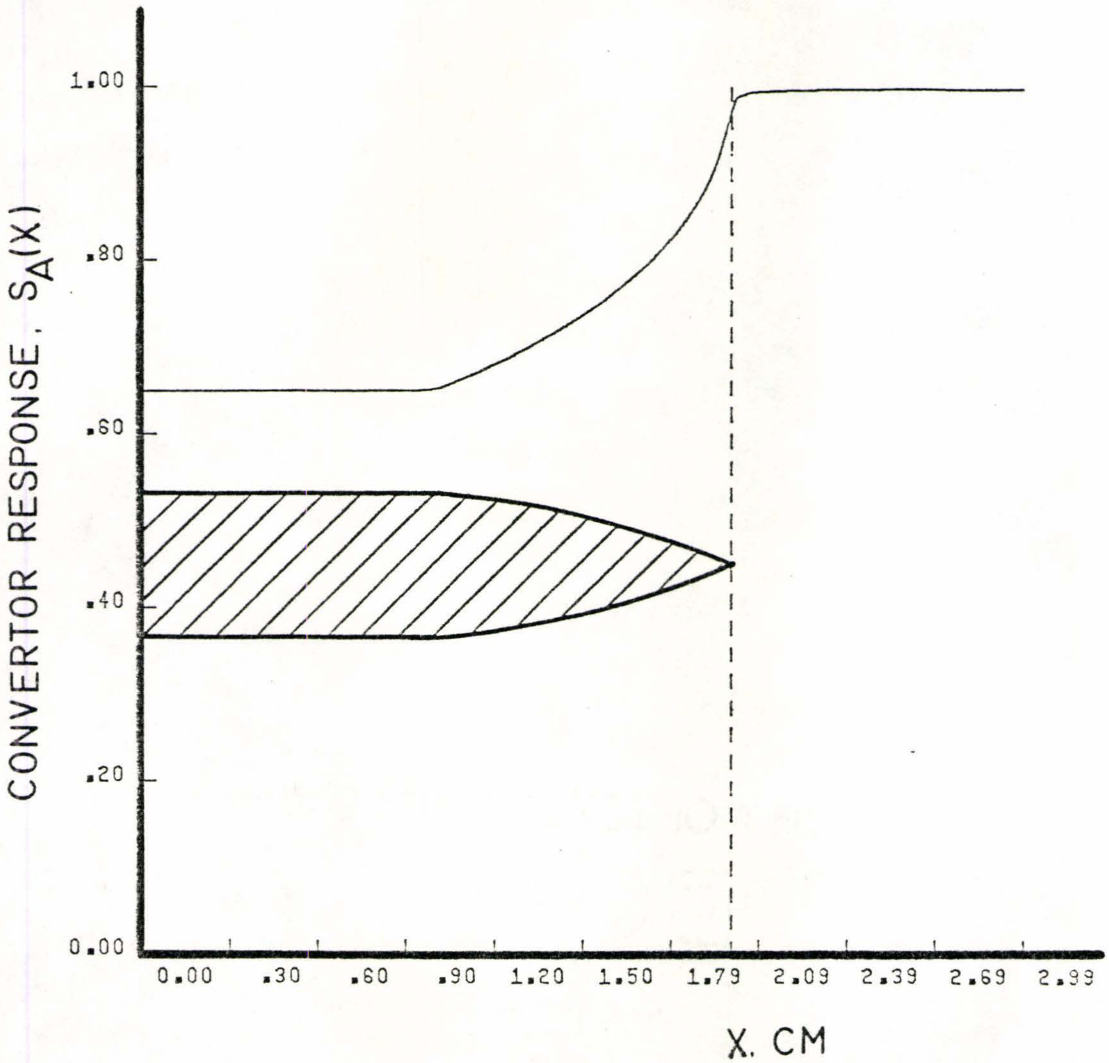

$$S_A(x) = 1. + \frac{1}{\pi}[t(x_o) - t(-x_o)] + \frac{1}{\pi}e^{-2\Sigma z}[t(x_1) - t(-x_1)]$$

$$+ \frac{2\sqrt{C_L}}{\pi} \int_{x_1}^{x_o} L_s \, \phi \, du$$

$$\phi(u) = \exp[- \Sigma z \sqrt{\frac{u-x_0}{x_1-x_0}}]$$

Fig. 2-3f: The convertor response for a "curvilinear razor".

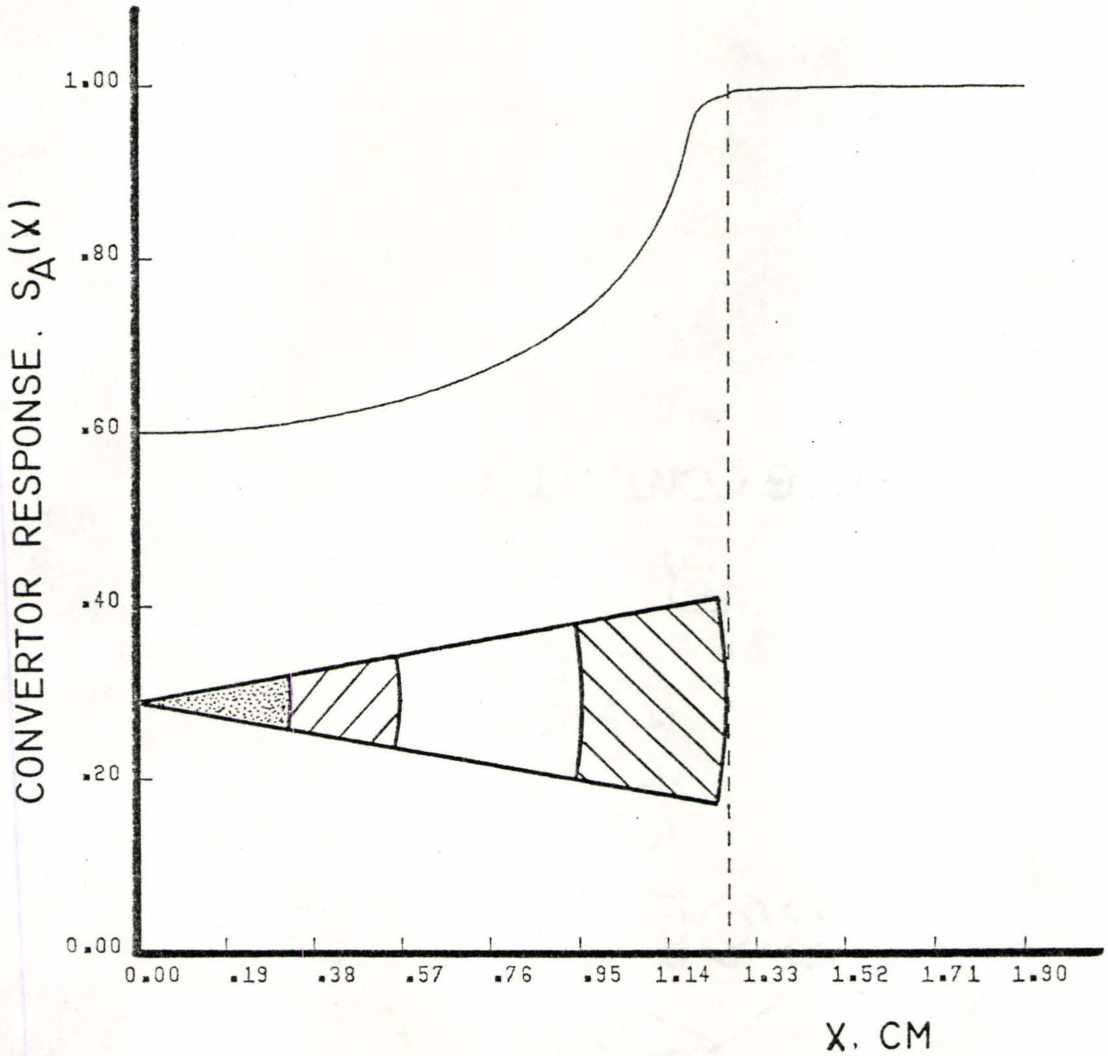

$$S_A(x) = 1. + \frac{1}{\pi}\,[t(R_M) - t(-R_M)] + \frac{\sqrt{C_L}}{\pi}\int_{-R_M}^{R_M} L\phi du$$

$$\ell n[\phi(u)] = -2\sum_{i=1}^{M-1}\Sigma_a^{(i)}\left[\sqrt{R_{i+1}^2-u^2} - \sqrt{R_i^2-u^2}\right]$$

Fig. 2-3g: The convertor response for a "stepped cylinder".

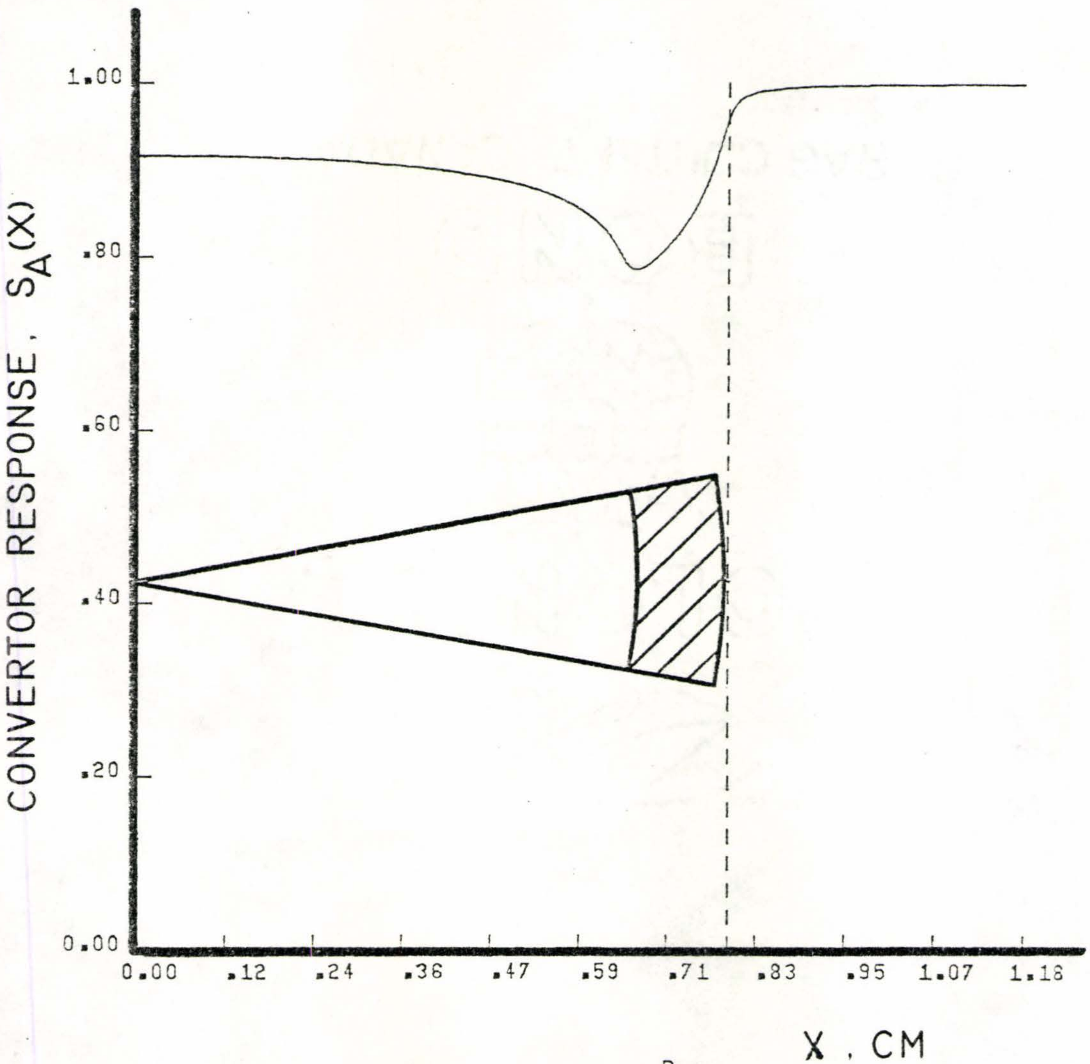

$$S_A(x) = 1. + \frac{1}{\pi}\,[t(R_o) - t(-R_o)] + \frac{\sqrt{C_L}}{\pi}\int_{-R_o}^{R_o} L\phi\,du$$

$$\ell n[\phi(u)] = \begin{cases} \Sigma\,[\sqrt{R_o^2-u^2} - \sqrt{R_i^2-u^2}\,] & 0 \le u \le R_i \\ \Sigma\sqrt{R_o^2-u^2} & R_i < u \le R_o \\ 1 & u > R_o \end{cases}$$

Fig. 2-3h: The convertor response for a hollow cylinder.

3. RESOLUTION AND IMAGE UNSHARPNESS

When considering the matters of resolution and unsharpness, two related but dissimilar topics are being considered. Unsharpness is a matter of assigning a distinct physical location to some object in cases where uncertainty arises through various effects such as screen scattering, object motion, and geometric unsharpness; in contrast, resolution studies involve placing limits on the size of an object which can be seen in a radiograph or a micro-densitometer scan. This is the essential difference: unsharpness, in principle, is independent of object size to the extent that one only requires a knowledge of relative object dimensions, whereas resolution is very much dependent on the absolute object dimensions.

The approach here again involves the ESF technique; however, this time the methods are extended to specific cases of potential application. The theory is presented in somewhat greater detail for this section of the work, since it is all relatively new material; however, it will be shown that the mathematics does not confuse the issues any more than necessary. In this chapter, the emphasis is on analysis rather than experimental details; the reader should consider himself warned.

3.1 ESF Theory of Resolution Analysis

In this report, when resolution is discussed the following is implied: suppose one has a radiograph of some object, or objects, which may contain small particles (or other objects which would appear as particles in a line scan); then for a given particle, the line-scan obtained with a micro-densitometer might appear as shown in figure 3-1. As usual, x_n and x_p represent the physical boundaries of the object.

As shown in the figure, ε_n and ε_p represent the values of x for which

$$S_A(\varepsilon_i) = S_{1/2} \equiv 1/2 \{Max[S_A(x)] + Min[S_A(x)]\} \quad (i = n \text{ or } p) \tag{3.1}$$

Then, a resolution parameter is defined by

$$R = |\varepsilon_p - \varepsilon_n| \tag{3.2}$$

The significance of this parameter is that if some R_o is the smallest value of the full-width at half-maximum which can be found on a densitometer line-scan, then one can say that the smallest object which can be detected has a significant dimension $|x_p - x_n|$. Actually, one must include noise effects due to the film, i.e. the finite grain size of the emulsion. This means that a single value might not be properly assigned to R_o; rather, a range of values is assigned which is centred about a mean value. This is illustrated in figure 3-2.

The physical reasons for requiring a resolution parameter are scattering in the object, and secondary radiation transport in the converter screeen; however, since object scattering is neglected in this analysis, only the latter need be considered.

As the objects being radiographed decrease in size (specifically, in thickness and width), there is less material attenuation of the beam. This has the effect of smoothing the distribution of the beam as it exits

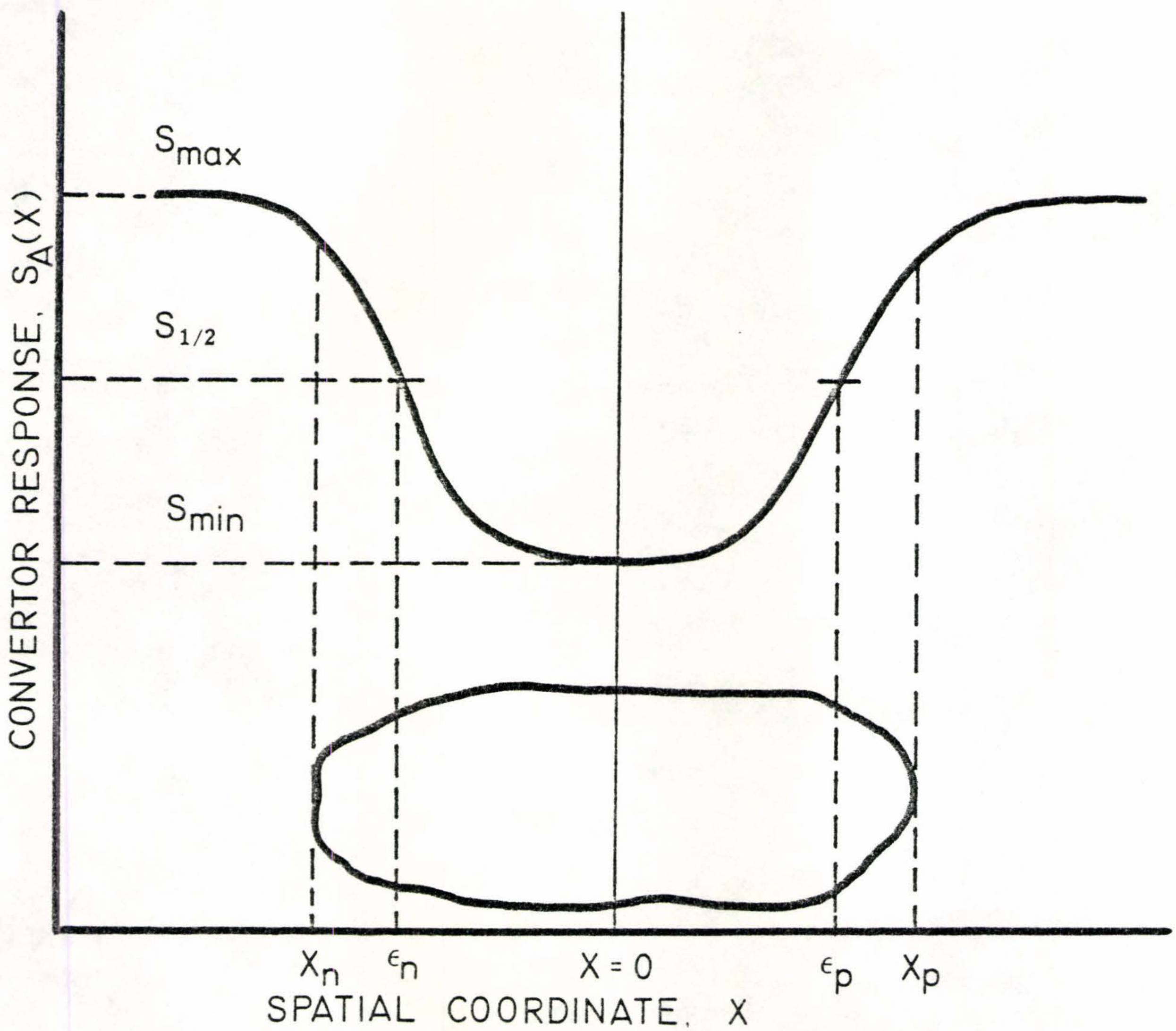

Fig. 3-1: The convertor response due to a small, particulate object.

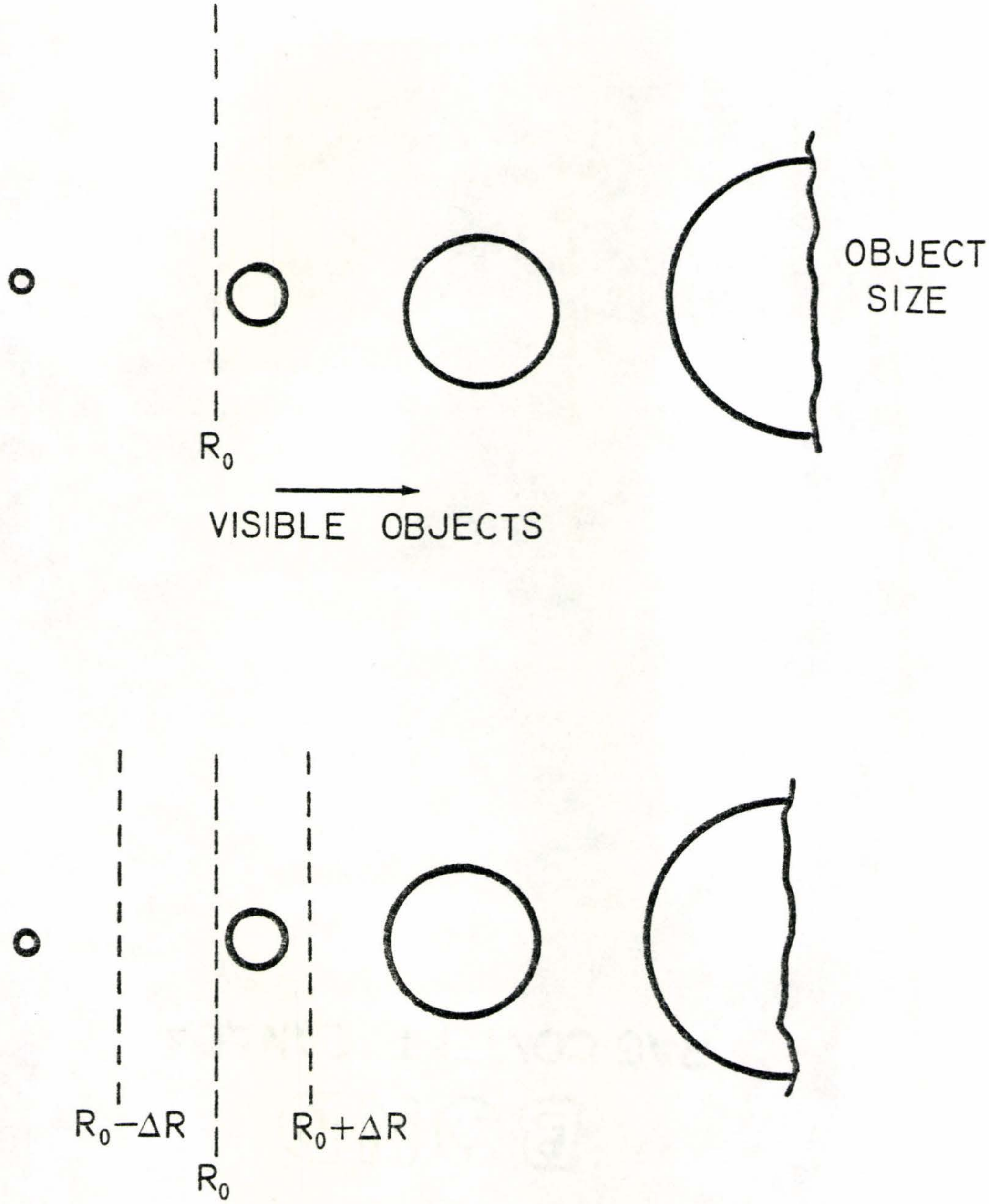

Fig. 3-2: The result of including film "noise" effects in a resolution analysis. Film granularity creates uncertainty in the lower limit of resolution.

from the object, resulting in the object edges being less well-defined in the line-scan. Another fact to be noted is that as the object width decreases, the probability of the point of impact of the secondary radiation being well beyond the object boundaries increases; thus, the optical density closer to the edge decreases. The end result of these factors is to cause the full-width at half-maximum to be less than the object width, $|x_p - x_n|$.

Mathematically, this can be viewed as an overlapping of the two ESF's which are due to the objects edges; neglecting for the moment the material/geometric perturbations, as the object dimensions decrease the two S-curves "approach" each other, causing the flat region of the overall response curve to be reduced in extent. In light of this, it is not surprising that as the object increases in size, the resolution parameter approaches a value of $|x_p - x_n|$, the true width.

As a final comment before beginning the analysis, the direction of curvature of the response curve depends on the material of both the object and any surrounding medium; thus, if $(\Sigma_a t)_{object} > (\Sigma_a t)_{medium}$, the curve will be a "dip", whereas if $(\Sigma_a t)_{object} < (\Sigma_a t)_{medium}$, the curve will show a "bump". Σ_a and t are of course the macroscopic absorption cross-section and thickness, respectively.

Generally, the response curve for any object is given by

$$S_A(x) = \frac{\sqrt{C_L}}{\pi}\left\{\int_{-\infty}^{x_n} \phi_m(u)L(x,u)du + \int_{x_n}^{x_p} \phi(u)L(x,u)du + \int_{x_p}^{\infty} \phi_m(u)L(x,u)du\right\} \tag{3.3}$$

This time, any attenuation properties of the medium surrounding the object are accounted for by defining the new attenuation function $\phi_m(u)$. For simplicity, ϕ_m will be assumed constant, leading to the modified form

$$S_A(x) = \phi_m \{1 + \frac{1}{\pi} [t(x_p) - t(x_n)]\} + \frac{\sqrt{C_L}}{\pi} \int_{x_n}^{x_p} L(x,u)\phi(u)du \tag{3.4}$$

$$\equiv g(x;\vec{p}) \tag{3.5}$$

Here, $\vec{p}$ is an all-purpose vector of object and medium parameters such as cross-sections, thickness, and so on. For convenience, C_L will be taken as constant for a given material.

As stated previously, the resolution parameter is given by

$$R = |\varepsilon_p - \varepsilon_n|$$

It is clear then, that R can be calculated by solving the two equations

$$\begin{aligned} g(\varepsilon_n;\vec{p}) - S_{1/2} &= 0 \\ g(\varepsilon_p;\vec{p}) - S_{1/2} &= 0 \end{aligned} \tag{3.6}$$

where

$$S_{1/2} = 1/2 \{Max[S_A] + Min[S_A]\}$$

In the case of symmetry, only one equation has to be solved:

$$g(\varepsilon;\vec{p}) - S_{1/2} = 0 \tag{3.7}$$

where $\varepsilon \equiv |\varepsilon_p| = |\varepsilon_n|$, and $x_o \equiv |x_p| = |x_n|$.

In practice, this much generality is probably unnecessary; symmetry will be present in many cases, and in addition the objects of concern will likely be small enough that one can make certain simplifying approximations about the object shape. Also, it is not unreasonable to assume constant cross-sections, i.e.

$$\Sigma_{a,\text{object}} \equiv \Sigma$$

$$\Sigma_{a,\text{medium}} \equiv \Sigma_1$$

As an example of the type of approximation one can make, consider figure 3-3; this shows the set-up for the block approximation, which is obviously the most simple form for determining R. In this case, equation (3.2) reduces to

$$S_A(x) = e^{-\Sigma_1 z} \{1 + \frac{1}{\pi} [t(\delta) - t(-\delta)]\} + \frac{\sqrt{C_L}}{\pi} \int_{-\delta}^{\delta} L(x,u)* \{e^{-2\Sigma\delta-\Sigma_1(z_p+z_n-2\delta)}\}du$$

$$= e^{-\Sigma_1 z} \{1 + \frac{1}{\pi} (e^{-2(\Sigma-\Sigma_1)\delta}-1)[t(-\delta) - t(\delta)]\} \qquad (3.8)$$

Assuming that $\Sigma_1 > \Sigma$, it is clear that S_{min} and S_{max} are such that

$$S_{min} = \lim_{x\to\infty} S_A(x) = e^{-\Sigma_1 z}$$

$$S_{max} = \lim_{x\to 0} S_A(x) = e^{-\Sigma_1 z} \{1 + \frac{2}{\pi} [e^{-2(\Sigma-\Sigma_1)\delta}-1]t(-\delta)\big|_0\} \qquad (3.9)$$

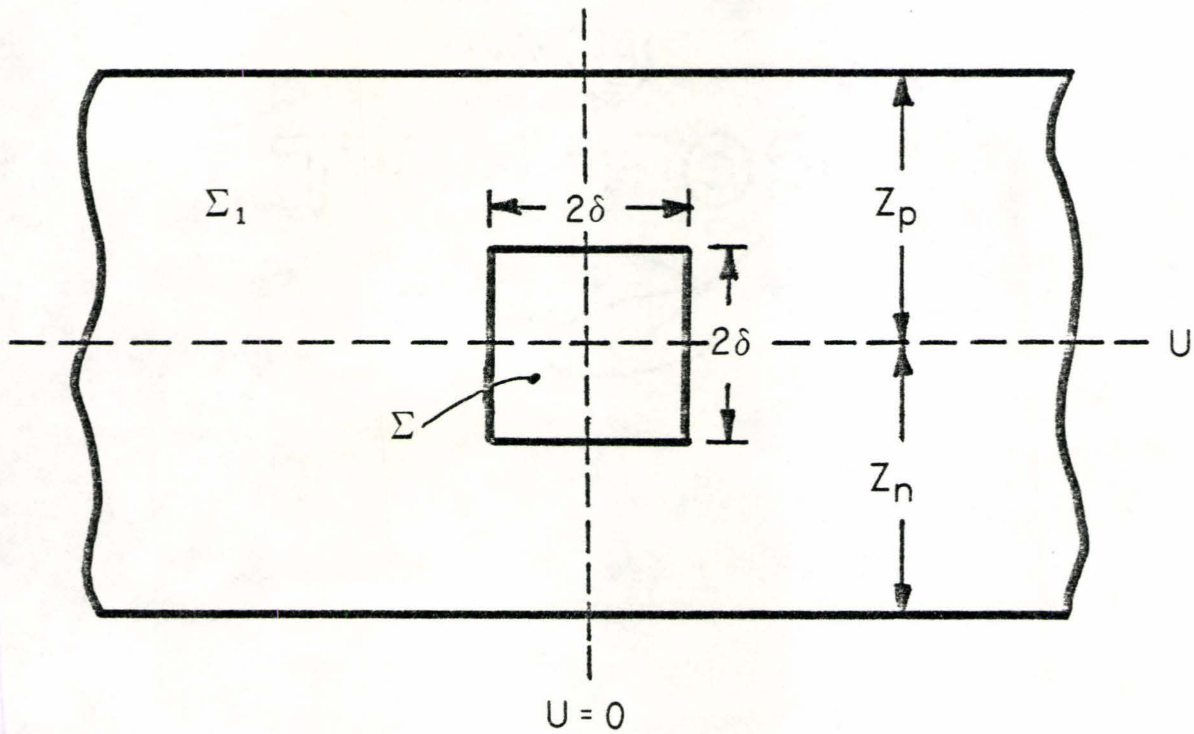

Fig. 3-3: The block approximation for resolution studies.

Thus, the equation to be solved for ε becomes

$$g(\varepsilon;\vec{p}) - S_{1/2}$$

$$= e^{-\Sigma_1 z}\{1 + \frac{\alpha}{\pi}[t(-\delta)|_\varepsilon - t(\delta)|_\varepsilon\} - e^{-\Sigma_1 z}\{1 + \frac{\alpha}{\pi}t(-\delta)|_o\}$$

$$\rightarrow t(-\delta)\Big|_\varepsilon - t(\delta)\Big|_\varepsilon - t(-\delta)\Big|_o = 0$$

where $\alpha \equiv e^{-2(\Sigma-\Sigma_1)\delta} - 1$. In full form, this becomes

$$\tan^{-1}[\sqrt{C_L}(\varepsilon+\delta)] - \tan^{-1}[\sqrt{C_L}(\varepsilon-\delta)] - \tan^{-1}[\sqrt{C_L}\delta] = 0 \qquad (3.10)$$

Obviously, this will require numerical solution; however it is a relatively simple matter, using bisection or other techniques, to prepare tables and charts of R as a function of object dimensions. A sample is shown in figure 3-4.

The interesting thing to note about equation (3.10) is the non-appearance of material parameters, specifically the cross-sections Σ and Σ_1. There are a number of possible conclusions one might reach using this fact: first it could mean that resolution, as defined here, is material-independent, i.e. particles of different materials but with similar dimensions can be detected to the same extent. A discussion of this idea will be postponed until a more general version of the preceding ideas is developed. In addition to re-deriving equation (3.10) this approach will more clearly illustrate some of the physical aspects of this theory.

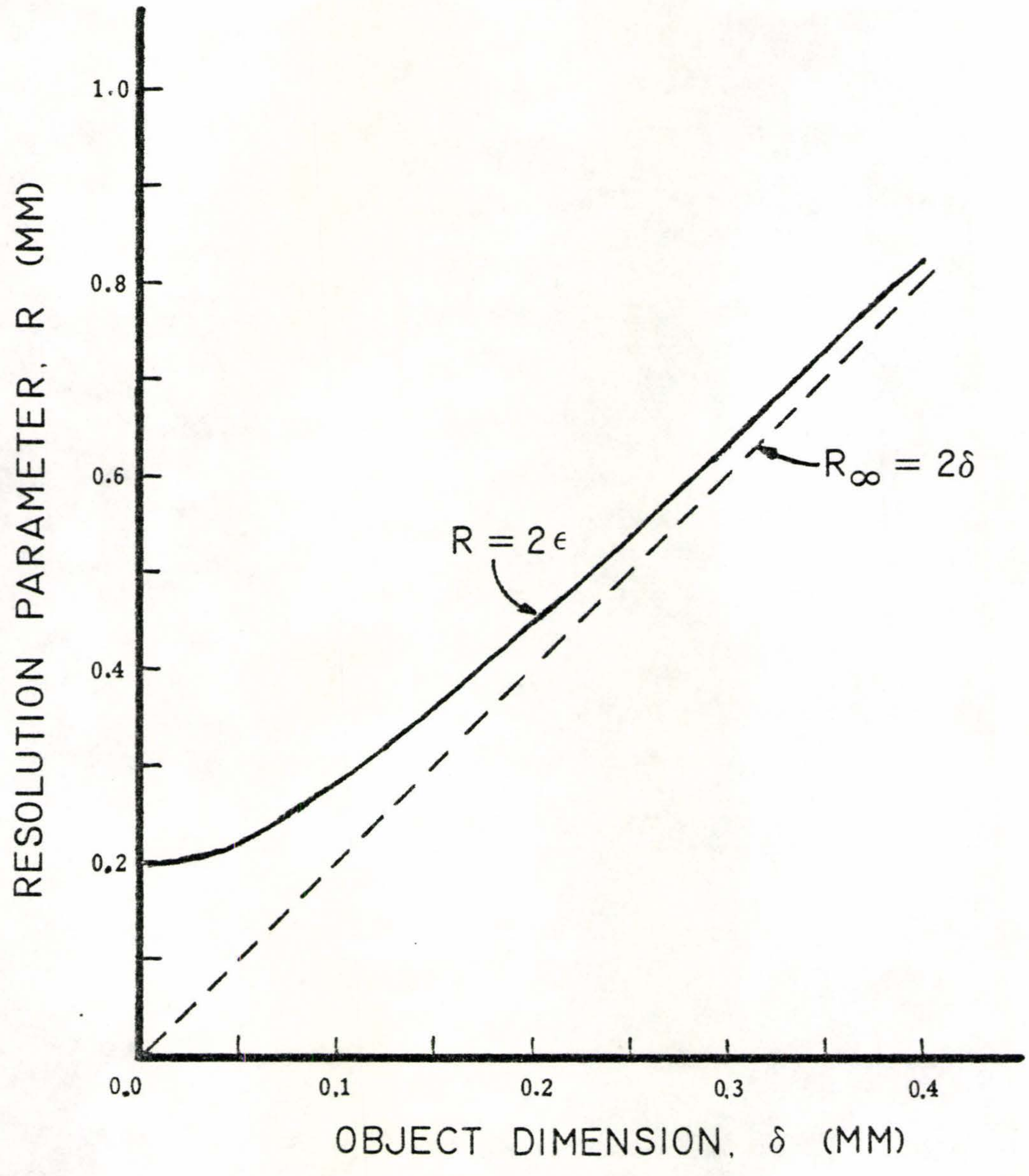

Fig. 3-4: Resolution as a function of particle dimensions, for a small "block" object. R_∞ represents the asymptotic value of the resolution as the object becomes large.

Consider equation (3.5) again; this time, the expression for $S_{1/2}$ is written in all generality, so that for symmetric objects one obtains

$$
\begin{aligned}
S_{1/2} &\equiv \frac{1}{2}\{\mathrm{Max}[S_A] + \mathrm{Min}[S_A]\} \\
&= \frac{1}{2}\{1 + S_A(0)\} \\
&= \phi_m \left\{ 1 + \frac{1}{2\pi}\left[t(\delta)\big|_o - t(-\delta)\big|_o\right] + \frac{\sqrt{C_L}}{2\pi}\int_{-\delta}^{\delta} L(0,u)\phi(u)du \right\}
\end{aligned} \tag{3.11}
$$

Thus, ε can be calculated from

$$S_A(\varepsilon) - S_{1/2} = 0$$

or in full form,

$$t(\delta)\big|_\varepsilon - t(-\delta)\big|_\varepsilon + t(-\delta)\big|_o + \sqrt{C_L}\int_{-\delta}^{\delta}\left[L(\varepsilon,u) - \frac{1}{2}L(0,u)\right]\phi(u)du = 0 \tag{3.12}$$

Clearly, solving for the full-width parameter has become a more difficult matter because of the presence of the integral term; however, it remains a fairly straight-forward problem. The problem to be examined here is the case where $\phi(u)$ is constant, say with a value ϕ_o. When this is used in equation (3.12), one can show that the resulting equation for ε is

$$(1-\phi_o)\{t(\delta)\big|_\varepsilon - t(-\delta)\big|_\varepsilon + t(-\delta)\big|_o\} = 0$$

The trivial result is that ϕ_o is unity; this implies that there is no object attenuation, hence no half-width. This is reassuring, since it suggests that the model does not predict a less-than-full convertor response for an absence of material.

A somewhat more useful result is that equation (3.10) re-appears; again, the implied result is a material independence. If one considers this from a "dual" viewpoint, the concept makes sense: while the depth of a line scan depression will be very dependent on material properties, the full-width at half-maximum will be material independent. This is a logical conclusion, because it is the width of a curve which is determined by the convertor screen isotropism; the converter does not affect the number of incoming particles (which determines the extent of film blackening), but it does (indirectly) affect the spatial distribution of these particles.

It is of some interest to note that this result can be obtained in yet another manner by considering the "re-normalized" converter response, $\tilde{S}_A(x)$:

$$\tilde{S}_A(x) \equiv \frac{S_A(x) - \min\,[S_A]}{\max[S_A] - \min[S_A]} \tag{3.13}$$

For constant attenuation, this becomes

$$\tilde{S}_A(x) = \frac{S_A(x) - S_A(0)}{1 - S_A(0)}$$

It is not hard to see that for any geometry,

$$\tilde{S}_A(\varepsilon) = 1/2$$

This can be shown by substituting equation (3.11) into equation (3.13). Also, $\tilde{S}_A$ is "depth-independent" in that it is always contained in the range (0,1.0). Considering the case of constant attenuation, one obtains

$$\frac{t(-\delta)|_{\varepsilon} - t(\delta)|_{\varepsilon}}{2t(-\delta)|_{o}} = \frac{1}{2}$$

which is clearly material independent unless C_L is a function of material properties. It appears that there is considerable justification for the idea of material independence of R; however, note that this may not be the case if $\phi(u)$ is not constant.

Continuing with the theory, another approach to resolution will be considered. In image analysis, occasional use is made of an idea called "lines per length"; this means that given an object such as a graticule, a limit can be placed on the smallest line-width which can be distinguished in either the image or a line-scan. From this, one can determine the maximum number of lines which can be visualized per unit length.

To set up a descriptive framework, consider the geometry shown in figure 3.5. By the usual methods, the convertor response function is shown to be

$$S_A(x) = e^{-\Sigma_1 z} \{1 + \frac{1}{\pi}(\alpha-1)[t(-2\delta - d) - t(-d) + t(d) - t(d + 2\delta)]\} \tag{3.14}$$

where $\alpha \equiv \exp[-2(\Sigma-\Sigma_1)\delta]$.

In this case, a useful quantity to work with might be the response difference defined by

$$\Delta S \equiv S_{max} - S(0) \tag{3.15}$$

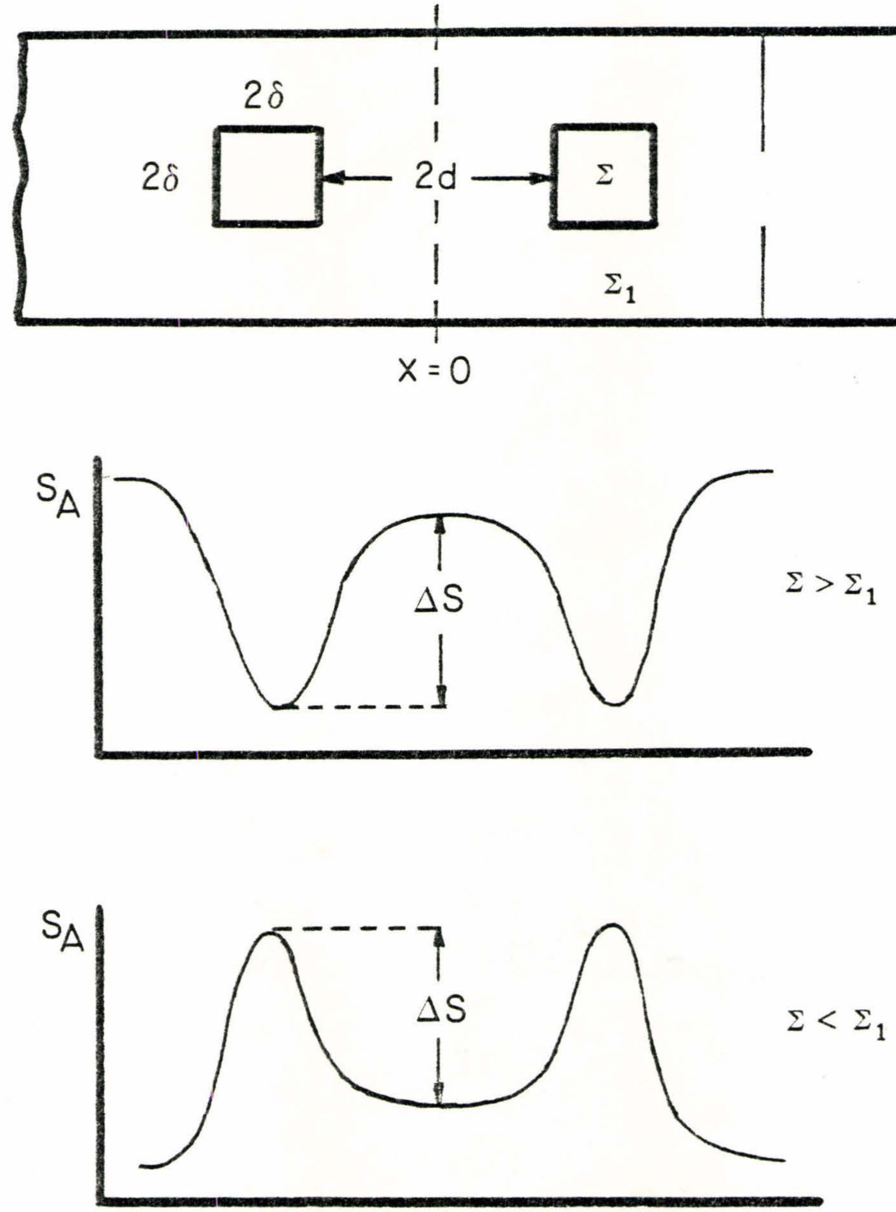

Fig. 3-5: Notation used in a convertor response difference analysis.

For example, if the values of d and δ are known, then one can determine which deviations in a line-scan correspond to particles of these dimensions. Conversely, if ΔS is known, then one can estimate the size of the particles or the distance between them, so that a resolution parameter might be specified.

Now, there are two cases to consider, in terms of the cross-sections Σ and Σ_1; these are also illustrated in figure 3-5. From equation (3.14), it is a simple matter to show that

$$S(0) = e^{-\Sigma_1 z} \{1 + \frac{1}{\pi} (\alpha - 1)[t(-2\delta - d)|_0 - t(-d)|_0 + t(d)|_0 - t(d + 2\delta)|_0]\} \tag{3.16a}$$

and

$$S_{max} = \begin{cases} e^{-\Sigma_1 z} \{1 + \frac{1}{\pi} (\alpha-1)[t(-2\delta - d)|_{d+\delta} - t(-d)|_{d+\delta} \\ \quad + t(d)|_{d+\delta} - t(d + 2\delta)|_{d+\delta}] , \ \Sigma < \Sigma_1 \\ \\ e^{-\Sigma_1 z}, \ \Sigma > \Sigma_1 \end{cases} \tag{3.16b}$$

Thus, the response difference becomes

$$\Delta S = \begin{cases} \frac{-e^{-\Sigma_1 z} (1-\alpha)}{\pi} \{t(-2\delta - d)|_{d+\delta} - t(-d)|_{d+\delta} = 2t(\delta) \\ \qquad - 2t(d)|_0 + 2t(d + 2\delta)|_0 , \ \Sigma < \Sigma_1 \\ \\ \frac{2e^{-\Sigma_1 z} (1-\alpha)}{\pi} \{t(-2\delta - d)|_0 - t(-d)|_0\}, \ \Sigma > \Sigma_1 \end{cases} \tag{3.17}$$

$$\equiv \begin{cases} f_1(d,\delta), & \Sigma < \Sigma_1 \\ f_2(d,\delta), & \Sigma > \Sigma_1 \end{cases} \tag{3.18}$$

This can be put into a slightly more general form by using

$$1 - \alpha \simeq 2(\Sigma-\Sigma_1)\delta$$

Substituting in equations (3-13) and re-arranging results in

$$\frac{\pi\Delta S}{2(\Sigma-\Sigma_1)e^{-\Sigma_1 z}} = \begin{cases} f_1(d,\delta), & \Sigma < \Sigma_1 \\ f_2(d,\delta), & \Sigma > \Sigma_1 \end{cases} \tag{3.19}$$

or, more generally

$$G_o = g_2\ (d,\delta) \tag{3.20}$$

where the generalized response difference, G_o, is defined by

$$G_o = \frac{\pi\Delta S}{2(\Sigma - \Sigma_1)e^{-\Sigma_1 z}}$$

and $g_2(d,\delta)$ is defined according to the relative values of the cross-sections. Such a definition is not absolutely essential of course, but it is judged to be better in terms of generality of application: G_o can be calculated as a function of either dimensions or materials.

To obtain a feeling for the physical significance of G_o, some of the limiting cases are considered. First, it is clear from equation (3.17) that for either case of relative cross-sections, $G_o \propto \delta$: as δ tends to zero, ΔS will also tend to zero, since there is no beam attenuation by particle matter, and as δ becomes large, ΔS also becomes large because there is more beam attenuation.

The variation of G_o with d depends on the relative size of Σ and Σ_1: if $\Sigma > \Sigma_1$, then as d becomes large, there is a larger region of lower cross-section material for the beam to pass through, resulting in less attenuation. Conversely, if $\Sigma < \Sigma_1$ there will be more beam attenuation. These results are summarized below:

$$G_o \;\alpha\; \Delta S \;\alpha \begin{cases} {}^{\delta}/d, & \Sigma > \Sigma_1 \\ \delta d, & \Sigma < \Sigma_1 \end{cases} \tag{3.21}$$

Note that for the case of no particles, i.e. where there is a single continuous medium, G_o is zero. This is the expected result, since an absence of material cannot cause beam attenuation. A sample graph of G_o is presented in figure 3-6.

Two points should be made before moving on to the next topic: first, it is clear that a "lines-per-length" parameter can be easily calculated using the methods of this section. Basically, all one need do is obtain the value of G_o, and determine the appropriate value of d either by numerical solution of equation (3.17) or from a graph similar to figure 3-6. Then, the parameter is easily shown to be

$$\text{LPL}(\Delta S) \equiv \text{lines per length for a given response difference} = \frac{1}{d^*} \tag{3.22}$$

where d* is the value of the line width obtained from G_o. Technically, one should consider a sequence of particles and spacings rather than the simplified geometry discussed here, since for smaller values of d and δ the secondary radiation transport effects of the other nearby object/gap pairs may become significant; however, the calculation

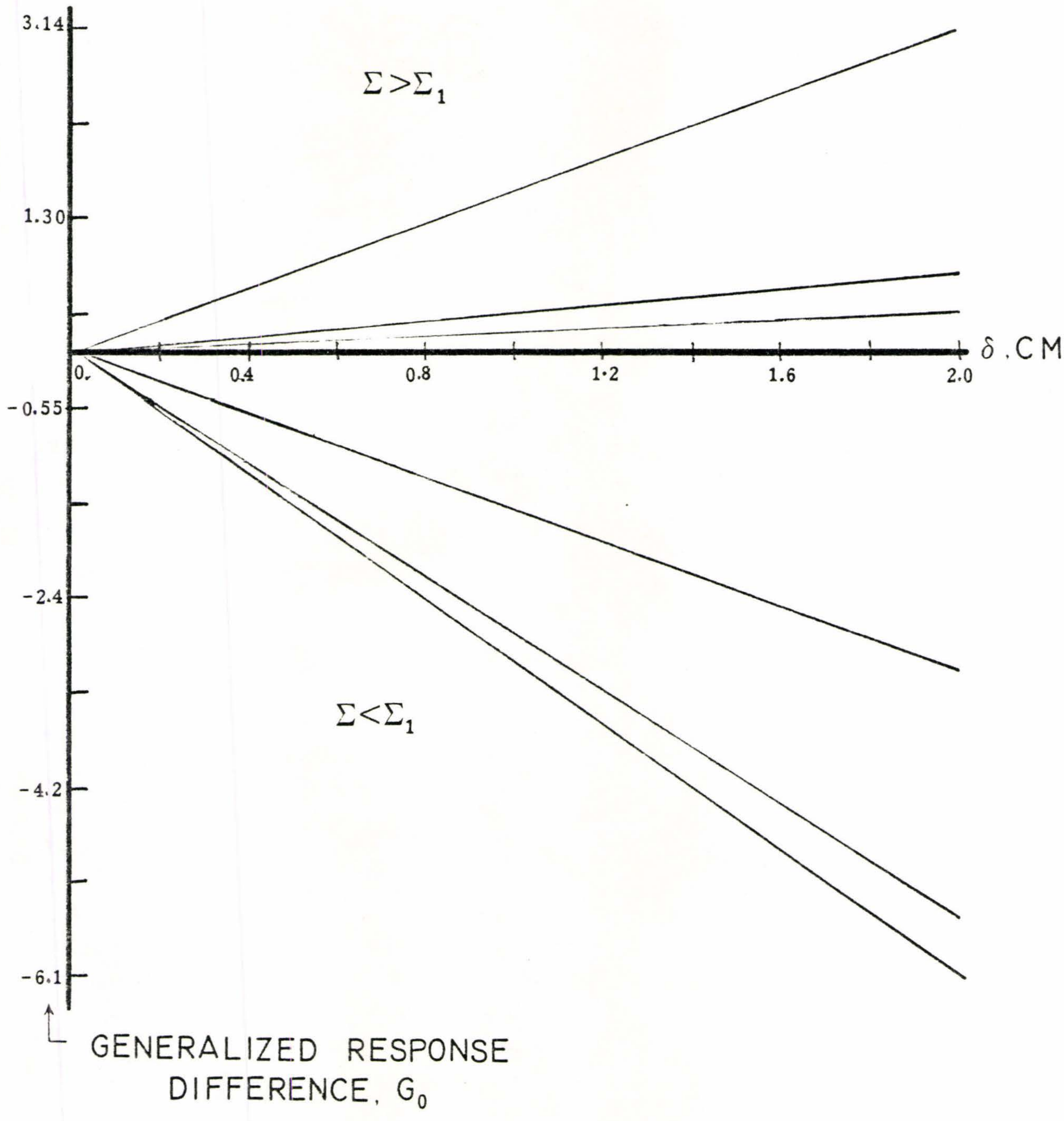

Fig. 3-6: A sample graph of the generalized response difference G_0, as a function of particle dimension and separation, and relative values of the particle and medium cross-sections.

procedure discussed here should prove useful as a first approximation.

This brings up the remaining point, which is a note of caution: in order to simplify the calculations involved, the so-called "block" approximation has been used. Now the use of constant cross-sections is of no great importance, since if necessary one can define average cross-sections such that

$\overline{\Sigma}$ = spatially averaged macroscopic cross-section

However, the important idea to note is that of using a block to approximate other shapes; for very small objects, the approximation will be excellent, while for large objects the matter of resolution is unimportant. Thus, problems arise in the intermediate range of particle sizes, and as a possible solution it is suggested that δ be determined thus: if the true particle shape is known, then it should be possible to determine an average dimension $\overline{\delta}$ such that

$2\overline{\delta} \equiv$ spatial average of object thickness

For example, if the object is circular, with radius R, one could use the root-mean-square thickness $\sqrt{2}\,R$. Of course, if extreme accuracy is required, one can go through the process of detailed solution of equation (3.4); however, it is doubtful whether any significant gains in accuracy will be achieved in return for the effort put into the necessary computing. In addition, numerical error will probably compound the difficulties encountered.

3.2 ESF Theory of Unsharpness Analysis

In this section, the ESF technique will be extended to include other factors which create uncertainty in optical density measurements; as will become apparent, the effects due to the spreading of secondary radiation about the point of neutron impact are part of a larger class of factors which all have the same end result, namely image blurring, or "unsharpness". Logically, the combined effect of these factors is called the total unsharpness.

The initial theoretical work for this section can be found in reference 5; thus, only an outline will be provided here. The basic idea is that instead of only considering convertor screen effects ("screen unsharpness"), one modifies the LSF to include other effects such as motion and geometric unsharpness. This is easily done by transforming the LSF thus:

$$L(x,u) \rightarrow L(x,\alpha)$$
$$\alpha = u + \mu + vt' + \ldots \tag{3.23}$$

where μ is a geometric unsharpness factor, t' is time, and v is the velocity of the object at time t' (t' is used for time so as to distinguish it from the inverse tangent function). Here, u is the same spatial co-ordinate used previously. Thus, the modified convertor response becomes

$$S_A^{\alpha}(x) = N_{\alpha} \int_{\alpha_0} L(x,\alpha)\phi(\alpha)d\alpha \tag{3.24}$$

where N_α is the appropriate normalization constant, and α_o is the phase-space region of integration. Usually, only screen, motion, and geometric unsharpness are considered, so that the response becomes

$$S_A^{s,m,g}(x;\mu_m,\tau) = \frac{\sqrt{C_L}}{\pi\mu_m\tau}\int_{\mu=o}^{\mu_m}\int_{t'=o}^{\tau}\int_{u=-\infty}^{\infty} L(x,u+vt'+\mu)\phi(u+vt'+\mu)du dt' d\mu \quad (3.25)$$

where τ is the exposure time and μ_m is the geometric unsharpness defined by

$$\mu_m = \frac{a\ell}{L}$$

where a is the focal spot or source size, ℓ is the film-object distance, and L is the source-object distance. For neutron radiography, screen and motion unsharpness tend to be most important factors, since collimation problems are greater and thus require a small ℓ/L ratio; additionally, motion effects will in general be of less importance than screen unsharpness, because of the relatively long exposure times required in neutron radiography. Thus, the response function to be considered will be

$$S_A^{s,m}(x;\tau) = \frac{\sqrt{C_L}}{\pi\tau}\int_{t'=o}^{\tau}\int_{u=-\infty}^{\infty} L(x,u+vt')\phi(u+vt')du dt' \quad (3.26)$$

In general, it will be easier to do the spatial integration, since v(t') will not usually be a constant; thus, one can define an exposure dependent response function

$$S_A^{s,m}(x;\tau) = \frac{1}{\tau} \int_0^\tau S_A(x,t')dt' \tag{3.27}$$

where

$$S_A(x,t') = \frac{\sqrt{C_L}}{\pi} \int_{-\infty}^{\infty} L(x,u+vt')\phi(u+vt')du \tag{3.28}$$

Obviously, the calculational procedure has become much more complicated, since the possibility of an exact solution of the time integral is very small. However, it will be useful to consider an example where some applicability is evident. Using figure 3-5, the block approximation is brought into play again, so that

$$S_A(x,t') = e^{-2\Sigma_1 z} \{1. + \frac{1}{\pi} (e^{-2(\Sigma-\Sigma_1)x_0} - 1)*$$

$$[t(-x_0 + t'v(t')) - t(x_0 + t'v(t'))]\} \tag{3.29}$$

An interesting case will be where $v(t')$ is sinusoidal; for example, this could represent the vibration of a machine part or the motion of a body organ or blood vessel. One will often be interested in locating the edge of the object; thus, let the convertor response at x_0 be re-defined as

$$\begin{aligned} S_0(\tau) &= S_A^{s,m}(x_0;\tau) \\ &= \frac{1}{\tau} \int_0^\tau S_A(x_0,t')dt' \end{aligned} \tag{3.30}$$

In full form, with $v(t') = v_0 \sin(wt')$, this becomes

$$S_o(\tau) = \frac{\phi_o}{\tau} \int_0^{\tau} \{1 + \frac{1}{\pi}(\phi_1 - 1)]t(-x_o + t'v_o \sin(wt'))\Big|_{x_o} \tag{3.31}$$

$$- t(x_o + t'v_o \sin(wt'))\Big|_{x_o}]\}dt'$$

Clearly, this enables one to locate the edge of an object in a line-scan when sinusoidal motion is involved.

It is interesting to note that in the limiting case of very long exposure times, $S_o(\tau)$ takes on a value which is independent of the object motion. This is easily shown by the following procedure: let the edge response at time τ be

$$S_o(\tau) \equiv \frac{1}{\tau} \int_0^{\tau} g_3(x_o, t'; \vec{p})dt' \tag{3.32}$$

where $g_3(x_o, t'; \vec{p})$ is defined by equation (3.29). Then, the limiting value is given by

$$\lim_{\tau \to \infty} S_o(\tau) = \lim_{\tau \to \infty} \left\{ \frac{\int_0^{\tau} g_3(xo, t'; p)dt'}{\tau} \right\}$$

$$= \lim_{\tau \to \infty} \frac{\partial}{\partial \tau} \int_0^{\tau} g_3(x_o, t'; \vec{p})dt' \tag{3.33}$$

where L'Hospital's rule has been used in the second equation. Invoking Leibnitz's rule, this becomes

$$\lim_{\tau \to \infty} \left\{ \int_0^{\tau} \frac{\partial}{\partial \tau} g_3(x_o, t'; p)dt' + g_3(x_o, \tau; \vec{p}) \frac{\partial(\tau)}{\partial \tau} - g_3(x_o, 0; p)\frac{\partial(0)}{\partial \tau} \right\}$$

$$= \lim_{\tau \to \infty} g_3(x_o, \tau; p) \tag{3.34}$$

since $g_3(x_o,t';\vec{p})$ is independent of τ. In addition, one must consider the velocity, $v(t')$; however, it is arguable that in practical cases $v(\tau)$ will have some finite and fixed value, say v_τ. Armed with this rather empirical fact, inspection of equation (3.29) shows the final result to be

$$\lim_{\tau\to\infty} S_o(\tau) = \phi_o \equiv e^{-2\Sigma 1 z} \tag{3.35}$$

This value is feasible on the grounds that regardless of the form of the object motion, at or about the edge, the attenuation will be for the most part due to the medium surrounding the object; thus over long periods of time, the cumulative effect on the convertor response should be due to the surrounding medium, and a time-averaged form of the edge motion.

A result which may be of some interest can be obtained for cases where $S_A(x,t')$ is periodic:

$$S_A(x,t' + nT) = S_A(x,t') \tag{3.36}$$

with T being some characteristic time. Assume for generality that the exposure time τ is such that

$$\tau = NT + \delta\tau$$

It is not hard to see that the exposure dependent response can now be written as

$$S_A^{s,m}(x;\tau) = \sum_{i=1}^{N}\left\{\int_{(i-1)T}^{iT} S_A(x,t')dt'\right\} + \int_{NT}^{NT+\delta\tau} S_A(x,t')dt' \tag{3.37}$$

In the first N integrals, the substitution used is

$$t' = w + (i-1)T$$

while in the last integral, one uses

$$t' = w + NT$$

The result is

$$\tau S_A^{s,m}(x;\tau) = \sum_{i=1}^{N} \left\{ \int_0^T S_A(x,w + (n-1)T)dw \right\} + \int_0^{\delta\tau} S_A(x,w + NT)dw \qquad (3.38)$$

However, using equation (3.36), this reduces to

$$S_A^{s,m}(x;\tau) = \frac{N}{NT+\delta\tau} \int_0^T S_A(x,t')dt' + \frac{1}{NT+\delta\tau} \int_0^{\delta\tau} S_A(x,t')dt' \qquad (3.39)$$

(where the dummy variable w has been changed back to t'.) Note that for $\delta\tau = 0$, this further reduces to

$$S_A^{s,m}(x;\tau) = \frac{1}{T} \int_0^T S_A(x,t')dt' \qquad (3.40)$$

This again suggests that for some situations, the response may be independent of exposure time. However, cases where $S_A(x,t')$ is periodic are expected to be rare, hence this result will not be considered any further.

It is of some interest to continue the unsharpness analysis in a manner parallel to that used in the resolution analysis of section 3.2;

thus consider the block geometry of figure 3-7, where in this instance the object moves with some velocity $v(t')$. The block edges are located spatially by $x(t')$ and $x(t') + 2\delta$, as indicated; this can be put into a more relevant form however, by defining $x(t')$ by

$$x(t') = x_o + t'v(t') \tag{3.41}$$

Thus, the time-dependent convertor response becomes

$$S_A(x,t') = \phi_o \{1 + \frac{1}{\pi} (\phi_1 - 1)[t(-x_o + t'v(t')) - t(x_o - t(x_o + 2\delta + t'v(t'))]\} \tag{3.42}$$

Specifying the integral limits to be time-dependent in this manner is perhaps a more rigorous way of bringing motion unsharpness into the analysis than just arbitrarily defining the variables of interest. Clearly then, the exposure-dependent response becomes

$$S_A^{s,m}(x;\tau) = \frac{1}{\tau} \int_0^\tau g(x,t';\vec{p})dt' \tag{3.43}$$

Now, let the response at half-maximum be

$$S_{1/2} \equiv 1/2 \{Max[S_A(x,t')] + Min[S_A(x,t')]\} \tag{3.44}$$

where the extrema are determined with respect to x, and the values of x corresponding to $S_{1/2}$ are $x = \pm \varepsilon_\tau$. (Symmetry is assumed for simplicity). Clearly then, in analogy to equation (3.5), ε_τ is obtained by solving

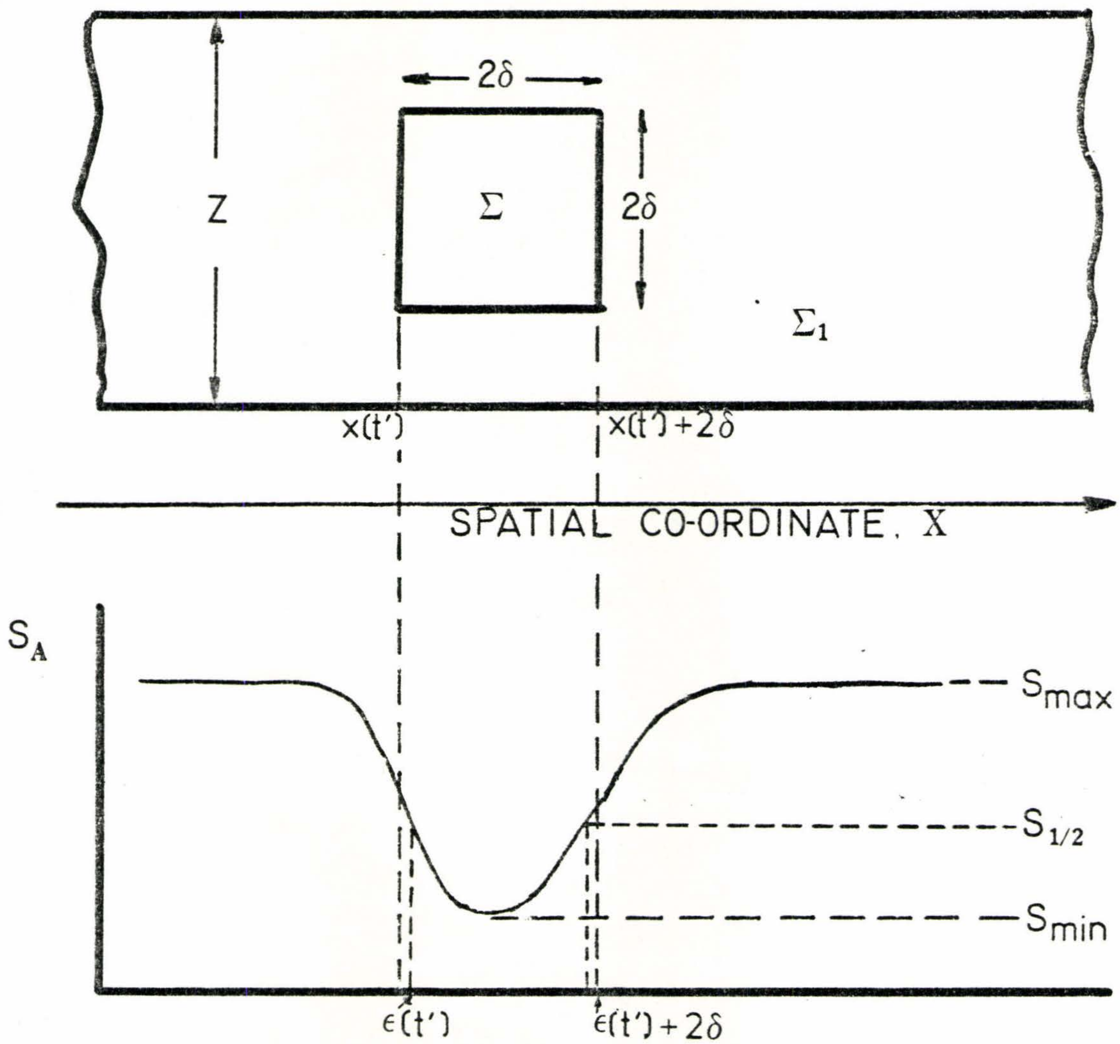

Fig. 3-7: The block approximation for an exposure-dependent resolution analysis. Note that the location of the blocks edges is a function of time.

$$\frac{1}{\tau} \int_0^{\tau} g(\varepsilon_\tau, t'; \vec{p})dt' - S_{1/2} = 0 \tag{3.45}$$

which then gives the exposure-dependent resolution parameter

$$R(\tau) = 2\varepsilon_\tau \tag{3.46}$$

It is not difficult to extend these ideas to the full phase-space definition of unsharpness; if the convertor response is given by

$$\begin{aligned} S_A^{\alpha}(x;\alpha_o) &= N_\alpha \int_{\alpha_o} S_A(x,\alpha)d\alpha \\ &\equiv N_\alpha \int_{\alpha_o} g(x,\alpha;\vec{p})d\alpha \end{aligned} \tag{3.47}$$

then once $S_{1/2}$ is determined, the generalized resolution parameter $R(\alpha_m)$ can be calculated by solving

$$N_\alpha \int_{\alpha_o} g(\varepsilon_\alpha, \alpha; \vec{p})d\alpha - S_{1/2} = 0 \tag{3.48}$$

It should be noted here that the block approximation was not at all essential to this part of the analysis; the response function can be defined for any geometry, even if it cannot be put into closed form, and thus the function $g(\varepsilon_\alpha, \alpha; \vec{p})$ can be defined, so that equation (3.45) can be formed in complete generality. The advantage of the block approximation is that for certain cases it is useful in giving one a feel for the physical aspect of the discussion, rather than leaving one to flounder about in parameter-space. Additionally, it is the simplest form for obtaining numerical values without excessive computational work. Thus, the approximation will continue to be prominent in the analysis.

Continuing with the scheme of discussion outlined in section 3.2, the idea of an exposure-dependent response difference is considered. Using equation (3.14), and letting

$$d \to d(t') \equiv d + t'v(t') \tag{3.49}$$

the appropriate response function then becomes

$$S_A^{s,m}(x;\tau) = \frac{1}{\tau} \int_0^{\tau} \phi_o \{1 + \frac{1}{\pi} (\phi_1 - 1)[t(-2\delta - d) - t(-d) + t(d) - t(2\delta + d)]\} dt'$$

$$\equiv \frac{1}{\tau} \int_0^{\tau} \phi_o \{1 + \frac{1}{\pi} (\phi_1 - 1) h(x,t';\vec{p})\} dt' \tag{3.50}$$

Let the exposure-dependent response difference be defined by

$$\Delta S(\tau) = \mathrm{Max}[S_A^{s,m}(x;\tau)] - S_A^{s,m}(0;\tau) \tag{3.51}$$

where the maximization is again taken with respect to x. Again, the relative values of Σ and Σ_1 must be considered, which gives the following results:

$$S_A^{s,m}(0;\tau) = \frac{1}{\tau} \int_0^\tau \phi_o \{1 + \frac{1}{\pi} (\phi_1 - 1) h(0,t',\vec{p})\} dt'$$

$$\mathrm{Max}[S_A^{s,m}(x;\tau)] = \begin{cases} \phi_o, & \Sigma > \Sigma_1 \\ \frac{1}{\tau} \int_0^\tau \phi_o \{1 + \frac{1}{\pi} (\phi_1 - 1) h(d+\delta,t';\vec{p})\ dt', & \Sigma < \Sigma_1 \end{cases} \tag{3.52}$$

Substituting these results into equation (3.51) gives

$$\Delta S(\tau) = \begin{cases} \frac{-\phi_o}{\tau} \left(\frac{\phi_1 - 1}{\pi}\right) \int_0^\tau h(0,t';\vec{p}) dt', & \Sigma > \Sigma_1 \\ \frac{\phi_o}{\tau} \left(\frac{\phi_1 - 1}{\pi}\right) \int_0^\tau \{h(d+\delta,t';\vec{p}) - h(0,t';\vec{p})\} dt', & \Sigma < \Sigma_1 \end{cases} \tag{3.53}$$

As in the static case, assume that

$$\phi_1 \equiv e^{-2(\Sigma-\Sigma_1)\delta} \simeq 1 - 2(\Sigma-\Sigma_1)\delta$$

Then taking all parameters except d, δ, and τ to the left hand side, one obtains

$$\frac{\pi\ \Delta S(\tau)}{2(\Sigma-\Sigma_1)e^{-2\Sigma_1 z}} = \begin{cases} \frac{\delta}{\tau} \int_0^\tau f_1(d,\delta,t') dt', & \Sigma > \Sigma \\ \frac{\delta}{\tau} \int_0^\tau f_2(d,\delta,t') dt', & \Sigma < \Sigma_1 \end{cases} \tag{3.54}$$

or more generally,

$$G_o(\tau) = \frac{1}{\tau} \int_0^{\tau} g_2(d,\delta,t')dt' \tag{3.55}$$

Continuing the generalization, in parametric phase-space this becomes

$$G_o(\alpha_m) = N_\alpha \int_{\alpha_o} g_2(d,\delta,\alpha)d\alpha \tag{3.56}$$

Clearly, a generalized response difference is easily obtained even without specifying geometry and/or material composition; however, caution must be used, since the separation of material and dimensional properties may not always be possible. For example, the block approximation makes use of a truncated series expansion for ϕ_1; in general, however, this may not be possible, and thus, the function $g_2(d,\delta,\alpha)$ may contain an explicit dependence on material properties, instead of the implicit dependence exhibited by the block approximation. This notwithstanding, it remains a straightfoward, if non-trivial, matter to evaluate $G_o(\alpha_m)$.

This concludes the examination of ESF theory as applied to the general unsharpness problem. It appears that the Lorentzian form for the LSF leads to a fairly easily manipulated mathematical structure, although the end results are not always amenable to analytic solution. Despite their apparent complexity, even the more complex combinations of geometry and material properties are readily attacked with numerical techniques, and thus a more detailed study, from both theoretical and experimental viewpoints, is suggested as one area for future investigation.

4. EXTENSIONS AND VARIATIONS

An idea that should be quite apparent from the previous chapters is the fact that this theory depends very much on the use of the Lorentzian form for the line-spread function. The results to date have indicated that this is a good model, but this has been more or less the only reason for using this function: an empirical decision has been made, based on experimental results(1). This of course is not at all a bad reason for choosing a model; however, it is a somewhat unsatisfactory reason (at least to this author). In addition, other methods may provide the means of satisfactorily dispatching some of the gremlins encountered in earlier chapters (in particular, the Lorentzian coefficient). The point to be made is that there may exist other more basic methods of analysis which do not require an intricate mathematical formulation; the next sections will deal with two of these alternative approaches.

4.1 Numerical Methods

While it is always both pleasant and useful to have a structured model for one's analysis, it is neither always possible nor entirely necessary. In addition, the use of an "equation-free" approach means it may be possible to analyze complex phenomena without resorting to any of the more annoyingly complicated mathematical techniques.

In this section the use of a strictly numerical procedure will be very briefly examined. This method is truly model-independent, in the sense that one is working entirely with experimental results; furthermore, it results in a true lumped parameter approach, because all object and radiographic facility properties are blended together in the data.

There are drawbacks, of course: it may be more difficult to get a feeling for one's results, and the initial investment in terms of calculation and programming effort may be quite high. However, these problems are compensated for by no longer having to explicitly account for every little quirk of the object-facility system, and by the fact that computers very readily handle this sort of problem. Another useful feature is that there exists a very highly-developed system of error analysis for numerical procedures; thus, one can easily put significant limits on the accuracy of any results obtained in this fashion. As a final note, this approach is of interest from the parallel viewpoints of old-fashioned academic curiosity and practical requirements.

Consider figure 4-1; the dashed line is an experimentally-obtained edge-spread curve, representing the optical density pattern due to an aluminum knife-edge. Note that this is an edge-spread curve, and not an edge-spread function. One can obtain a line-spread curve from these results by a simple numerical differentiation; if L and E denote the line-spread and edge-spread curves respectively, then the two are related by

$$L(x_i) = \frac{E(x_{i+1}) - E(x_{i-1})}{x_{i+1} - x_{i-1}} + O(h^2) \tag{4.1}$$

where the subscripts represent the discrete experimental values, and h is the (constant) mesh spacing. The error in this equation is of the order of h^2, as indicated. Equation (4.1) was used to generate the solid curve in figure 4.1.

This curve has some of the features of the Lorentzian LSF, in

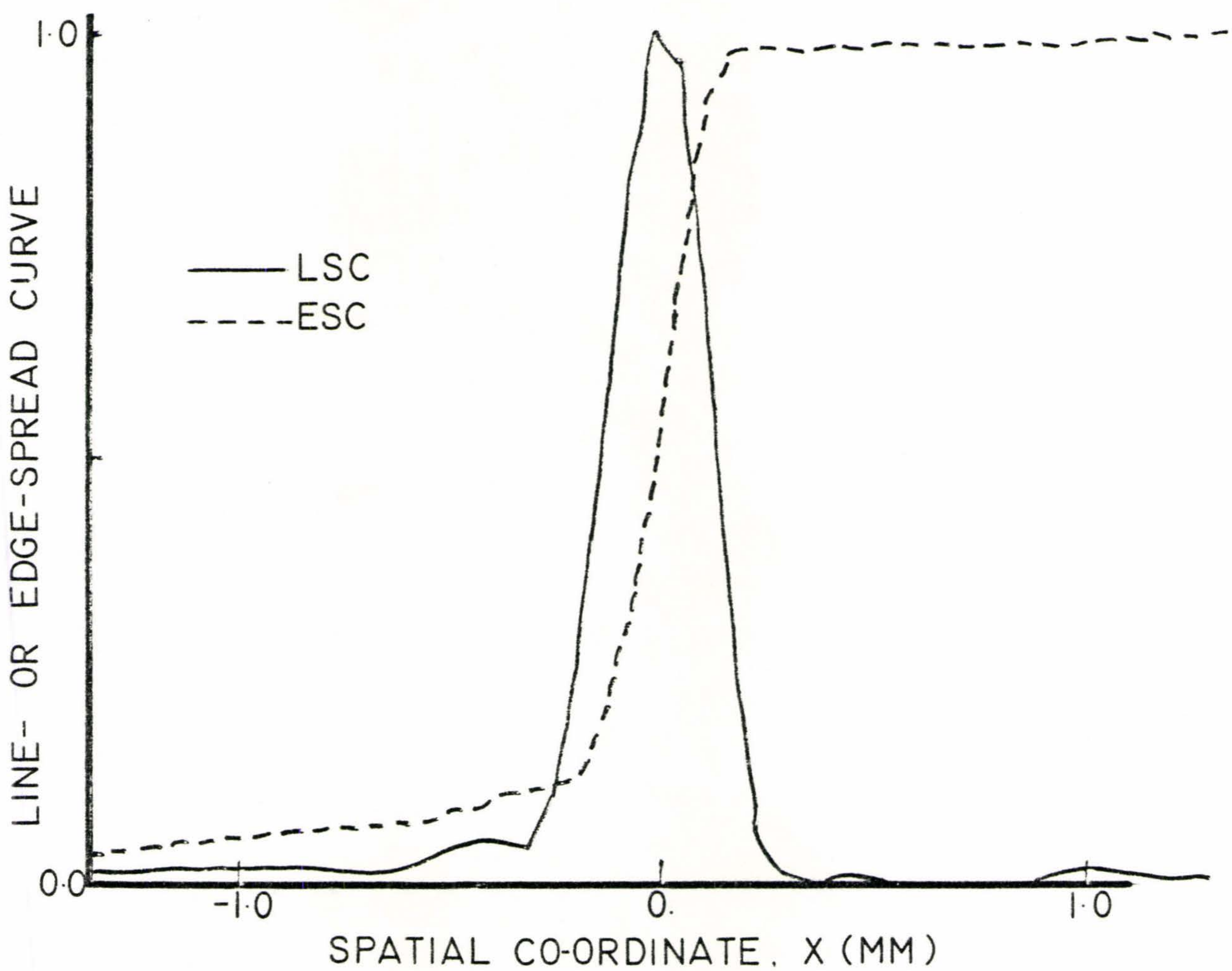

Fig. 4-1: Experimentally-obtained edge- and line-spread curves.

that there is a distinct peak, and the magnitude of the curve drops off fairly quickly as one moves away from the peak. However, there are also a number of differences between the experimental curve and the results one would obtain from a Lorentzian function. Similarly, the edge-spread curve has some features not found in a Lorentzian ESF. Hence, there are a number of conclusions one might reach from an examination of these results; because of this the method is subject to some qualitative uncertainty. Before doing any calculations, one still has to decide what the data physically represents; this is easily illustrated with the results obtained herein. First, the data will be discussed from the viewpoint of a pure thermal neutron beam. Since beam purity tests have indicated that this is not the case (cf. ref. 11), this is an obviously incorrect analysis; however, the results are interesting, and show the potential of the numerical approach, which justifies the artificial use of the data. After this, the data will be used again, this time including the effects of the beam γ-content. This more correct approach should clearly illustrate the utility of an equation-free technique when one does not have detailed knowledge of the experimental circumstances.

Consider the data, then, as if it were obtained from a radiographic facility with a pure thermal neutron beam. For convenience, the two curves have been reproduced separately in figures 4-2 and 4-3, along with the curves one would obtain from the Lorentzian functions:

$$L_L(x) = \frac{1}{1 + C_L x^2} \tag{4.2a}$$

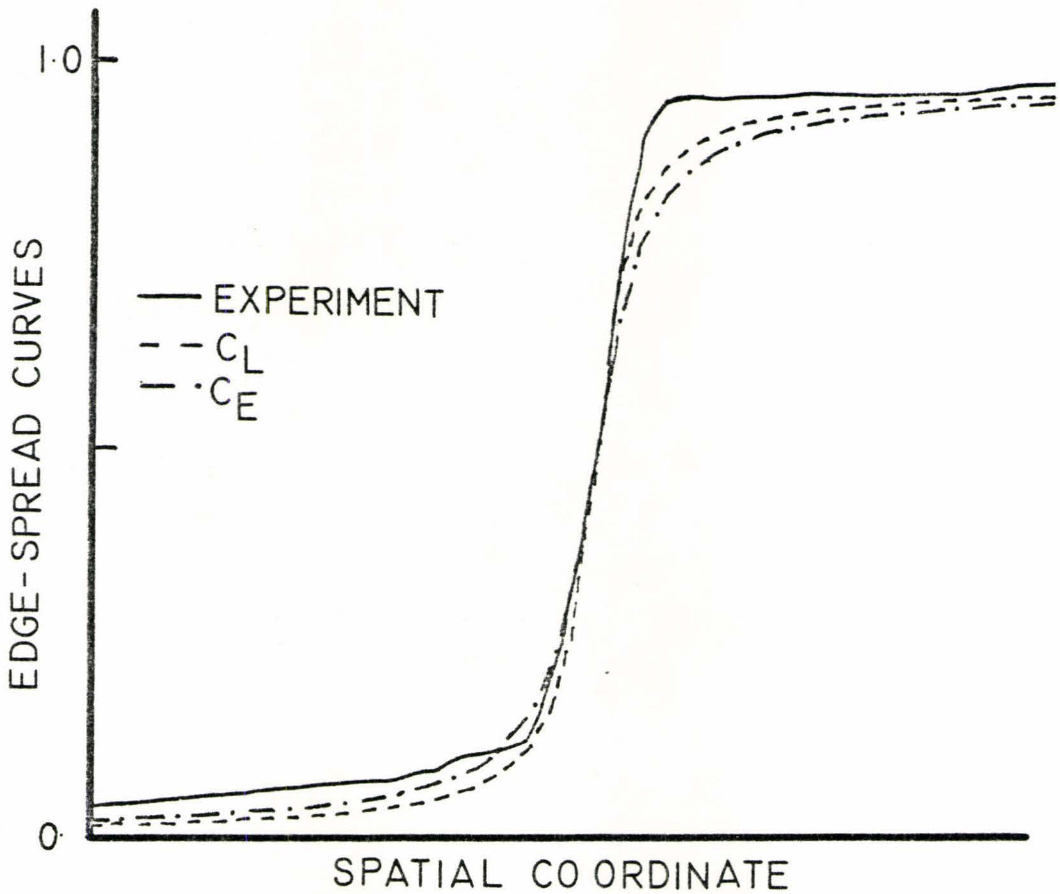

Fig. 4-2: Comparison of experimental and theoretical edge-spread curves.

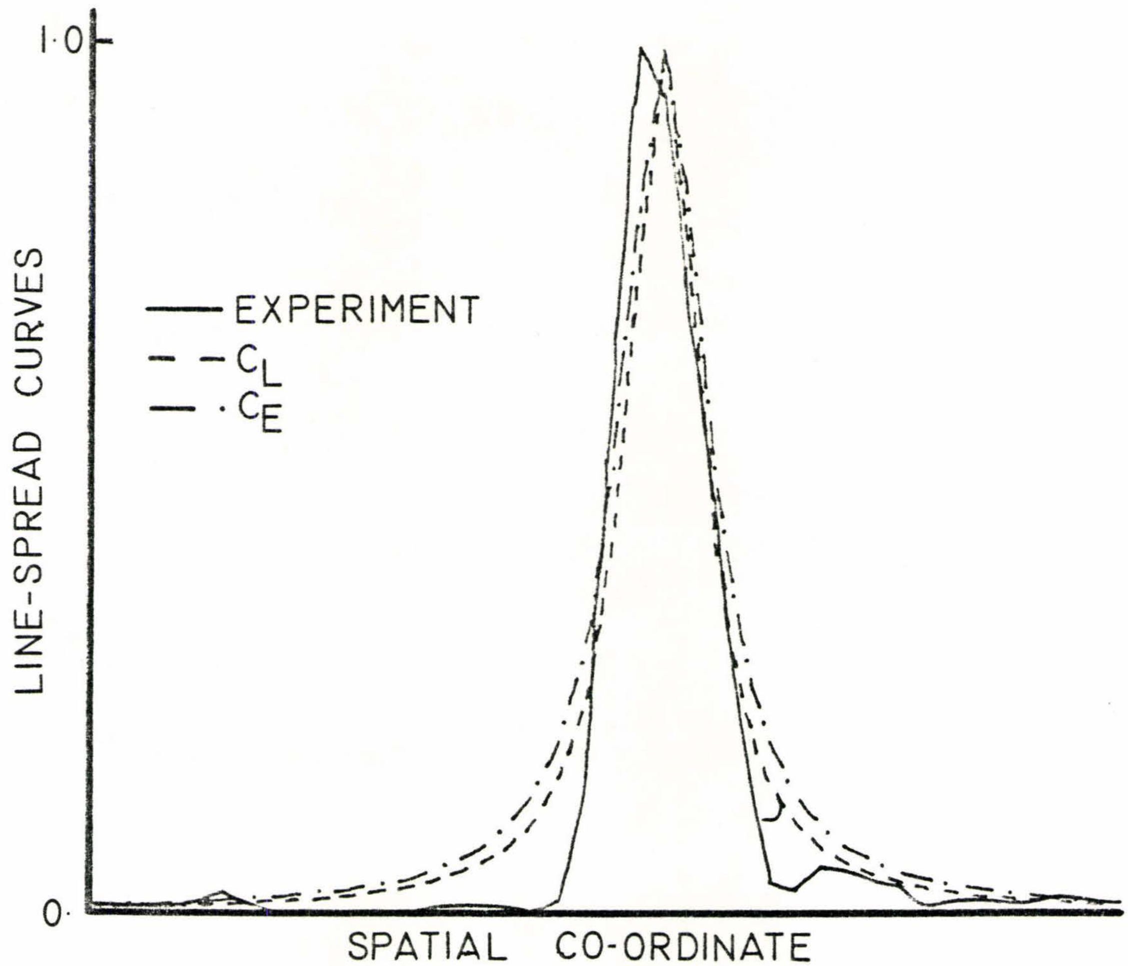

Fig. 4-3: Comparison of experimental and theoretical line-spread curves.

$$E_L(x) = \frac{1}{2} + \frac{1}{\pi} \tan^{-1} [\sqrt{C_L}\, x] \tag{4.2b}$$

For the experimental curves, let the descriptive parameter be C_E; this is the equivalent of the Lorentzian coefficient. Values for C_E can be obtained by two methods, if one assumes that the experimental results can be approximated by equations (4-2): one can calculate C_E by least squares fitting, or one can use less sophisticated techniques, which use principles similar to a Lorentzian analysis but still allow for deviations from that model.

Consider the line-spread curve and function shown in figure 4-2. The first thing one might notice is that the LSF is smoother than the experimental LSC; here, smoothness does not refer to the lack of film or other noise in the Lorentzian curve, but rather to the fact that the LSF has a non-zero value over a larger range than does the LSC. The implication here is that the spreading of the secondary radiation is more of a localized effect than the Lorentzian model predicts, and this in turn suggests that perhaps the emission of secondary radiation is not uniformly distributed in the angular variable; instead there may be a range of preferred angles, such that the probability of emission at 180° to the path of the incident neutron is higher than for other angles.

Another point of interest is that the LSC is not quite symmetric. This is of particular interest here because the nature of the Lorentzian is such that it is symmetric about the point of neutron capture. Now if one accepts the previous idea about preferred angles of secondary emission, then it is not unlikely that this emission is not symmetric about the capture point. Alternatively, one could regard this asymmetry as being due to object material effects; if there is a scattering component in the cross-section, then there should be an unbalanced neutron current at or about the knife-edge. This is because there are neutrons being scattered out of the edge face which may still interact with the convertor, but there are no neutrons travelling <u>into</u> the material.

This discussion is interesting from an abstract viewpoint in that it illustrates "what might have been"; however, it will be more instructive to consider the data in terms of what it truly represents, that is, as the physical record of an image created by a combined neutron-gamma beam. If figures 4-2 and 4-3 are re-considered in this light, then one must include the following in any conclusion: because γ-radiation interacts directly with the film emulsion, it is not subject to the convertor foil "smearing" process, hence that portion of the total image created by γ-rays more accurately represents the object shape.

To get a quantitative feel for this idea, some methods for calculating the coefficients C_L and C_E will be discussed. First, the values of C_L were calculated by least-squares fitting of a Lorentzian and an inverse tangent function to the line- and edge-spread data, respectively. Then, values for C_E were calculated in the following manner: for the line-spread data, if one assumes that a Lorentzian would at least be a good approximation to the experimental curve, then the full-width at half-maximum should be related to C_E by

$$\text{FWHM} \approx \frac{2}{\sqrt{C_E}} \tag{4.3}$$

Using linear interpolation to locate the value of x on either side of the origin for which the curve has half of its maximum value, one obtains

$$\mathrm{FWHM} = |131.64| + |-104.97|$$

$$= 236.61\ \mu\mathrm{m}$$

Note the two different values of x; this is indicative of the curve asymmetry. Using this result in equation (4.3), one obtains

$$C_E = 7.14 \times 10^{-5}\ \mu\mathrm{m}^{-2} = 7.14 \times 10^{3}\ \mathrm{cm}^{-2}$$

This value is considerably different from previously obtained values, and when used in a line-spread function will generate a curve which drops in value very rapidly as one moves away from the peak area. This does not indicate "preferred emission angles" of the secondary radiation, as discussed previously; rather, it suggests that some care is necessary in applying Lorentzian methods to situations where one does not have a pure neutron beam.

A similar result is obtained when C_E is calculated from the edge-spread data; again assuming the Lorentzian function to be an approximation, then one has the experimental data given by

$$\mathrm{ESC}(x) \approx \frac{1}{2} + \frac{1}{\pi} \tan^{-1} [\sqrt{C_E}\ x) \qquad (4.4)$$

The derivative of this function at the origin is easily shown to be

$$\frac{d}{dx} \left\{\mathrm{ESC}(x)\right\}\Big|_{x=0} = \frac{\sqrt{C_E}}{\pi} \qquad (4.5)$$

Now if one uses a difference form for the derivative, and denotes the points immediately to the left and right of the origin by -1 and +1 respectively, the result is

$$\frac{\sqrt{C_E}}{\pi} \simeq \frac{f_{+1} - f_{-1}}{x_{+1} - x_{-1}} \tag{4.6}$$

where f_i represents the value of the data at the i'th point. The end result is

$$C_E = 1.11 \times 10^{-4}\ \mu m^{-2} = 1.11 \times 10^{4}\ cm^{-2}$$

Once again the value of C_E is considerably different from previously used values, further emphasizing the need for caution in the application of Lorentzian methods.

It is of interest to note that different values of C_E are obtained from the ESC and LSC, for which there might be a number of possible reasons. First, if the assumption of a Lorentzian approximation does not hold, then there is nothing to indicate that equations (4.3) and (4.5) hold; second, even if the assumption holds, there will be a further error introduced in equation (4.6) by the use of the difference form (this error will be of the order of the square of the mesh size: cf. equation (4.1)).

These approximate results should be compared to those obtained from least-squares calculations; the various numbers have been collected in Table 4-1:

TABLE 4-1

Values of the Lorentzian coefficient, C_L, compared with the values of the experimental coefficient, C_E. All values have units of cm^{-2}.

	C_L (least squares fitting)	C_E (approximated results)
Line-spread	9.73×10^3	7.14×10^3
Edge-Spread	2.22×10^4	1.11×10^4

As mentioned, these values of the coefficient differ from previously used values, by as much as an order of magnitude; if one discounts numerical errors, then this difference could be attributed to the presence of γ-radiation in the beam, or to the sample having a significant scattering component in its total cross-section. In other words, one could artificially use the Lorentzian coefficient as an indicator of sample properties, as well as convertor foil properties. However, care must be used in this approach, because one will not have any reliable means of telling how good or bad the approximation is, or even whether the model has completely broken down. Even if one foregoes the strict application of the various Lorentzian functions, and uses only the approximate forms given by equations (4.3) and (4.6), the results may still be dubious, because these approximations are Lorentzian-based. From an examination of figures 4-2 and 4-3, it is rather uncertain as to which coefficient, i.e. C_L or C_E, gives a better fit to the data; this in turn brings up the matter of whether or not numerical methods are of any applicability. To discuss this problem, one must realize that the simple matters of line-spread functions are of relatively little importance in a practical situation; one is more interested in the edge-spread function obtained from a radiograph of a given object. Furthermore, if the composition of that object is unknown, it is not unlikely that one would desire a simple means of determining this composition. This could conceivably be done by calculating $\phi(u)$, the attenuation function; as shown by equation (2.1), ϕ is a function of cross-section and object thickness, and with this knowledge one could obtain at least a first estimate of the object make-up. It is here that a simple numerical technique could be invaluable.

Consider the general, non-specific convertor response given by equations (2.3) and (2.4b):

$$S_A(x) = N \int_{-\infty}^{\infty} R(x,u)\phi(u)du \tag{4.7a}$$

$$= N\left\{\int_{\infty}^{x_n} R(x,u)du + \int_{x_n}^{x_p} R(x,u)\phi(u)du + \int_{x_p}^{\infty} R(x,u)du\right\} \tag{4.7b}$$

The equation is "non-specific" in that no particular form is given for R(x,u); in fact, there is no reason why an experimental line-spread curve could not be used. In doing this, one would need to put equations(4.7) into a discrete form; this is necessary because one will have a set of experimental data points. To accomplish this, the integrals in equation (4.7b) are replaced by summations, and the following quantities are defined:

$$\begin{aligned} &u_j = j\Delta u = jh;\ x_i = i\Delta x \\ &x_n = m_n\Delta x = m_n h;\ x_p = m_p h \\ &-\infty \rightarrow M_n h;\ +\infty \rightarrow M_p h \end{aligned} \tag{4.8}$$

One should note a convenient property of infinity in discrete situations: infinity is as many mesh points (i.e. M_n or M_p) away from the object edges as is necessary for edge-effects to become negligible. Note that a constant mesh size is assumed. If equations (4.8) are substituted into equations(4.7), one obtains

$$S_i = H\left\{\sum_{j=M_n}^{m_n} R_{ij} + \sum_{j=m_n}^{m_p} R_{ij}\phi_j + \sum_{j=m_p}^{M_p} R_{ij}\right\} \tag{4.9}$$

where

$S_i \equiv S_A(x_i)$

$H \equiv hN$

$R_{ij} \equiv$ the value, at $u = j\Delta u$, of an experimentally obtained LSC centred at $x = i\Delta x$ (determined from equation (4.1)).

For convenience, let

$$P_i^{(n)} \equiv \sum_{j=M_n}^{m_n} R_{ij}; \qquad P_i^{(p)} \equiv \sum_{j=m_p}^{M_p} R_{ij}$$

Equation (4.9) then becomes

$$S_i = H\left\{P_i^{(n)} + P_i^{(p)} + \sum_{j=m_n}^{m_p} R_{ij}\phi_j\right\} \tag{4.10}$$

Clearly then, if there are $i = 1, \ldots, I$ data points, one has

$$\begin{bmatrix} S_1 \\ \vdots \\ S_I \end{bmatrix} = H \begin{bmatrix} P_1^{(n)} + P_1^{(p)} \\ \vdots \\ P_I^{(n)} + P_I^{(p)} \end{bmatrix} + H \begin{bmatrix} R_{1m_n} & \cdots & R_{1m_p} \\ \vdots & & \vdots \\ R_{Im_n} & \cdots & R_{Im_p} \end{bmatrix} \begin{bmatrix} \phi_{m_n} \\ \vdots \\ \phi_{m_p} \end{bmatrix} \tag{4.11}$$

which becomes

$$\underline{S} = H\left[\underline{\ }^{(n)} + \underline{P}^{(p)} + \underline{\underline{R}}\ \underline{\phi}\right] \tag{4.12}$$

Thus, the solution for $\underline{\phi}$ is

$$\underline{\phi} = \underline{\underline{R}}^{-1}[\frac{1}{H}\,\underline{S} - \underline{P}^{(n)} - \underline{P}^{(p)}] \tag{4.13}$$

Here, it is assumed that $\underline{\underline{R}}^{-1}$ exists; additionally, since $\underline{\underline{R}}$ is not a square matrix, one is dealing with the so-called psuedo-inverse of $\underline{\underline{R}}$[6]. This results in some extra computational effort, but this is of no major concern since computer programs exist to deal with this sort of problem. The point to be made is that equation (4.13) provides a fairly straightforward method of estimating an object's composition from a radiographic image: having obtained ϕ_k, the value of the attenuation function at $x_k = k\Delta x$, one obtains the thickness and cross-section from

$$(\Sigma z)_k = -\ell n[\phi_k] \tag{4.14}$$

One should note that this method is not entirely free of problems; first, one will only obtain an estimate of either Σ or z from equation (4.14): two variables cannot be independently specified by one equation. Second, any values obtained will be average values; in mathematical terms, this average will be given by

$$\Sigma_i = \frac{1}{T_i} \int_0^{T_i} \Sigma_a(z)dz \tag{4.15}$$

T_i being the thickness of the object at $x = i\Delta x$. This may lead to some confusion if the object is made up of a number of different materials; however, with caution useful information can still be obtained. Third, equation (4.13) gives no indication of the sensitivity of this method; various numerical errors could mask the desired information, although with some effort an error analysis could be done. Finally, equation (4.9) assumes that the values of the response corresponding to the objects edges are known, and are given by equation (4.8). This may not be the case; as previously indicated, one of the primary assumptions of ESF theory is that the locations of the edges are not exactly determined. What may be required here is some sort of interative procedure, whereby initial guesses for either $\underline{\phi}$ or for m_n and m_p are supplied, and repeated calculations with equations (4.9) through (4.13) are used to improve these guesses. However this method is used, caution is once again suggested.

This concludes this section; to continue any further would take the work beyond the basic survey which it was meant to be. This is not to say that the numerical methods are not worthy of further investigation; in fact, it is thought that continued research, particularly with regard to the "gremlins", will prove to be quite fruitful in developing a good calculational tool.

4.2 Monte Carlo Methods*

In the previous section, methods were outlined whereby one could cary out an image analysis procedure without the use of any complicated techniques: this is the so-called "equation-free" approach. In moving to a higher level of examination, one might choose a model which, though it uses some mathematics, still maintains a more basic outlook with regard to the physical problem. This idea combines the virtues of the two methods: one obtains the computational simplicity

*This work has previously appeared, in somewhat different form, as a term paper submitted in partial fulfillment of the course requirements for Engineering Physics 704.

of a strictly numerical approach, and at the same time has some sort of mathematical structure whereby predictions and estimates can be made. A very general class of techniques which fits these requirements is Monte Carlo analysis, which combines statistics with basic and well-defined physical models; as will become apparent, the Monte Carlo methods lead to results which are in good agreement with those obtained by Lorentzian analysis, and in addition allow an investigation to be taken far beyond that point which might be easily attained with an ESF approach. In particular, Monte Carlo techniques allow scattering effects to be built into one's model, and more importantly they allow a two-dimensional analysis to be undertaken, which in itself is not a trivial problem.

As in the previous section, this work is intended to be a preliminary survey; thus, no particularly complicated analyses were undertaken, especially since the results suggested that an excess of sophistication was unnecessary. The only drawback to this approach is that no proper error analysis was done; rather, the errors were estimated from

$$\{\text{Error}\} \propto 1/\sqrt{N} \tag{4.16}$$

N being the number of histories involved in the simulation. If this work is to be continued, it is strongly suggested that formal error studies be incorporated into the examination.

In passing it should be noted that the basic principles involved in a Monte Carlo study were obtained from references 7, 8, and 9. Also, the calculational algorithms used in this section are collected for easy reference in the appendix, along with the estimated errors given by equation (4.16).

As an obvious starting point, consider the very basic problem of analyzing the spreading of the secondary radiation about the point of neutron capture in the convertor foil. As shown by figure 4-4, one needs some information concerning the film-convertor separation (d), the distance of neutron penetration into the convertor (p), and the point where the secondary radiation strikes the film (x_p). If the neutron penetration is to be considered, then one needs to model the convertor attenuation of both neutrons and secondary radiation; thus for simplicity it is assumed that the neutrons are captured instantaneously. As a result, the problem reduces to that of determining the emission angle, θ; once this is done, it is easy to see that the secondary impact point is given by

$$x_p = d*\tan\theta \qquad (4.17)$$

Now, since isotropic scatter is assumed, the angle can be determined from

$$\theta = \frac{\pi}{2}(1 - 2\xi) \qquad (4.18)$$

where ξ is the random variable. The form given by equation (4.18) is a biased result, in that it only allows for back-scatter into the film; however, this is justified by noting that any secondary radiation which is forward-scattered is "lost", unless it is again deflected toward

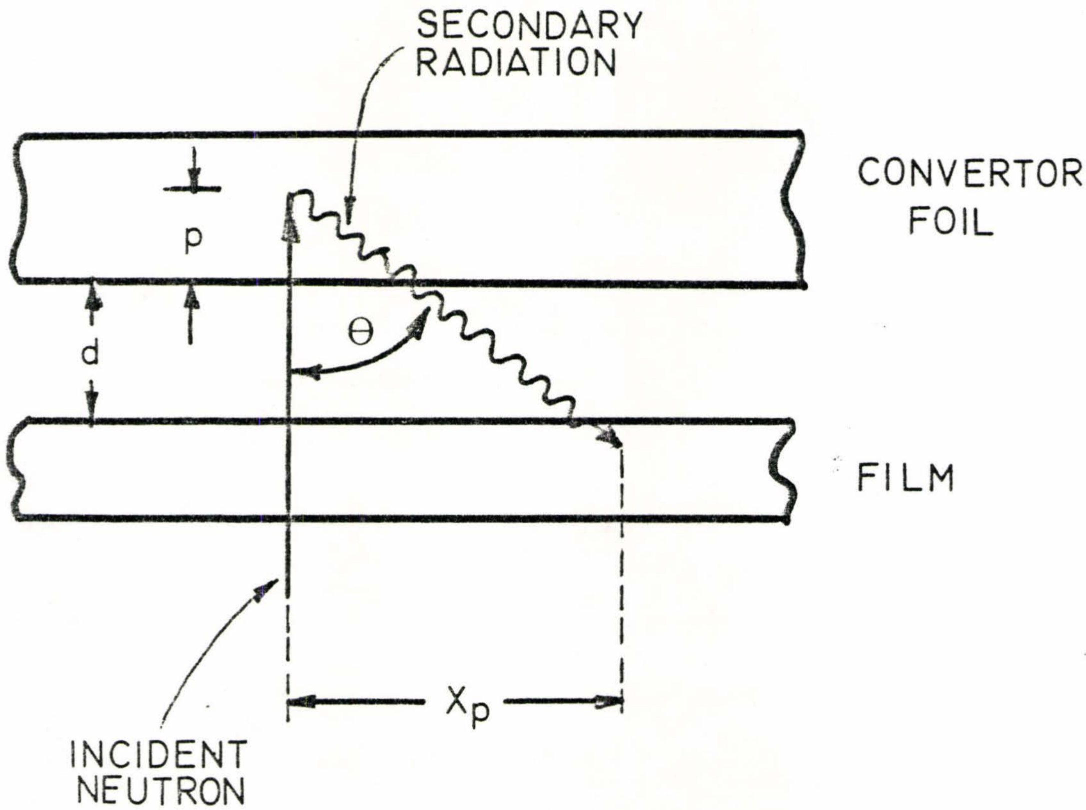

Fig. 4-4: The geometry used in a Monte Carlo LSF analysis.

the film.

As might be expected, this approach resulted in a curve which, as shown by least-squares methods, was very well-fitted by a Lorentzian. However, instead of just using this method to generate LSF curves, equations (4.17) and (4.18) were used to calculate C_L as a function of the film-convertor separation, and this in turn was compared to the results obtained from a "pure" theoretical analysis;[1] this is shown in figure 4-5. The agreement between the two sets of data is generally very good, except for small d, where there is as much as twenty percent difference. It is thought that this difference is due to the theoretical model including film attenuation and convertor thickness effects; if this is the case, then the agreement appears to be even better.

The next area to consider in this investigation is that of "finite" geometries, which basically means one now has to consider material and geometric properties of the sample in conjunction with the system properties, such as convertor effects. Obviously, the simplest case to consider is that of the semi-infinite slab, with constant thickness (z) and cross-section (Σ). This geometry has the advantage of being very easy to study, both in terms of computational effort and in terms of characterization: if one considers the "attenuation product" (Σz), then one has a very neat means of examining thickness and cross-section properties (and their effects on the ESF analysis) in considerable generality.

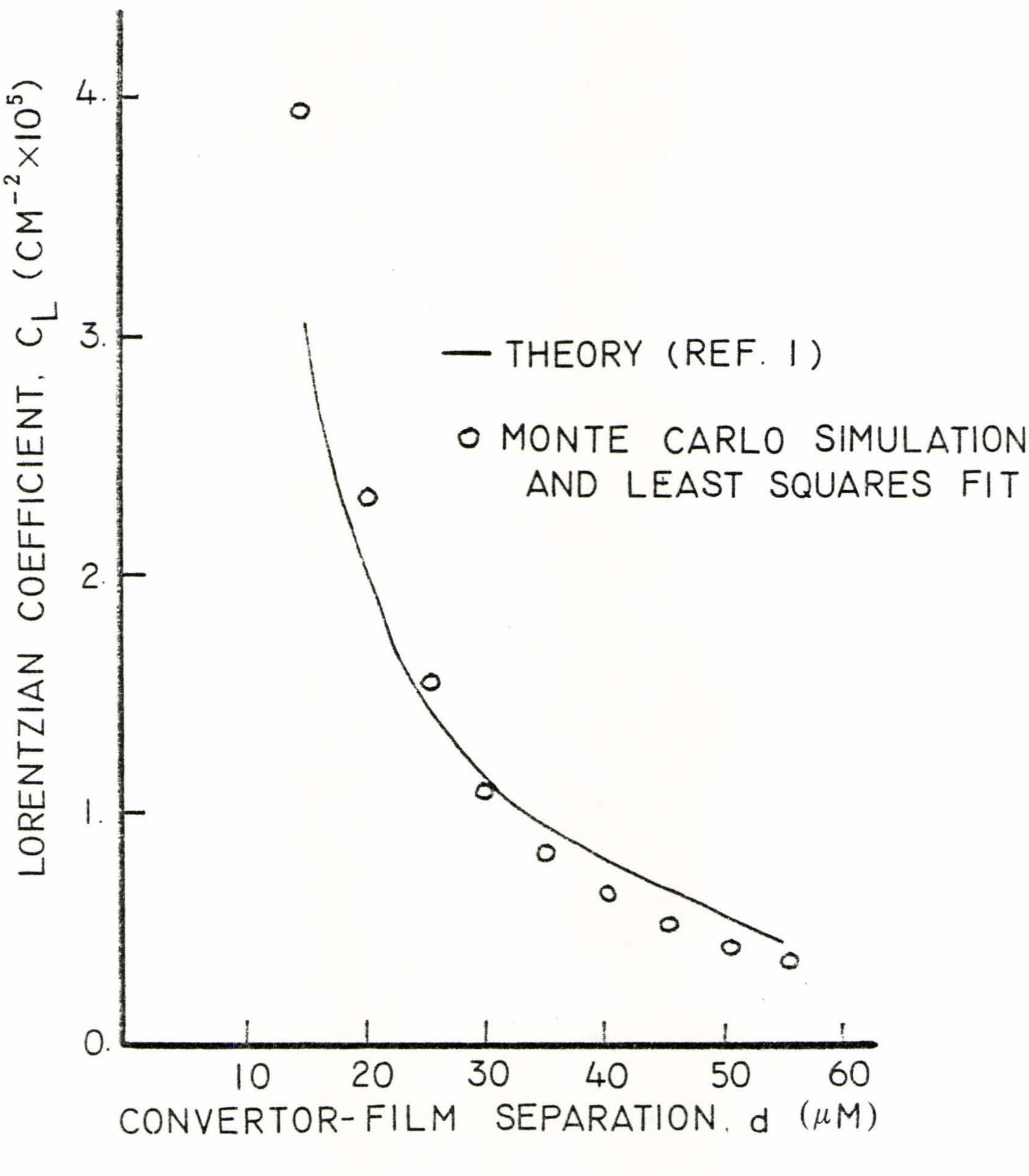

Fig. 4-5: The Lorentzian coefficient as a function of film-convertor separation.

For this case, the Monte Carlo model is very much the same as that used in the LSF study, in that isotropic emission and no neutron penetration occur in the convertor. In this case, however, one has more than one convertor emission point to consider, and in addition there will be some attenuation of the incident neutron beam over part of the region under consideration. Fortunately, the only effect of this is to slightly complicate the "bookkeeping" portion of the computer program used.

A sample result is shown in figure 4-6, and again the agreement with the Lorentzian model is very good. The drop at the low end of the curve is from using a finite number of mesh points, and could easily be eliminated by using some sort of weighting scheme. For reference, the theoretical curve was generated by using a least-squares estimate for C_L in the Lorentzian expression for a semi-infinite, partially-absorbing slab:

$$S_A(x) = 1. + \frac{1}{\pi}(e^{-\Sigma z} - 1)[\frac{\pi}{2} - \tan^{-1}(\sqrt{C_L}\, x)] \quad (4.19)$$

Other than there being a satisfyingly good agreement between the two types of curves, figure 4-6 is of relatively little consequence. A matter of greater interest is illustrated in figure 4-7, which shows C_L as a function of both the attenuation product and the film-convertor separation. It is apparent that C_L is either independent of or only weakly dependent on material thickness and cross-section; this is not entirely surprising, since the findings of the earlier portions of this

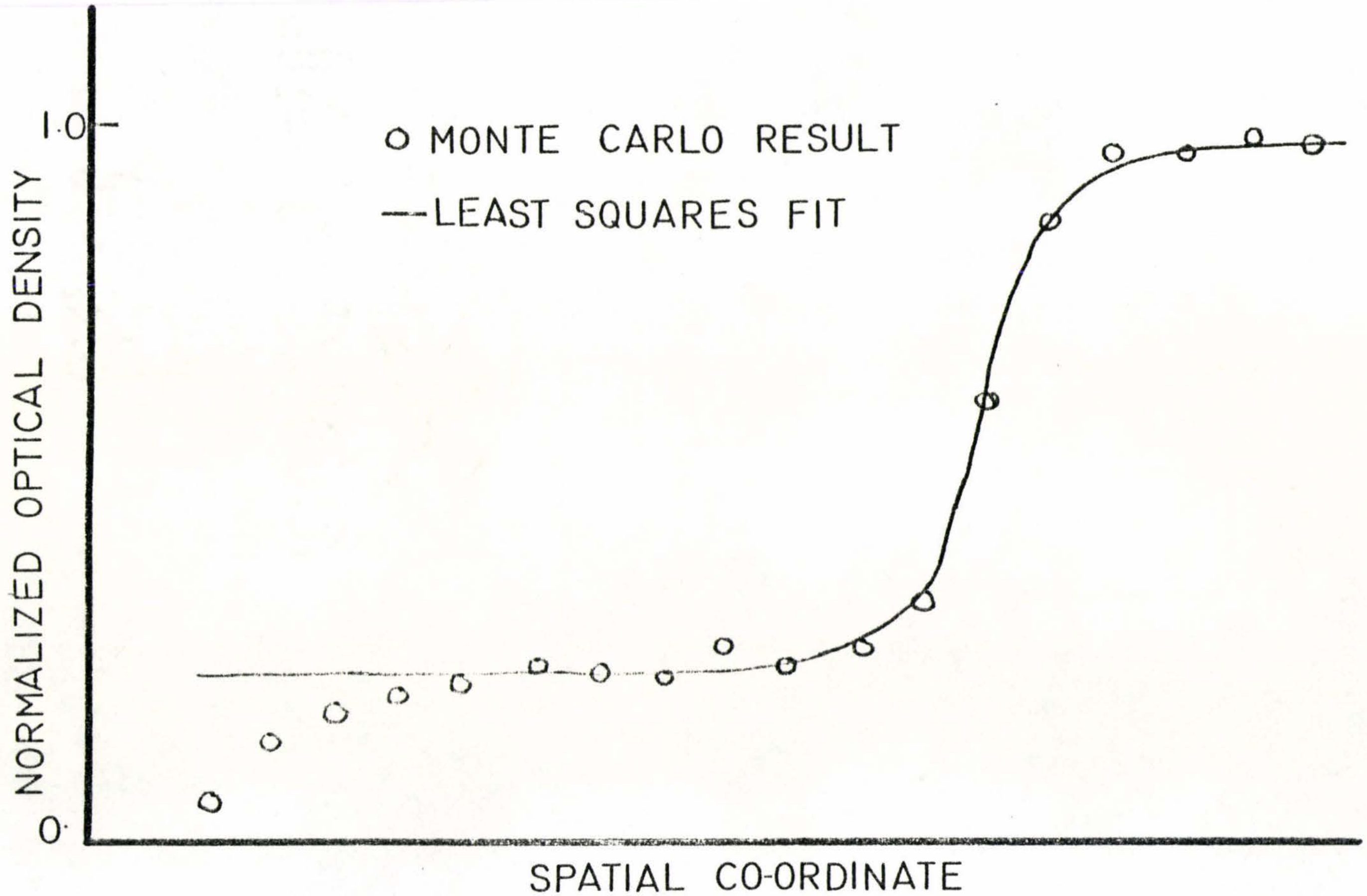

Fig. 4-6: Monte Carlo and Lorentzian ESF curves for a semi-infinite partially absorbing slab. The "dip" at the left of the curve is a statistical phantom.

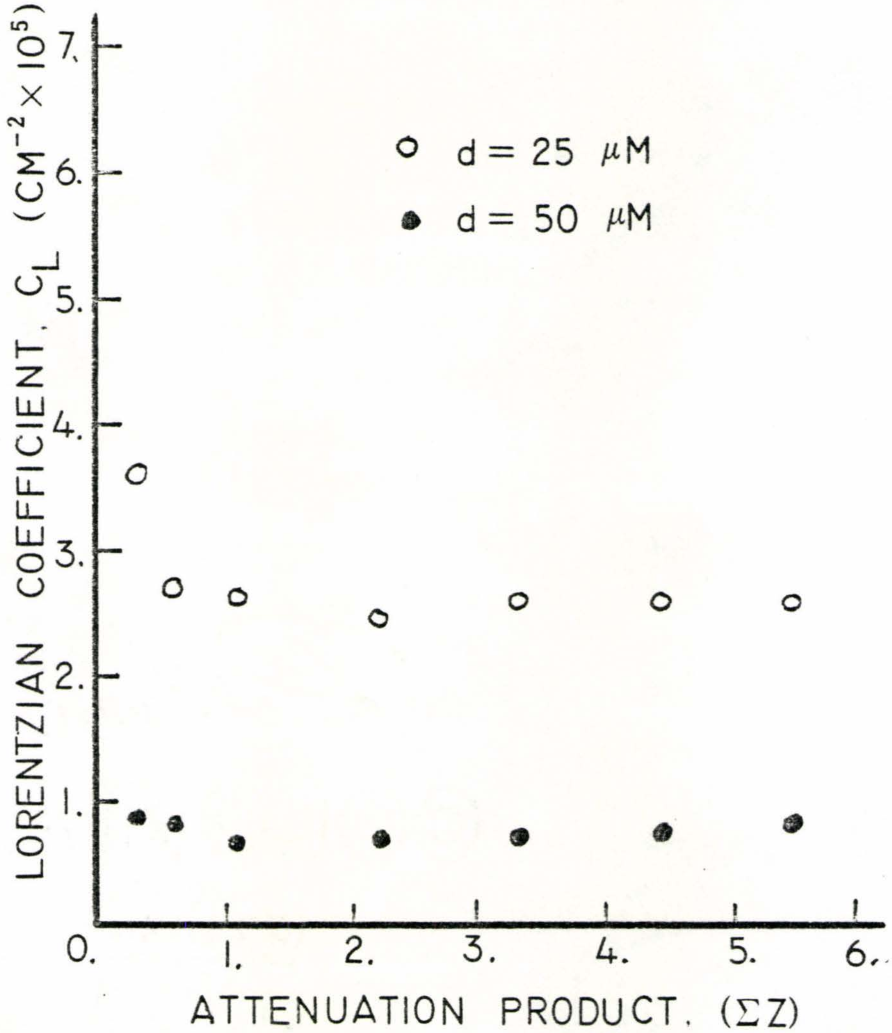

Fig. 4-7: The Lorentzian coefficient as a function of the attenuation product (Σz). The results imply that C_L is independent of the make-up at the object being radiographed.

work have indicated that using C_L to characterize sample properties, in addition to convertor properties, is at best an artificial use of Lorentzian techniques. Whether or not this "artificial approach" will prove useful will be left as a matter for future investigation.

It is of some interest to note that while C_L appears to be independent of (Σz), but still depends on the value of the film-convertor separation (d), the numerical values obtained for C_L with an ESF analysis are different for those obtained with an LSF analysis. A similar result occurred in section 4.1, when simple numerical techniques were used; at that point, the discrepancy was attributed to either a γ-component in the beam, or to scattering properties of the sample being radiographed. In this analysis, however, neither of these phenomena is possible, simply because the Monte Carlo model does not allow for such events. Thus, one is forced to conclude that the difference between the coefficients obtained for an LSF and for an ESF is due to some sort of numerical peculiarity. This in turn suggests that any "artificial" use of Lorentzian theory should be undertaken with the utmost caution, which means that perhaps Lorentzian models should be restricted to those situations which closely resemble the ideal case of absorption-only samples. Another point to be made here is that this conclusion appears to throw a shadow on the use of any equation-free techniques; instead, it is suggested that this result indicates one should refrain from applying any sort of approximate calculations (i.e. those associated with the experimental coefficient C_E), and should instead follow a "pure" numerical approach, as given by equations (4.9) through (4.13). In short, one arrives at the general conclusion that the Lorentzian model - or any other model - should not be pushed beyond whatever limits arise from its basic assumptions.

Carrying on with the investigation, the next logical step seems to be to examine the effect of sample scattering of the incident neutron beam. For the Monte Carlo model, one requires some information about the penetration distance (ℓ), the type of interaction (Σ_a or Σ_s), the angle of scatter (θ), and the point of impact in the convertor (x_s); these quantities are illustrated in figure 4-8. For simplicity, this examination makes use of a so-called "one-shot" model; all this means is that for each incident neutron, only one interaction is allowed: either absorption occurs, upon which the history is terminated, or scattering occurs, at which point free-flight to the convertor is "forced". Note that only the neutron flux (after passing through the sample) was calculated; the principles of evaluating the convertor response have already been illustrated.

A sample result is shown in figure 4-9, and it clearly indicates a previously unencountered edge effect. Whether or not this will prove to be a significant effect remains to be seen; for instance, the small "blips" on either side of the point on the curve corresponding to the edge may just be statistical phantoms, arising from the somewhat unrealistic one-shot model. Contrarily, if one views the curve in terms of what might be called balanced scatter, the results begin to make sense: there is a net neutron current <u>out</u> of the sample

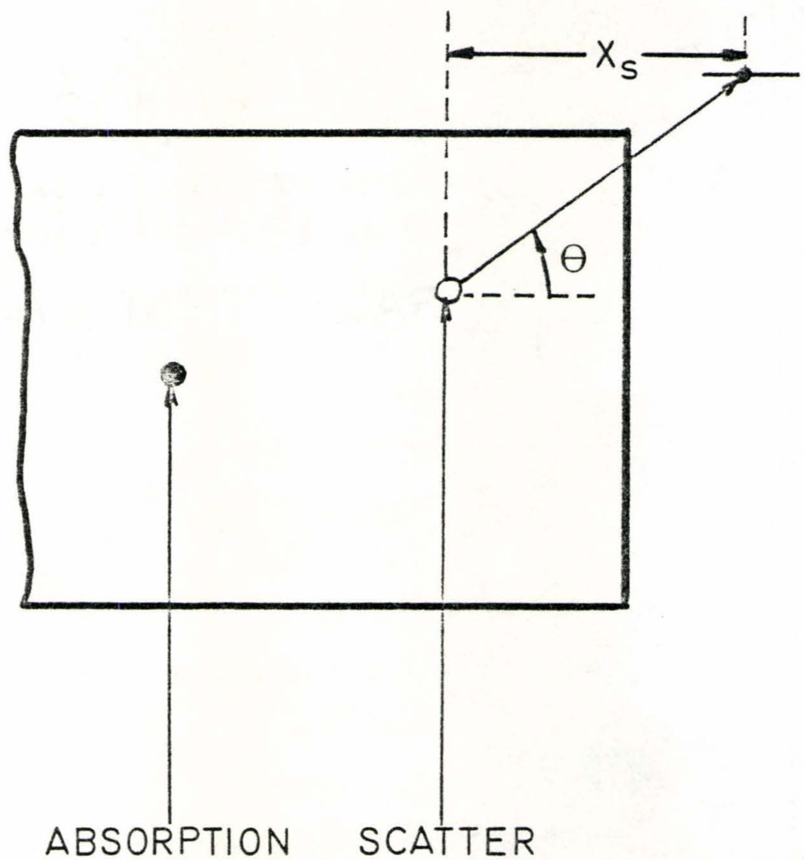

Fig. 4-8: The geometry for a Monte Carlo ESF analysis, including sample scattering effects and using a "one-shot" model.

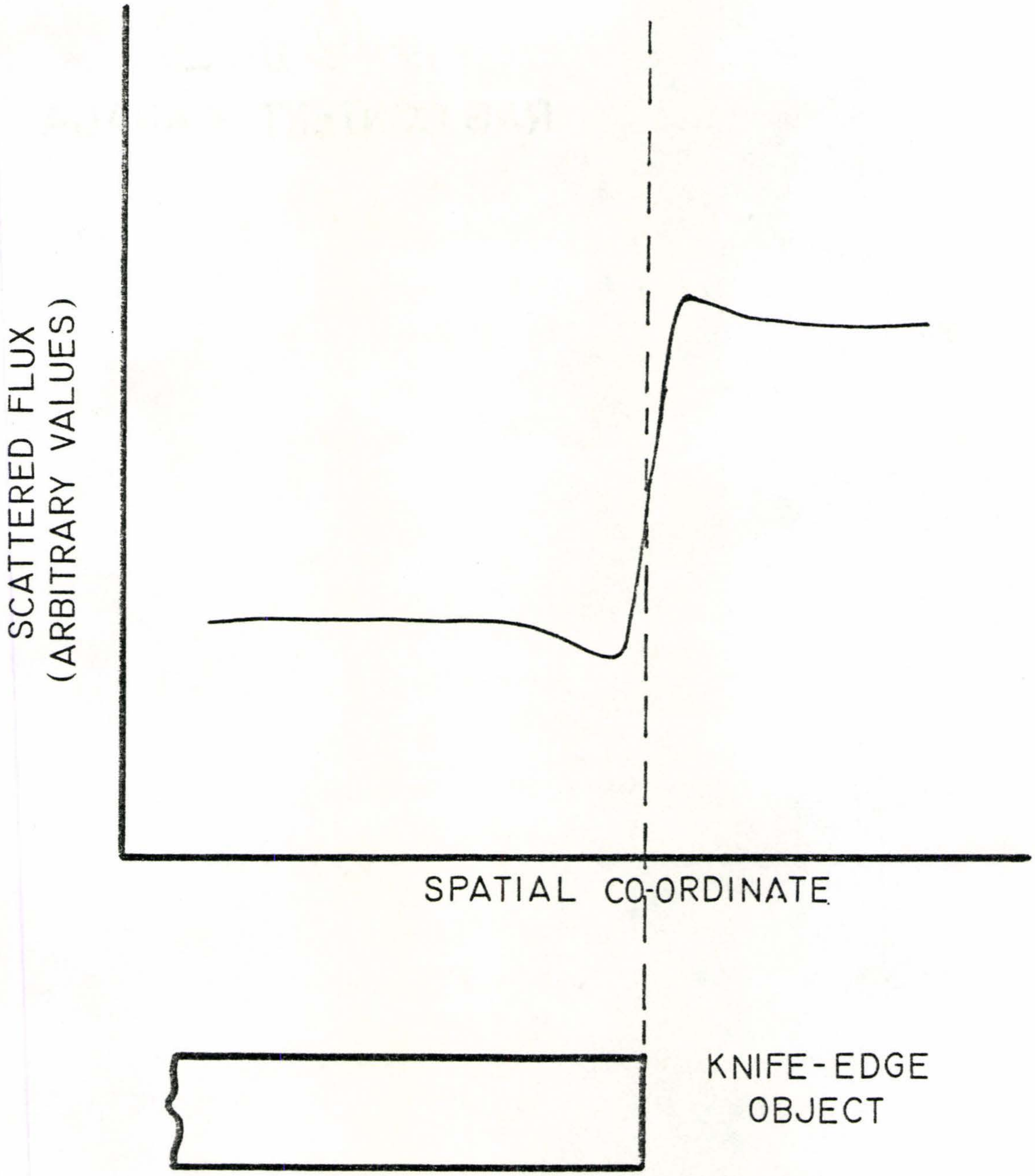

Fig. 4-9: Neutron flux after a homogeneous incident beam passes through a sample with a finite scatter cross-section.

face at the edge because of scattering, but there is no corresponding current into the sample face. As a result, there should be an "excess" or a "scarcity" of neutrons at the points indicated by the "blips". Another point to note is that these deviations,which are apparently caused by scattering,may disappear because of the smoothing effect of the convertor response; the blips are quite small to begin with, and thus after convolution with an LSF (which is the process occurring in the convertor foil, from a mathematical viewpoint), the whole curve is "smeared" so that one might not be able to detect this effect. The point to be made here is that scattering effects cannot be easily disregarded; however, it is possible to examine these effects without need of any complex models. For an example of just how difficult the analysis can become, see reference 10.

At this point, the problem of radiographic analysis in two dimensions will be the next major area to be considered. The majority of previous work, both analytical and experimental, has dealt with one dimensional problems where the isotropic emission of secondary radiation has been restricted to a plane perpendicular to the convertor foil, containing a "row" of emitters, or a line source. In a more general analysis, one might wish to consider the effects of secondary radiation emission which is unrestricted, in the sense that one now has two angles specifying the direction of emission. For isotropic emission, the probability of any directional pair (θ_1,ϕ_1) will be equal to that of any other pair (θ_2,ϕ_2).

Before the Monte Carlo model is introduced, it may be of some interest to examine an analytical model. Basically, all one has to do is extend the edge-spread model to two-dimensions; thus, the probability of secondary radiation emitted in the converter at a point (u,v) and striking the film at a point (x,y) is given by the *point*-spread function (PSF)

$$R(x,y,u,v) \equiv R(\vec{r},\vec{r}\,') \tag{4.20}$$

If a Lorentzian model is used, the PSF becomes

$$L(\vec{r},\vec{r}\,') = \frac{1}{1 + C_L|\vec{r} - \vec{r}\,'|^2} \tag{4.21a}$$

$$= \frac{1}{1 + C_L[(x-u)^2 + (y-v)^2]} \tag{4.21b}$$

where the latter form is for Cartesian co-ordinates. The symbolism used here is illustrated in figure 4-10.

In setting up the expression for the convertor response, one needs an attenuation function. In analogy with the one-dimensional form the equation to be used will be

$$\phi(\vec{r}\,') = \exp\{-\int_{z_n(\vec{r}\,')}^{z_p(\vec{r}\,')} \Sigma_a(\vec{r}\,',z)dz\} \tag{4.22}$$

Here, z_p and z_n represent the limits of the material path which the neutron traverses at $\vec{r}\,'$, and $\Sigma_a(\vec{r}\,',z)$ is the value of the macroscopic absorption cross-section at the point $(\vec{r}\,',z)$. Combining equations (4.20) and (4.22), the incremental convertor response becomes

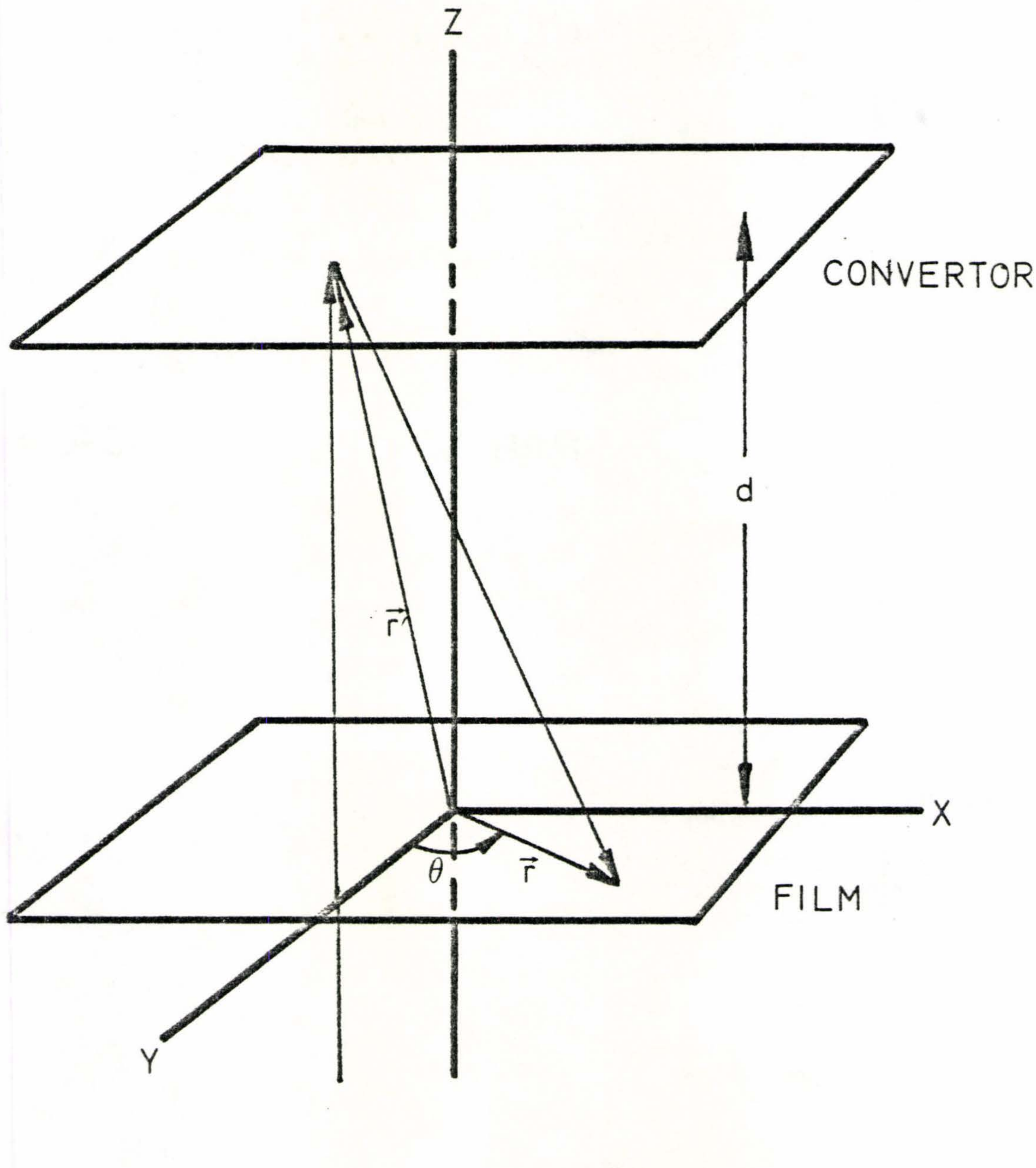

Fig. 4-10: The geometry used for two-dimensional point-spread function analysis.

$$dS_A(\vec{r},\vec{r}') \;\alpha\; \phi(\vec{r}')R(\vec{r},\vec{r}')d\vec{r}'$$

In words, the fraction of convertor response at $\vec{r}$, due to emission at $\vec{r}'$, is given by the attenuation of the incident neutron beam at $\vec{r}'$ (ϕ), multiplied by the probability of the radiation emitted at $\vec{r}'$ striking the film in a region $d\vec{r}'$ about a point $\vec{r}$. Clearly, when emission from the whole plane is considered, the convertor response is given by

$$S_A(\vec{r}) = N \int_{-\infty}^{\infty}\!\!\int R(\vec{r},\vec{r}')\phi(\vec{r}')d\vec{r}' \tag{4.23}$$

The limits of integration are meant to imply integration over both variables. N is the normalization constant, similar to that used previously.

The solution of equation (4.23) is a non-trivial but straightforward matter, as was the case in one-dimension. In this situation however, the method of breaking up the infinite region of integration is not so easily applied, since the edges of the object may not necessarily be specified by constant values of the particular co-ordinate. Instead, if the object boundary is denoted by $B(\vec{r}')$, then equation (4.23) can be written as

$$\frac{S_A(\vec{r})}{N} = \iint\limits_{\vec{r}'\notin b(\vec{r}')} R(\vec{r},\vec{r}')d\vec{r}' + \iint\limits_{B(\vec{r}')} R(\vec{r},\vec{r}')\phi(\vec{r}')d\vec{r}' \tag{4.24}$$

The first integral is over the region "outside" of the object, where there is no beam attenuation (i.e. $\phi(\vec{r}') \to 1$), and is analogous to the terms in a one-dimensional case which represent the semi-infinite slabs at the object edges. The second integral is the perturbation term, indicative of material and geometric properties of the object.

So far, the problem is very much like the one-dimensional case, with the only difference being the increased complexity of the calculation. To illustrate this, consider the object shown in figure 4-11: the geometry is that of an infinitely absorbing material covering three-quarters of the plane. The reason for using this shape will become apparent in the Monte Carlo analysis. If x-y geometry is used, then it is easy to see that the attenuation function is given by

$$\phi(u,v) = \begin{cases} 1, & u,\ v \leq 0 \\ 0, & \text{otherwise} \end{cases} \tag{4.25}$$

Using this, equation (4.23) becomes

$$\frac{S_A(x,y)}{N} = \int_{v=-\infty}^{0} \int_{u=-\infty}^{0} R(x,y,u,v)\,du\,dv \tag{4.26}$$

Examination of the inner integral shows that the function is equivalent to that given by equation (2.4c):

$$\int_{u=a}^{b} R(x,y,u,v)\,du \equiv r_1(x,y;a,v) - r_1(x,y;b,v) \tag{4.27}$$

Here, the fact that two variables are involved is indicated by denoting the integrated function by r_1. Equation (4.26) now becomes

$$\frac{S_A(x,y)}{N} = \int_{v=-\infty}^{0} \{r_1(x,y;o,v) - r_1(x,y;-\infty,v)\}dv \tag{4.28}$$

Note that the integrand in equation (4.28) is similar to the generalized ESF for a semi-infinite knife-edge, as developed in section 2.1. If one defines

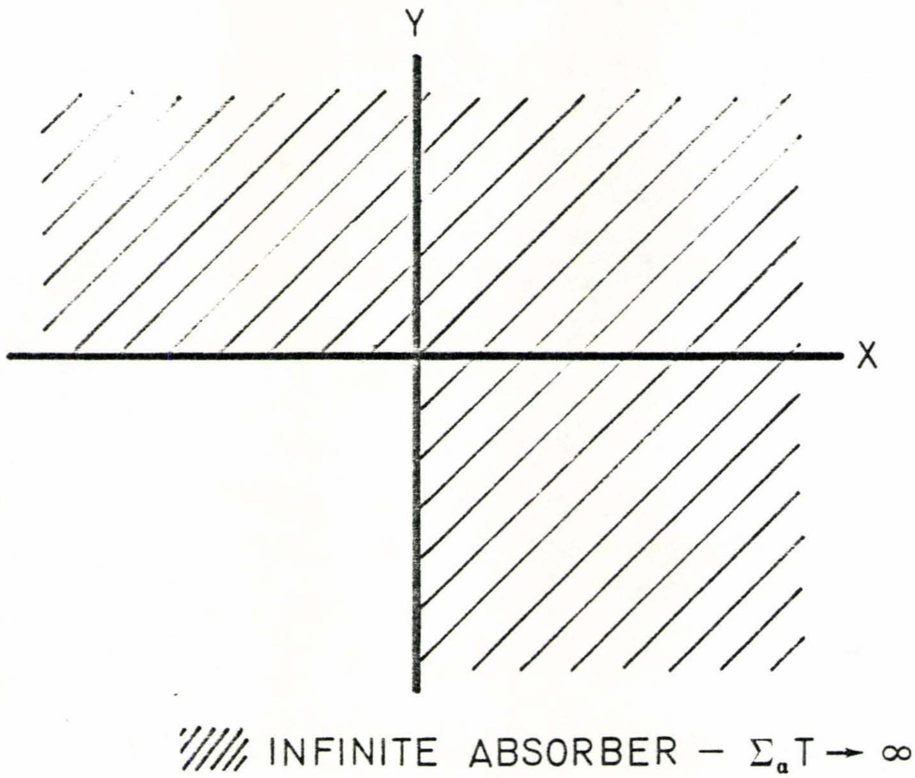

Fig. 4-11: The geometry used for a simple analytical study in two-dimensions.

$$\int_a^b r_1(x,y;\alpha,v)dv = r_2(x,y;\alpha,b) - r_2(x,y;\alpha,a) \tag{4.29}$$

then equation (4.28) in turn becomes

$$\frac{S_A(x,y)}{N} = r_2(x,y;0,0) - r_2(x,y;0,-\infty) - r_2(x,y;-\infty,0)$$

$$+ r_2(x,y;-\infty,-\infty) \tag{4.30}$$

Consider these four terms separately: in light of the one-dimensional results, any term which has $\pm\infty$ in it should be constant. Hence, the fourth term in equation (4.30) indicates that at a great distance from any object features, the convertor response is unaffected by those features. This is to be expected, since the convertor response is affected by the attenuation function; if this function is constant, then the convertor response variation is determined only by the point-spread function.

The second and third terms in equation (4.30) would appear to be similar to the fourth term in appearance and effect, were it not for the fact that two variables are involved here. What the terms actually represent is the fact that at a point near an object feature in terms of one co-ordinate, but far from any features in terms of the other co-ordinate, the response is only dependent on one variable. This is illustrated in figure 4-12: at a point some distance from the corner, the net current of secondary radiation in the y-direction is zero, since the emission is isotropic and the neutron beam attenuation is constant with respect to y. Thus, the convertor response at this point is dependent only on x, as given by the second term in equation

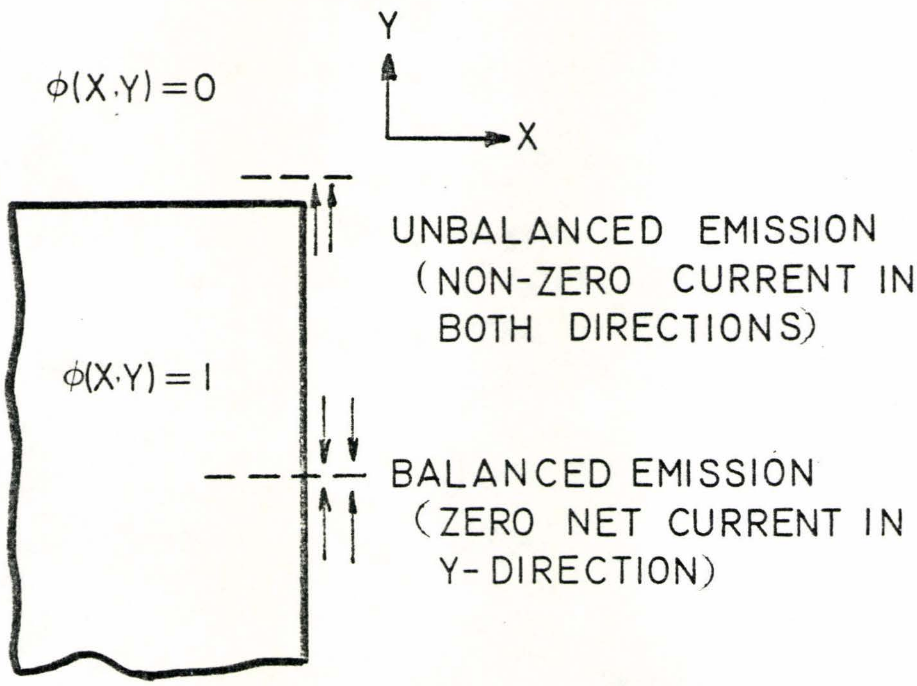

Fig. 4-12: The concepts of balanced and unbalanced emission in two dimensions.

(4.30). A similar result holds for the variation of S_A independently of x, as given by the third term.

The remaining term in the equation represents the variation of the convertor response at points near an object feature in terms of both variables. Consider figure 4-12 again: as an example, at the object corner, the secondary flux in the y-direction is shown. Note that there is a non-zero current here, because there is no secondary emission for x or y positive ($\phi(x,y)=0$). Similarly, there would be a net current in the x-direction. As a result, the expression for the response must include an explicit dependence on both x and y, for points near an object feature. Note that the ideas discussed in the preceeding paragraphs are similar to the concept of balanced scatter introduced earlier; here of course, one refers to balanced emission, rather than scatter.

Before moving on to the Monte Carlo analysis, one last matter of interest with respect to the analytical study will be considered. In a rigourous examination, one would have to work directly with equation (4.26), at least for this geometry. However, it will be useful to have some sort of empirical model which can be used for quick rough calculations. Thus, considering equation (4.30) in terms of a Lorentzian form, and recalling the previous discussion, the following approximation is suggested:

$$S^*(x,y) = a_1 \tan^{-1} [b_1 \sqrt{x^2+y^2}] + a_2 \tan^{-1} [b_2 x] + a_3 \tan^{-1} [b_3 y] + a_4 \qquad (4.31)$$

The form of this equation is suggested partly by equation (4.30) and partly by the one-dimensional results of Section 2, where it was shown that the convertor response expression for a knife edge is given by

$$S_A(x) = \frac{1}{\pi} \tan^{-1} [\sqrt{C}x] + \frac{1}{2}$$

Thus the second and third terms in equation (4.31) correspond to the response at a large distance from the corner, in terms of one or the other of the co-ordinates. Note that in equation (4.31) some leeway has been left for approximation by incorporating the unknown parameters a_i and b_i. One can estimate the coefficients a_i by considering the value of S* at large distances from the convertor. For example, at $(x,y) = (-\infty,-\infty)$, there is no beam attenuation, hence there should be a full convertor response, i.e. $S^*(-\infty,-\infty) = 1.0$. At the points $(0,-\infty)$ and $(-\infty,0)$, $S^* = 0.5$; this is because at these points the problem is essentially one-dimensional, and as shown in section 2, the value of the convertor response at the edge of an infinite absorber is 0.5. Finally, at the point (0,0), S* is defined as S_{oo}. Substituting these results into equation (4.31), one obtains

$$\begin{bmatrix} \pi/2 & -\pi/2 & -\pi/2 & 1 \\ -\pi/2 & 0 & -\pi/2 & 1 \\ -\pi/2 & -\pi/2 & 0 & 1 \\ 0 & 0 & 0 & 1 \end{bmatrix} \begin{bmatrix} a_1 \\ a_2 \\ a_3 \\ a_4 \end{bmatrix} = \begin{bmatrix} 1 \\ 1/2 \\ 1/2 \\ S_{oo} \end{bmatrix} \qquad (4.32)$$

It is easy to show that this has the solution

$$\begin{bmatrix} a_1 \\ a_2 \\ a_3 \\ a_4 \end{bmatrix} = \frac{1}{\pi} \begin{bmatrix} 2(1 - S_{oo}) \\ -(3 - 4S_{oo}) \\ -(3 - 4S_{oo}) \\ S_{oo} \end{bmatrix} \qquad (4.33)$$

This result leads to the following empirical expression for the two-dimensional convertor response due to a "three-quarter" corner:

$$S^*(x,y) = \frac{1}{\pi} \{2(1-S_{oo}) \tan^{-1}[b_1\sqrt{x^2+y^2}] - (3-4S_{oo}) \tan^{-1}[b_2x] - (3-4S_{oo}) \tan^{-1}[b_3y] + S_{oo}\} \tag{4.34}$$

Whether or not this result will be of any use will require experimental or other verification, particularly with regard to the value of S_{oo}.

The Monte Carlo analysis for the two-dimensional case differs from the one-dimensional version only by having to specify the direction of secondary emission with two angles rather than one. Locating the point of impact in the film requires a two dimensional search, but this is not much more difficult than a one-dimensional search. The algorithm is once again very simple: one specifies the film-convertor separation (d) and the point of neutron capture (x,y). If this point is within the region defined as being "covered" by the infinite absorber, then one ends this particle history and starts over with a new particle. If the point (x,y) is in the "uncovered" region, then one calculates the direction of secondary emission from

$$\phi = \frac{\pi}{2}(1 - 2\xi_\phi)$$

$$\alpha = 2\pi\xi_\alpha$$

Then, the point of impact is calculated from

$$r = d*\tan(\frac{\pi}{2} - \phi)$$

$$x_f = x + r*\cos(\alpha)$$

$$x_f = y + r*\sin(\alpha)$$

Again, the model has been biased in favour of back-scatter by assuming forward-scattered radiation to be lost. After this, the problem again reduces to a matter of bookkeeping, i.e. keeping track of the number of particles landing at or about the point (x_f, y_f).

The geometry chosen for examination was the so-called three-quarter corner. The reason for this was to reduce the amount of computer time required to examine a significantly large number of particles; however, even when this was done, the amount of time involved required that a series of small runs be made and an average result obtained from these. A typical result is shown in figure 4-13. The figure illustrates clearly the calculation problems involved: at each mesh point, twelve thousand particle histories were considered, and yet the surface is still rather rough. With this in mind, the following discussion should be considered with caution, even though the results agree, to a certain extent, with earlier findings.

A preliminary examination of figure 4-13 gives some basic but useful results. First, the overall appearance of the CSF is about what was expected: there is a zero response in the region of attenuation, and there is a full response in the region of zero attenuation. Second, the edge-spread effect is visible: at those points near the object edge, the familiar

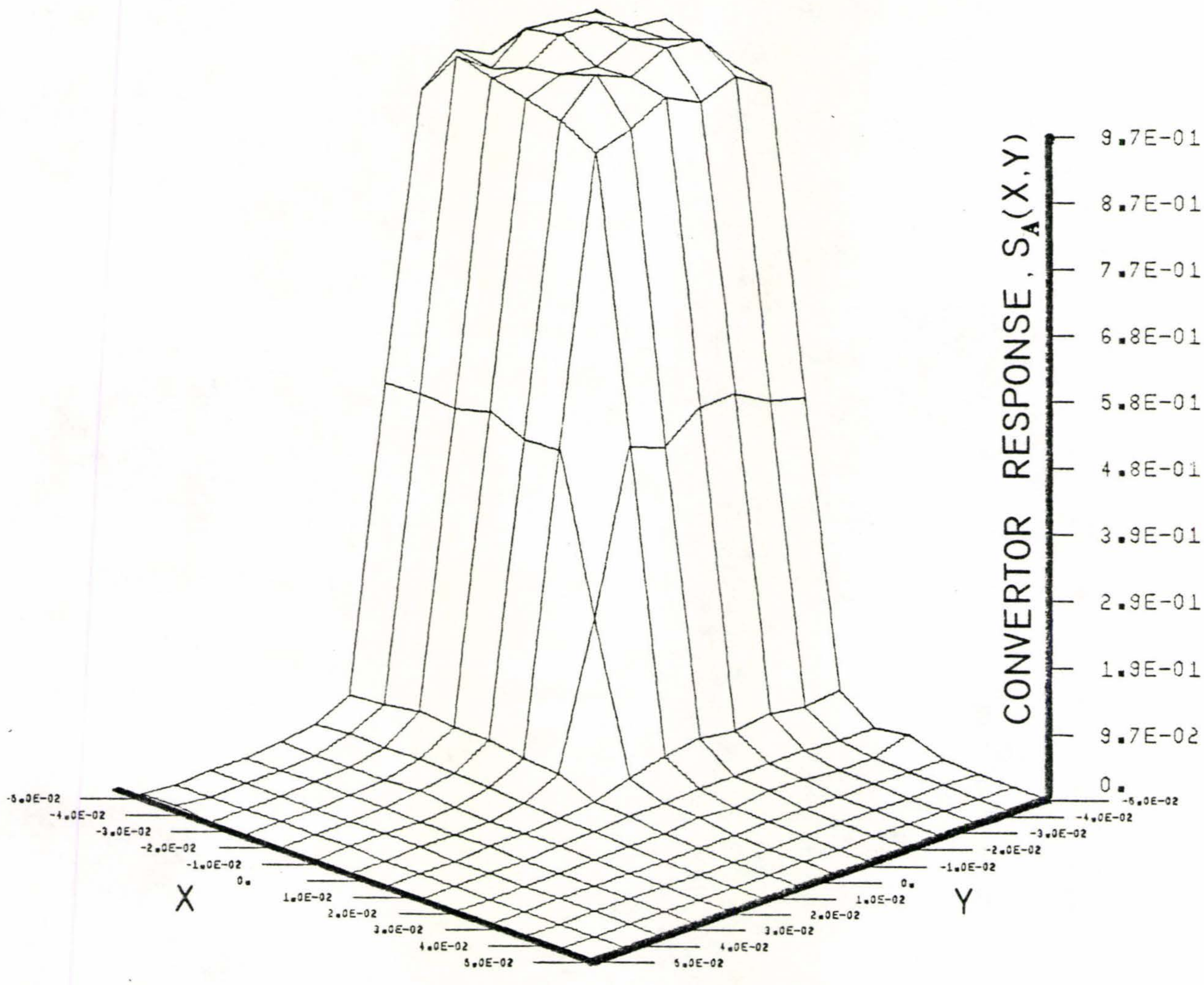

Fig. 4-13: A two-dimensional convertor response curve for a "three-quarter corner", obtained with Monte Carlo methods.

S-shape is present, even allowing for the crudity of the calculations. Finally, the convertor response near the corner is somewhat different in magnitude from that at points further away from the corner, in agreement with the previous study of analytical forms. This is best illustrated by the method shown in figure 4-14; the figure represents the two-dimensional convertor response as a function of x, for fixed values of y. The results clearly illustrate the point made previously, in that the values of $S_A(x,y)$ at "great" distances from the edge are relatively independent of y. Then, as one moves closer to the edge (i.e. y decreases), the value of the convertor response changes. Two points are of interest here: first, the shape of the response does not appear to change. Instead, the magnitude of the function varies with y. This suggests that a "working function" for approximate calculations of the response could be

$$\begin{aligned} S^*(x,y) &= s(y)\ t_2\ (x) \\ &\equiv s(y)\left[1/2 - \frac{1}{\pi}\tan^{-1}(bx)\right] \end{aligned} \tag{4.35}$$

where s(y) is some function such that

$$\begin{aligned} & s(-\infty) = 1 \\ & s(0) = s_0,\ 0 \leq s_0 \leq 1 \\ & s(\infty) = 0 \end{aligned} \tag{4.36}$$

This of course applies only for this particular geometry; it may not be possible to obtain such a simple representation for other situations.

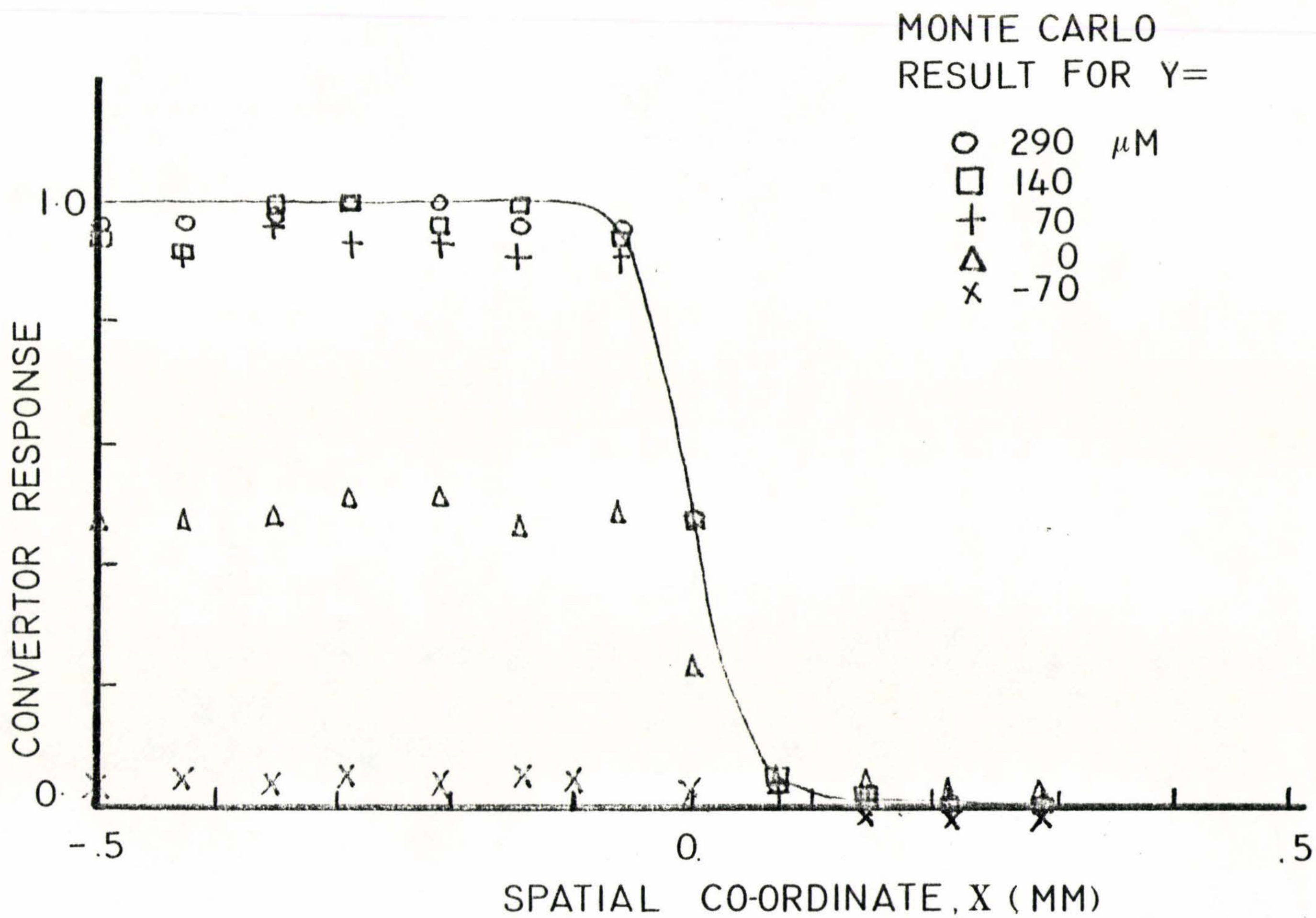

Fig. 4-14: Values of the convertor response for a "three-quarter corner". The results are a function of one co-ordinate with the other taking fixed values.

The second point to note is that the value of the response corresponding to the edge is, in a sense, independent of y; inspection of figure 4-14 suggests that

$$S_A(x_o,y) = \frac{1}{2}\{\max[S_A(x,y)] + \min[S_a(x,y)]\} \tag{4.37}$$

where the extrema are evaluated with respect to x, and x_o represents the edge. This result is in agreement with the one-dimensional studies of section 2, and can be demonstrated for a simple case using equations (4.35) and (4.36). In this case

$$\begin{aligned} \max[S_A(x,y)] &= s(y)t_2(-\infty) \\ &= s(y) \\ \min[S_A(x,y)] &= s(y)t_2(+\infty) \\ &= 0 \end{aligned} \tag{4.38}$$

Thus,

$$S_A(x_o,y) = 1/2\ s(y) \tag{4.39}$$

For $y \to -\infty$, the response at the edge is one-half; this agrees with the one-dimensional result.

To continue this discussion requires some knowledge of s(y); thus, using the previously stated conditions and considering the symmetry of the problem, the following form is suggested:

$$s(y) = \frac{1}{2} - \frac{1}{\pi}\tan^{-1}[by] \tag{4.40}$$

Note that this implies $s_o = 1/2$. When substituted into equation (4.35), one obtains

$$S^*(x,y) = \frac{1}{4} - \frac{1}{2\pi}\,[\tan^{-1}(bx) + \tan^{-1}(by)] + \frac{1}{\pi^2}\,\tan^{-1}(bx)\,\tan^{-1}(by) \qquad (4.41)$$

Again, the form of equation (4.30) has been reproduced; however, this differs from equation (4.31) in that separation of variables is present to some extent, and one does not have to contend with the term S_{oo}. In fact, equation (4.41) suggests that $S^*(0,0) = 0.25$, a value which is in reasonable agreement with the Monte Carlo results shown in figure 4-14.

Whether or not equation (4.41) will be of any use will again depend on experimental or other verification; however, it is thought that this form will be superior to that given by equation (4.31), since it appears to arise more "naturally" out of the physical situation, as represented by a one-dimensional model.

This concludes the study of Monte Carlo methods as applied to neutron radiography; to proceed any further will require a much more detailed analysis, if only to reduce statistical uncertainties. The results have generally indicated that a Lorentzian model will be useful in optical density analysis. Additionally, the Monte Carlo methods will provide an alternative procedure which will be doubly useful: the technique can be used to verify the results obtained by other methods, and it will stand by itself as an excellent means of calculation for these situations which cannot be easily handled by analytical means. Some suggestions for further investigation are presented in chapter 5.

5. SUMMARY AND CONCLUSIONS

In the earlier chapters of this work, a variety of methods for neutron radiographic image analysis have been presented and discussed. The purpose of this final chapter is to consider the various procedures in their entirety and thereby determine whether or not any further information may be obtained. In doing so, a summary of the major ideas will be provided; the numbers given refer to equations, unless otherwise indicated.

In section 2.1, the basic mathematics was developed in considerable generality. It was shown that with a few simple assumptions, the most general model could be reduced to a form well-suited to calculations (2.5). In addition, the various terms of the expression for the converter response were identified with particular physical effects, without having to specify a form for the line-spread function (2.5 ff). The advantage here of course is that should a suitable LSF be discovered, it presumably could be fitted into the analysis with little difficulty.

Next, a specific form was chosen for the LSF, namely the Lorentzian function characterized by the Lorentzian coefficient, C_L. It was suggested that the value of C_L might cause some problems, because of uncertainty as to whether or not C_L depends on sample properties. The resolution of this matter was left to later chapters. With this in mind, an expression for the general Lorentzian convertor response was derived (2.17), which in turn was further developed for the case of symmetric objects (2.23). As indicated in section 2.2, the Lorentzian form is easily calculated for any combination of material and geometry; a number of computer-generated examples were given.

In chapter 3, the concepts of resolution and total image unsharpness were examined by extending the basic theoretical ideas of chapter 2. In section 3.1, resolution was characterized by the resolution parameter R (3.2), and a method of calculating R for any material/geometry combination was presented. The method was illustrated using the "block" approximation, and a very simple equation for determining the resolution parameter was derived (3.10). The general case was then examined in a number of ways, and it was shown, or at least implied, that the resolution parameter may be material independent (3.12 ff). At this point it began to be apparent that the Lorentzian coefficient was, strictly speaking, independent of the sample being radiographed.

Another means of characterizing resolution is the response difference ΔS, defined by equation (3.15). In contrast to the resolution parameter R, ΔS could be related to the distance between particles, and not just the particle size. The block approximation was again used to derive an expression for a generalized response difference (3.20); additionally it was shown that this quantity could be calculated as a function of either materials or dimensions. This is in apparent conflict with the earlier result that resolution is material independent; however, one should note that G_0 and R are quite different means of characterizing resolution, and thus need not have the same features. Finally, the hazards of using the simple block approximation were discussed, along with some possible means of dealing with these problems.

In section 3.2, the ideas developed in the previous sections were expanded so as to be able to deal with the problems of "total" unsharpness, where factors other than those associated with the convertor screen come into play. It was shown that a generalized convertor response function could be derived (3.24, 3.25), but for the purposes of practicality, only screen and motion unsharpness were considered (3.26). For illustrative purposes, the block approximation was used again in an analysis which paralleled that of section 3.1. It was shown that in some cases the convertor response is independent of object motion; specifically, this is true when the exposure time is long or when the object motion is periodic (3.32 ff). The latter fact might be of use in a situation where exposure should be limited; an example is the use of x-rays on humans, where the dose must be minimized. Note that this indirectly suggests that ESF methods might be usefully applied to areas other than neutron radiography.

The next topics to be considered involved generalized forms of the resolution parameter R and the response difference ΔS (3.41 ff). It was shown that expressions for both quantities could be obtained, even though the nature of the calculations would probably be such that numerical methods would be necessary. The section was concluded by pointing out how caution must be applied in the use of ESF theory.

In chapter 4, two entirely different approaches to neutron radiographic image analysis were considered. Neither of these techniques involved the direct use of a specific model for the convertor response, and, up to a point, neither model required any complex mathematical formulation.

The first of these techniques involved a strictly numerical approach, whereby one analysed optical density curves solely on the basis of experimental data. No model for the imaging process was required, and presumably one could obtain any degree of accuracy in the results by improving the numerical techniques used. The analysis began with the simple matter of obtaining an LSF from an ESF by a simple finite-difference calculation (4.1); this would be of no great import in itself, were it not for the fact that this allows one to disregard the problem of explicitly specifying all of the factors affecting image formation. The examples given were anisotropism in the emission of secondary radiation and scattering of neutrons in the object being radiographed. Additionally, the numerical approach allows one to include departures from the ideal in one's experimental set-up; it was shown how C_E, an "experimental coefficient", could be calculated (4.3 ff), so that one would have a means of characterizing types of radiography other than neutron.

The next portion of the analysis involved setting up a calculation procedure whereby one could estimate such things as the geometry and composition of a sample. A matrix formulation ideally suited to computer use was derived (4.7 ff), and it was shown how an iterative approach might be required in order to determine the sample dimensions.

The particular advantage to the numerical approach is that no consideration of a characterizing parameter is necessary; while it may be instructive and useful to have such a parameter, the problem of evaluation makes it worthwhile to develop other techniques. As shown in earlier chapters, it was possible to view the Lorentzian coefficient as a function of sample and radiographic system properties; however, this conceivably would lead to a much more complicated model, which provided an even less certain feel for the physical aspects of the radiographic problem. However, as shown in section 4.2, it turns out that the Lorentzian coefficient (and presumably any similar characterizing parameter resulting from the use of a different LSF) does not depend on sample properties, but instead is strictly dependent on the radiographic imaging system. This was demonstrated using another "alternative approach", namely Monte Carlo analysis. In considering the Lorentzian coefficient and its associated difficulties, the problems analyzed will be summarized. First, using a very simple physical model, it was shown how the Lorentzian form compared very well with results obtained from a detailed calculation involving all the physical properties of a convertor foil (4.17 ff). This suggested that the Lorentzian form is an excellent model for calculation purposes, and also is quite adequate for representing the physical situation in the convertor. Next, it was demonstrated how the Lorentzian response function derived for a given geometry was a good representation of the physical results (4.19). In doing so, it was shown how the Lorentzian coefficient was independent of sample properties by relating it to the so-called attenuation product. Additionally, these results suggested that the use of the Lorentzian model in a situation where the assumptions of chapter 2 are strained would lead to results of a dubious nature.

The next problem considered sample scattering, a factor which the Lorentzian model neglects. It was shown how this led to results different from those predicted by the standard ESF technique, and again the implication was that the Lorentzian model should not be pushed beyond its assumptions. Indirectly, this once more precludes the artificial use of the Lorentzian coefficient to characterize sample properties.

Finally, a very basic two-dimensional analysis was undertaken. First, a general model was developed (4.20 ff), and it was shown how this became a rather complicated problem (in terms of calculation and application) even for simple cases. Some simple approximations based on a Lorentzian form were discussed and, it was shown how these approximations could be related to the physical aspects of the situation (4.31 ff). Next, a very simple Monte Carlo model was presented, and this clearly illustrated another limitation of the ESF approach: while it is quite possible to set up an ESF expression for any given situation, the calculational effort involved makes it more worthwhile to use another approach. This is not meant to denigrate the ESF approach; rather, it suggests that there is no need to do a large amount of work if simpler procedures exist.

Apart from the amount of work involved, use of the previously mentioned approximations indicated two things: first, that the Lorentzian form appears to hold up well in two dimensions, and second, that a one-dimensional model will work quite well for the two-dimensional case if it is applied far from the vicinity of such things as corners. This latter point is significant, in that it illustrates how the convertor screen isotropism is an extremely localized effect. Additionally (but less significantly), it suggests that a great deal of effort can be saved in some cases. The application of this idea was demonstrated by "building" a two-dimensional response function out of two one-dimensional functions (4.35 ff). It is of some interest to note that what was done here involved the separation of variables, an approach which has been used with considerable success elsewhere.

This concludes the analytical portion of this work. A number of techniques which may be of use in neutron radiographic image analysis have been developed, and the correlation between the ESF-based methods and the other more physically-oriented approaches suggest, indirectly, that the ESF methods are a good model for a physics analysis of neutron radiography. The usefulness of the techniques is further illustrated by good agreement with experimental data; this may be found in reference 11. On this basis then, it is suggested that further work, both analytical and experimental, be carried out with the aim of developing edge-spread function methodology to its fullest extent. In addition, the alternative approaches developed in chapter 4 should be examined more rigourously, both for their intrinsic virtues and as companion techniques for ESF methods. Taken as a whole, the various forms of analysis presented here will hopefully provide a comprehensive basis for understanding and evaluating neutron radiographic imaging processes.

APPENDIX

Monte Carlo Calculation Algorithms and Approximate Errors

LINE-SPREAD FUNCTION ANALYSIS

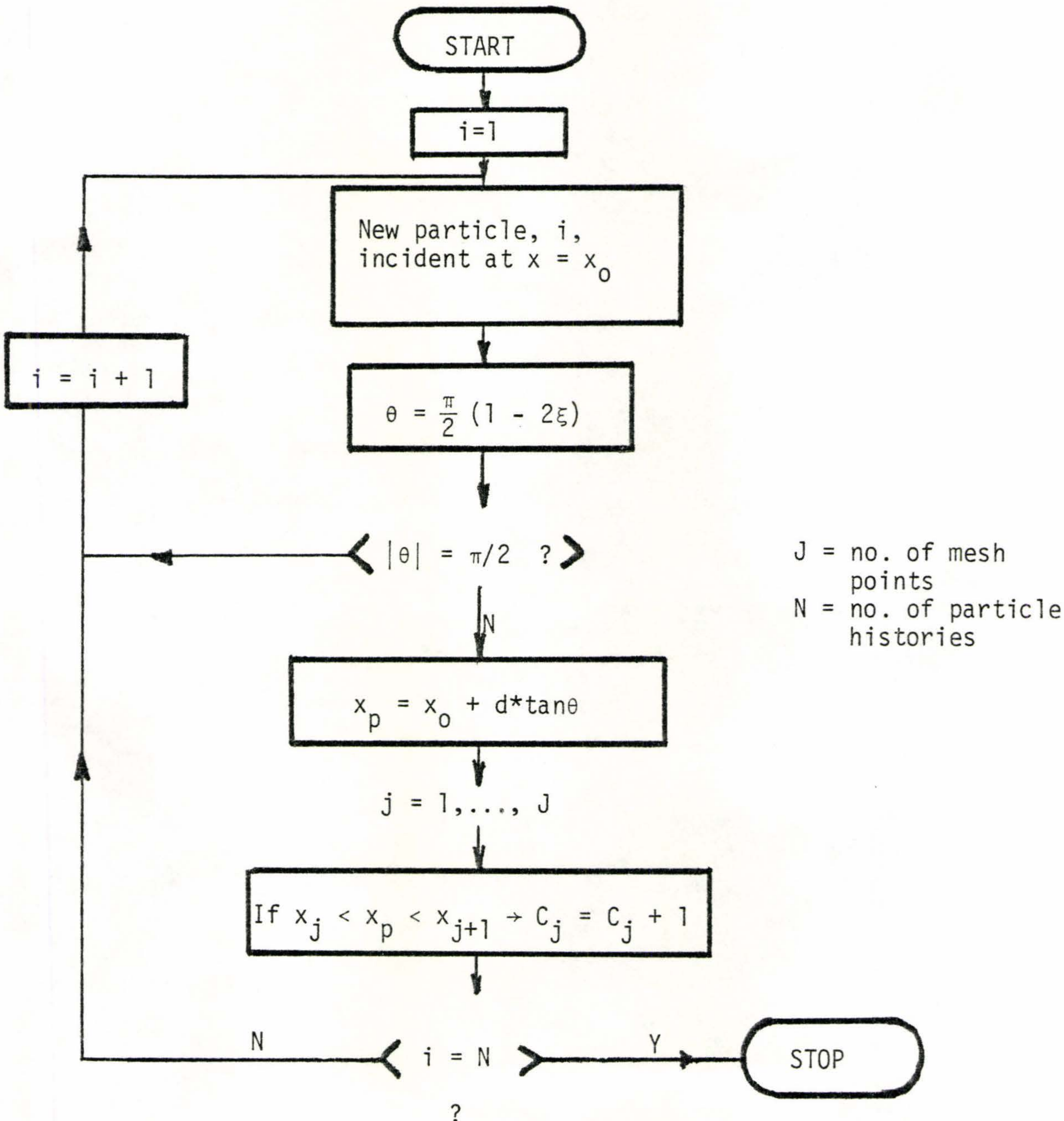

EDGE-SPREAD FUNCTION ANALYSIS

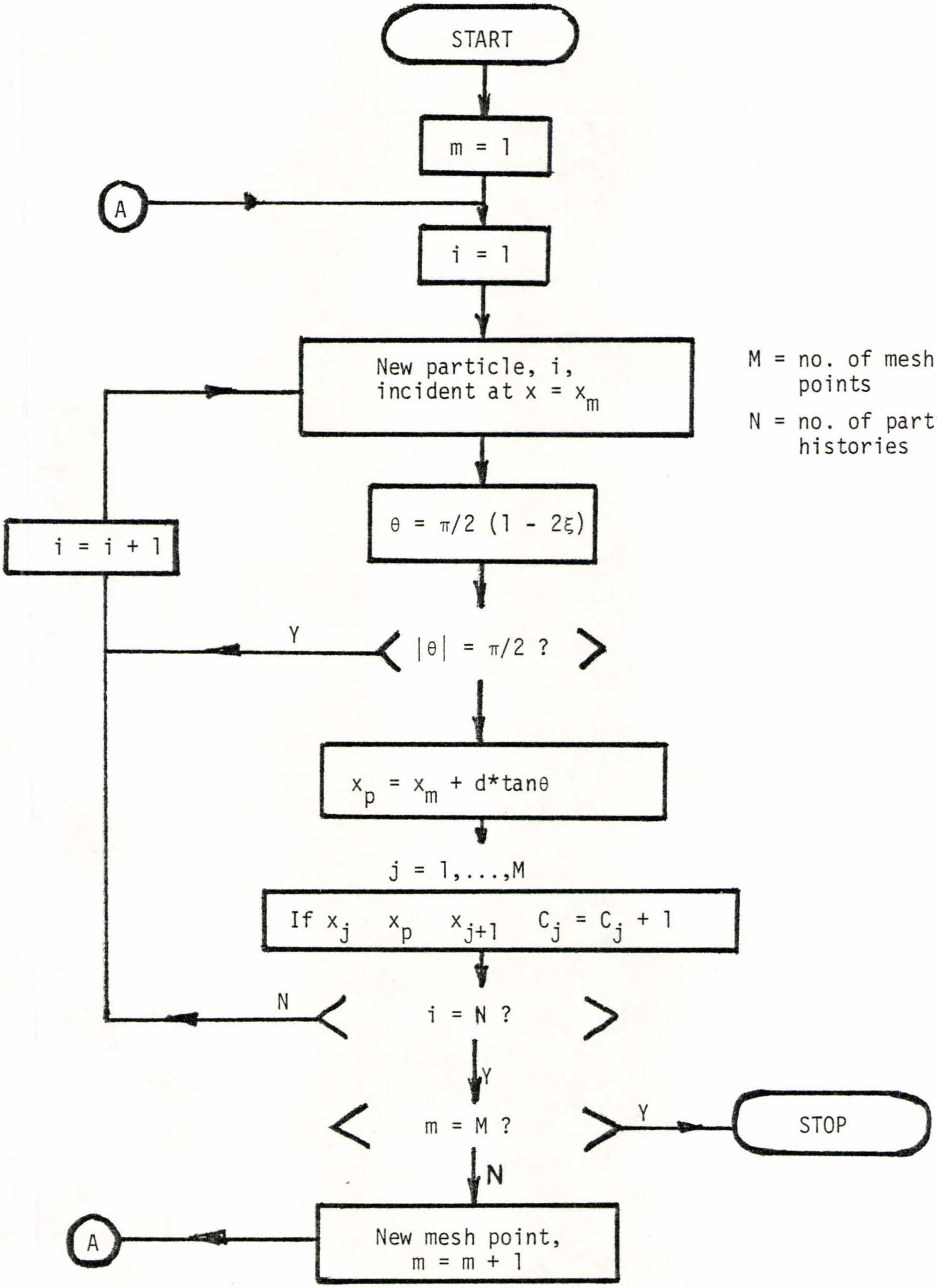

M = no. of mesh points

N = no. of particle histories

ESF ANALYSIS, INCLUDING SCATTER EFFECTS

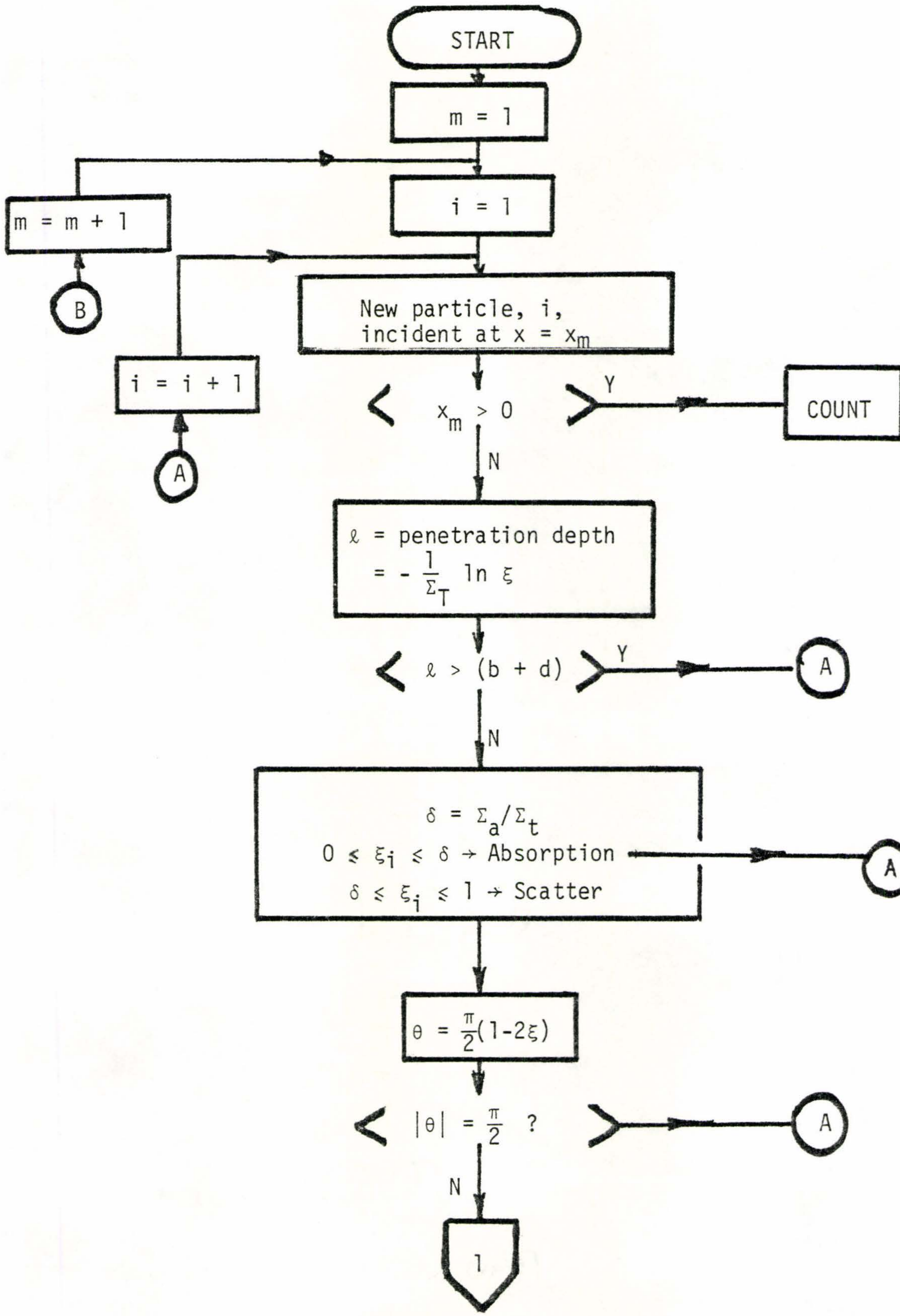

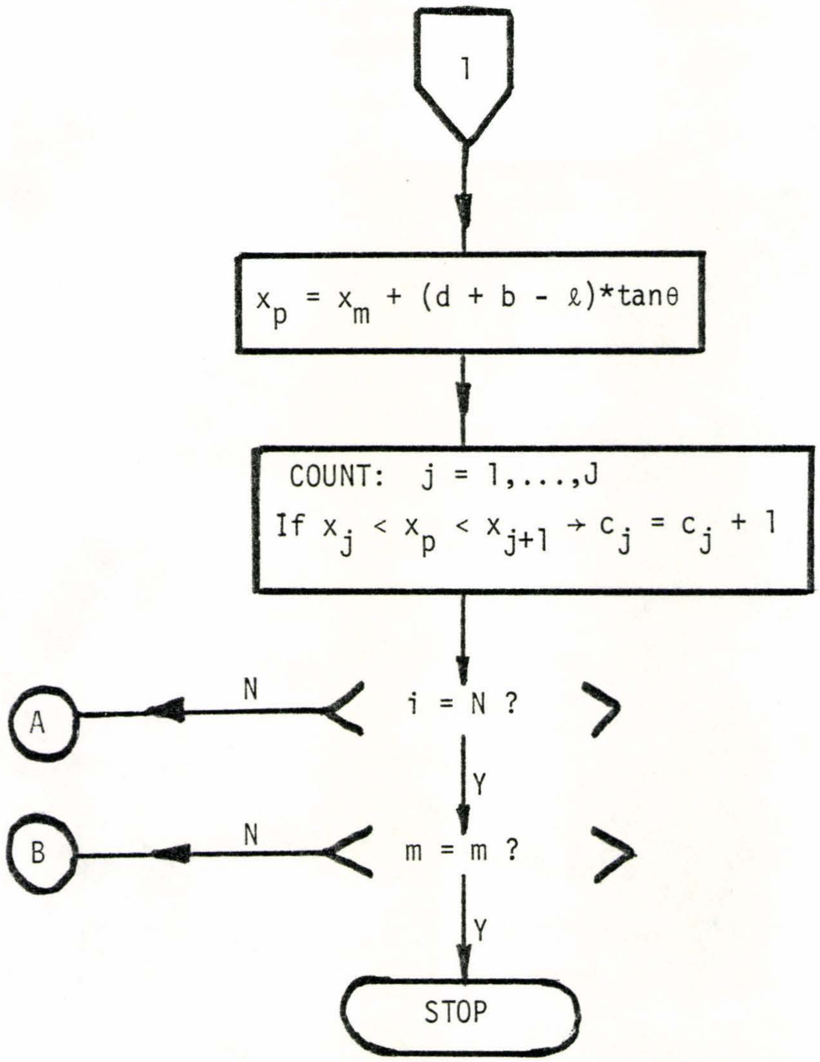
1
x_p = x_m + (d + b - ℓ)*tanθ
COUNT: j = 1,...,J
If x_j < x_p < x_j+1 → c_j = c_j + 1
i = N ?
N
A
Y
m = m ?
N
B
Y
STOP

CORNER-SPREAD FUNCTION ANALYSIS

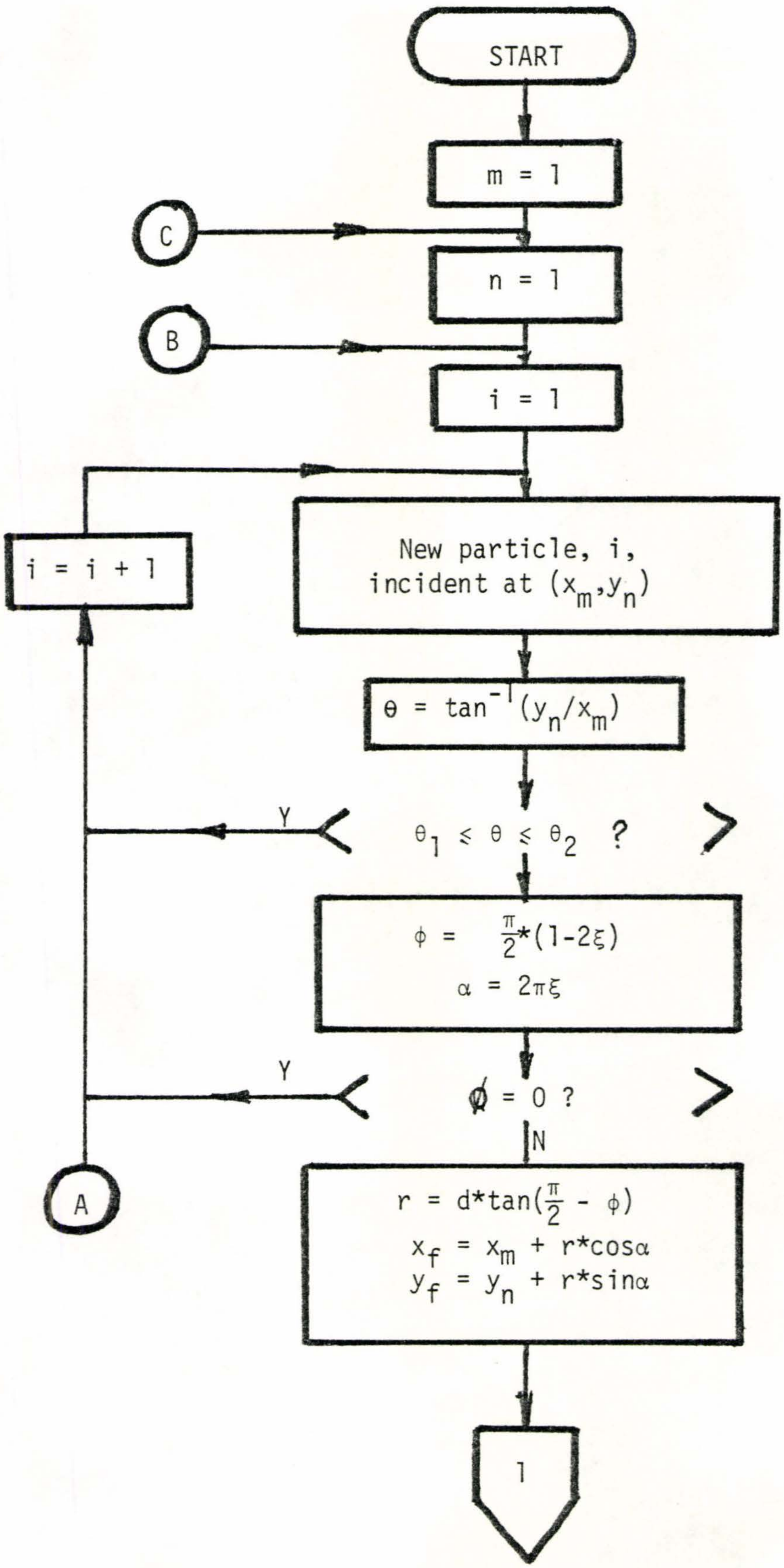

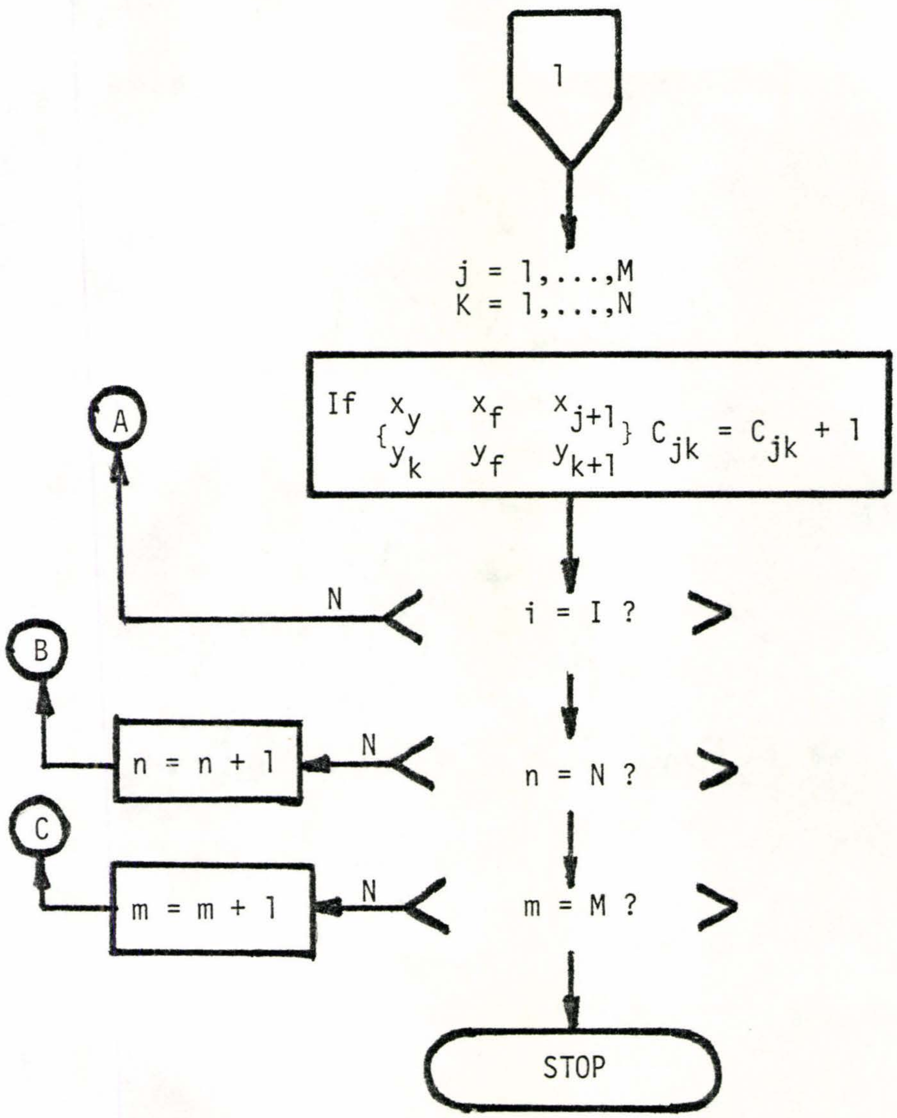
1
j = 1,...,M
K = 1,...,N
If {xy xf xj+1 / yk yf yk+1} Cjk = Cjk + 1
A
N
i = I ?
B
n = n + 1
N
n = N ?
C
m = m + 1
N
m = M ?
STOP

Approximate Errors

The errors listed below were estimated from

$$\rho \sim 100 \left(\frac{1}{\sqrt{N}}\right) \%$$

where N is the number of histories considered.

Case	N	ρ (%)
LSF	500,000	0.2
ESF	10,000 per value of x	1.0
ESF with scatter	10,000 per value of x	1.0
CSF	12,000 per co-ordinate pair (x,y)	0.9

REFERENCES AND BIBLIOGRAPHY

1. Harms, A.A., Garside, B.K., and Chan, P.S.W., "The Edge-Spread Function in Neutron Radiography"; J. Appl. Phys., 43, 3863 (1972).

2. Harms, A.A., Heindler, M., and Lowe, D.M., "The Physical Basis for Accurate Dimensional Measurements in Neutron Radiography"; Mat. Eval., 36, 5 (1978).

3. Harms, A.A., "Neutron Radiography of Corroded Metals"; contract report submitted to Dept. of Supply and Services, Government of Canada. DSS File #01SU CD3296049 (1978).

4. Garside, B.K., and Harms, A.A., "The Detection Process in Neutron Radiography"; J. Appl. Phys., 42 (1971).

5. Harms, A.A., and Zeilinger, A., "A New Formulation of Total Unsharpness in Radiography"; Phys. Med. Bio., 22 (1977).

6. Jensen, V.G. and Jeffries, G.V., "Mathematical Methods in Chemical Engineering"; Academic Press (1963).

7. Sobol, I.M., "The Monte Carlo Method"; University of Chicago Press, Chicago and London (1974).

8. Schaeffer, N.M. (ed.), "Reactor Shielding for Nuclear Engineers"; USAEC Office of Information Services (1973).

9. Nakamura, S., "Computational Methods in Engineering and Science"; John Wiley and Sons, Inc., New York (1977).

10. Osuwa, J.C., "Non-Symmetric Edge-Spread Functions"; Master's Project, Dept. of Engineering Physics, McMaster University, Hamilton, Canada (1979).

11. Butler, M.P., "Experimental Evaluations of ESF Methods for Neutron Radiographic Image Analysis", Master's Project, Dept of Engineering Physics, McMaster University, Hamilton, Canada (1980).